

Structural Evolution during Reversible Halogen Intercalation into WTe_2 : Commensurate–Incommensurate WTe_2I and Multistage WTe_2Br_x ($x = 0.5, 1.0$ and 1.25)

Patrick Schmidt,^a Carl P. Romao^b and Hans-Jürgen Meyer^{*a}

Halogen intercalation into the layered material tungsten ditelluride (WTe_2) provides a unique pathway to tune its structural and electronic properties. In this study, we detail the synthesis and characterization of the new bromine-intercalated phases WTe_2Br_x ($x = 0.5, 1.0$, and 1.25), and reinvestigate the iodine-intercalated analogue, WTe_2I . A defining feature of the bromine system is its rapid and re-versible "breathing" behavior at room temperature, allowing guest molecules to be absorbed or released from the van der Waals gaps under ambient conditions. Structural analysis shows that the bromine-poor phase $\text{WTe}_2\text{Br}_{0.5}$ crystallizes in the orthorhombic space group $Pmmn$, thereby maintaining a uniform stacking sequence. In contrast, the bromine-rich $\text{WTe}_2\text{Br}_{1.25}$ phase (space group $Imm2$) adopts an architecture where two distinct types of bromine layers alternate between the host layers. For the iodine system, the compound WTe_2I exhibits both incommensurate and commensurate (3+1)D modulated variants in the superspace group $P2_1/m(\alpha 0 \gamma)00$. In the commensurate polytype, the structural modulation locks into a rational vector, $\mathbf{q} = (1/2, 0, 1/6)$, which can be described also as a 3D supercell. Electronic structure calculations show $\text{WTe}_2\text{Br}_{0.5}$ and commensurately modulated WTe_2I to be metals with flat bands at the Fermi energy arising from the intercalation. These findings demonstrate the unusual stability and structural flexibility of anionic intercalation in a transition metal dichalcogenides.

Introduction

Layered transition metal dichalcogenides (TMDCs) have attracted intense interest for their unique electronic, magnetic, and topological properties.^{1–3} In these materials, strong in-plane covalent bonding and weak interlayer van der Waals forces give rise to a two-dimensional architecture that is highly responsive to external perturbations, such as intercalation or the application of pressure.^{2, 4} This open layered structure enables a rich intercalation chemistry in which various guest species can be incorporated. Typically, cations, neutral molecules or organic molecules can be inserted between the layers, thereby modifying the host's structure and properties.^{5–16}

WTe_2 is a particularly intriguing member of the TMDC family and crystallizes in an orthorhombic T_d phase, where it exhibits semimetallic behavior,^{17–19} exceptionally large, non-saturating magnetoresistance,^{20, 21} and complex topological properties—ranging from a 2D topological insulator in its monolayer form to a type-II Weyl semimetal in the bulk.^{22, 23} It also displays superconductivity at low temperatures²⁴ and shows a charge density wave (CDW) state^{25–32}, underscoring its rich and exotic physical

properties. The crystal structure (space group $Pmn2_1$) features distorted octahedral coordination of tungsten atoms by tellurium atoms, with zigzag W–W chains running within the ab -plane along the a -axis and van der Waals gaps separating the WTe_2 layers.³³ These structural features render WTe_2 highly receptive to intercalation, offering an opportunity to tune its electronic ground state through the controlled insertion of guest species.

Cationic intercalation into the structure of WTe_2 has been reported for $A_{0.5}\text{WTe}_2$ compounds ($A = \text{K}, \text{Rb}, \text{Cs}$), which we have previously characterized structurally and electronically, showing that alkali ions act as electron donors.³⁴ While cationic intercalation into TMDCs is well established, involving alkali metals,^{5, 8–11, 13, 35, 36} organometallic species, or molecular donors,^{12, 14–16} anionic intercalation remains extremely rare. Halogen molecules ($\text{I}_2, \text{Br}_2, \text{Cl}_2$), despite their strong oxidizing nature, have largely resisted clean insertion into TMDCs in a structurally defined and stoichiometric manner. Instead, halogens have often been introduced during crystal growth as transport agents and later found in low concentrations or as surface dopants. For example, Cl_2 and I_2 have been shown to form bound excitonic centers in $\text{MoS}_2, \text{WS}_2$, and MoSe_2 , being responsible for characteristic luminescence features at low temperatures.^{37–48} However, these guest species reside in dilute, disordered environments, without forming ordered intercalation phases or significantly expanding the host lattice. As such, these systems are better classified as halogen-doped or halogen-decorated TMDCs—rather than true intercalation compounds.

^a Section of Solid State and Theoretical Inorganic Chemistry, Institute of Inorganic Chemistry, Eberhard Karls University Tübingen, Auf der Morgenstelle 18, 72076 Tübingen, Germany.

^b Department of Materials, Faculty of Nuclear Sciences and Physical Engineering, Czech Technical University in Prague, Trojanova 13, Prague 120 00, Czech Republic.

Recently, we have demonstrated that WTe_2I is the first and so far only example of a structurally confirmed anionic halogen-intercalated TMDC.^{49, 50} In this compound, planar monolayers of iodine are inserted between the WTe_2 layers of the orthorhombic host, expanding the c -axis by $\sim 56\%$ and forming a fully stoichiometric intercalate. Importantly, the intercalation process was shown to be topotactically reversible: heating WTe_2I above 100°C under inert conditions fully deintercalated iodine and re-generated pristine WTe_2 . These results established WTe_2I as a prototypical system for reversible anionic intercalation in layered semimetals. The crystal structure of WTe_2I was refined an averaged three-dimensional structure from powder X-ray diffraction (PXRD) data, which revealed notably large anisotropic displacement parameters (ADPs) for iodine, already suggesting a positional modulation.

Subsequent single-crystal X-ray diffraction studies indicated the presence of an incommensurately modulated structure. Density functional theory (DFT) calculations supported these findings, indicating significant charge transfer from WTe_2 to iodine, a shift of the Fermi level, and soft phonon modes characteristic of structural instability. In this work we present an incommensurate and a commensurate structure, appearing simultaneously for WTe_2I , and for better realization we report a supercell of the structure.

Despite many reports of halogen-related doping no other halogen-intercalated TMDC compound has been structurally verified to date. The present work expands this chemistry by demonstrating that bromine, though more volatile and reactive than iodine, can also be intercalated into WTe_2 in well-defined stages. We describe the synthesis and reversible intercalation of bromine into WTe_2 , leading to the formation of stable WTe_2Br_x compounds with distinct structural and electronic signatures, representing only the second known example of an anionic halogen intercalation phase in the TMDC family. Time-resolved powder X-ray diffraction (PXRD) reveals that bromine can be reversibly inserted and removed from the van der Waals gaps, with distinct diffraction patterns for each stoichiometry ($x = 0.5, 1.0, \text{ and } 1.25$), highlighting a remarkable “breathing” behavior that enables dynamic control of composition and structure under mild conditions.

Results and discussion

Incommensurate and commensurate modulations of WTe_2I

As reported previously,⁴⁹ WTe_2I forms when WTe_2 is reacted with iodine at $40\text{--}200^\circ\text{C}$. Elemental analyses confirm a stoichiometry corresponding to one iodine per WTe_2 (WTe_2I) within experimental uncertainty (see Experimental Section). No phase transition of WTe_2I single crystals was detected between 100 K and 270 K .

Single-crystal X-ray diffraction studies, performed on several crystal specimens at 150 K , revealed two closely related (3+1)D modulated structure variants in the superspace group $P2_1/m(\alpha 0 \gamma)00$ with almost identical basic lattice parameters (Table 1), in good agreement with the previously reported unit

cell.⁴⁹ The incommensurate variant is described by the modulation vector $\mathbf{q} = (0.4487, 0, 0.1617)$, whereas the commensurate polytype has $\mathbf{q} = (1/2, 0, 1/6)$ and can equivalently be described as a 3D supercell. Using the transformation matrix $(1\ 0\ -3, 1\ 0\ 3)$, a primitive $P2_1/m$ supercell with $a = 12.1694(1)\text{ \AA}$, $b = 21.8799(2)\text{ \AA}$, $c = 12.1726(1)\text{ \AA}$ and $\beta = 117.635(1)^\circ$ is obtained. For ease of comparison and broader reusability, the commensurate structure was also refined as an explicit 3D superstructure in SHELXL; the resulting model is crystallographically equivalent and is provided as a reference in the deposited data (Table 1). All modulated crystals show pronounced pseudo-merohedral twinning, where the main reflections overlap, while the satellites are well separated in the incommensurate case and partially overlap for the commensurate polytype. The twin law corresponds either to a twofold rotation about c -axis or an equivalent mirror perpendicular to it; owing to the metric pseudosymmetry ($\beta \approx 90^\circ$), both descriptions are indistinguishable, and a conventional twofold twin matrix was applied, with the twin fraction of the second domain refined to $0.432(2)$. Depending on the batch, crystals were found to be fully commensurate or incommensurate (with slightly different incommensurate \mathbf{q} -vectors), and some specimens contained mixed domains, combining commensurate and incommensurate regions, or even multiple distinct incommensurate modulations alongside the commensurate phase (Figure S1). Although satellites are visible up to $m = \pm 4$, refinements were restricted to $m = \pm 2$ and carried out with the minimal, physically meaningful set of modulation waves needed to reproduce the observed atomic displacements, thereby avoiding over-parameterization. Refinement statistics are summarized in Table 1.

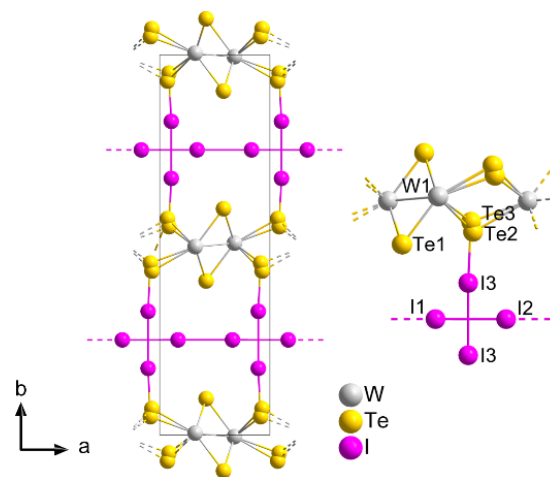


Figure 1. Section of the average incommensurate WTe_2I structure (left) and a smaller section with atom labels (right). Note, the zig-zag chains of tungsten atoms running parallel to the c -axis.

The average 3D structure is essentially identical to the previously reported model of WTe_2I (see Figure 1), but requires two additional split sites, Te3 and I3. These minor positions are $\sim 15.5\%$ occupied, while the corresponding main sites (Te2, I1, and I2) are under-occupied accordingly, consistent with a local defect motif rather than a distinct bulk phase. Structurally, the splitting is initiated by a local $\sim 90^\circ$ rotation of a I_2 unit (denoted

as I3) out of the iodine-net plane. This reorientation necessitates a concomitant shift of the adjacent tellurium atom. This reorientation is accommodated by a concomitant shift of the adjacent tellurium atom (Te2→Te3); without this shift, the resulting Te2-I3 contact would be unrealistically small and physically prohibitive. By adopting the Te3 position, the system instead establishes a Te3-I3 distance of ~ 2.77 Å. This value is characteristic of a covalent bond (sum of covalent radii ~ 2.71 Å), suggesting that the local defect motif is stabilized by a degree of covalent bonding between the host layer and the guest. This localized covalent interaction likely acts as an 'anchor' that pins the iodine guest to the WTe_2 framework, thereby stabilizing the defect motif and dictating the specific periodicity of the long-range structural modulation.

Table 1: Crystallographic data and details of the crystal structure refinement of the different WTe_2 modifications. Refinements were performed for (in)commensurately modulated crystal structures and the corresponding supercell. Detailed information on the modulation functions is given in the crystal information file. All crystals were measured with Mo-K α radiation at 150 K.

Modification	WTe_2		
	incom-	commensurate	supercell
CCDC	2520418	2519690	2519736
Formula		WTe_2I	$W_6Te_{12}I_6$
$M / g \cdot mol^{-1}$		565.95	3395.7
Crystal system		monoclinic	
(Super)space group	$P2_1/m(\alpha 0\gamma)00$	$P2_1/m$	
Modulation wave vector \mathbf{q}	(0.4487 0 0.1617)	(1/2 0 1/6)	—
m max.	≤ 2	≤ 2	—
t_0	0	0	—
$a / \text{Å}$	6.3200(2)	6.30257(5)	12.1694(1)
$b / \text{Å}$	21.8060(6)	21.8792(3)	21.87990(2)
$c / \text{Å}$	3.4713(2)	3.47075(3)	12.1726(1)
$\beta / ^\circ$	90.057(3)	90.0268(7)	117.635(1)
V	478.40(3)	478.600(9)	2871.38(6)
Z	4	4	4
θ -range / $^\circ$	1.97-38.01	1.89- 45.01	1.888-30.508
unique reflections/ parameters	7009 / 193	7023 / 152	8947 / 294
twvol2 or BASF	0.432(2)	0.394(4)	0.378(2)
$R_1/wR_2/\text{GooF}$ (all data)	4.86 / 7.47 / 1.10	6.99 / 14.37 / 1.08	0.0433 / 0.0999 / 1.022
R_1/wR_2 : (all main)	1.65 / 3.80	5.18 / 13.33	—
(all 1st order)	6.92 /	8.54 / 17.19	—
(all 2nd order)	12.09 /	9.13 / 19.37	—
max./min.	-1.02 /	-1.96 / 1.75	-4.081 / 4.297
$\Delta\rho/e^- \cdot 10^{-6} \text{ pm}^3$	1.25		

Since the commensurate and incommensurate refinements are nearly identical apart from the modulation vector, we focus here on the incommensurate model. The modulation is dominated by the iodine sublattice, where iodine atoms show a pronounced displacive modulation within the planar net (see Figure 2, Figure 4 and Figure 3 right), whereas the WTe_2 layers exhibit only small, coupled distortions. Within the iodine layer, the displacive modulation translates into a pronounced spread of I-I distances. Over one modulation period, the shortest and longest distances within the I1/I2 planar net span 2.688(8)–

4.018(8) Å (see Figure S2) and the I3-I3 distance remains comparatively long at 3.272(2) Å, highlighting the strongly distorted and non-uniform iodine net. A representative section of the modulated structure at $t = 0$ is shown in Figure 2.

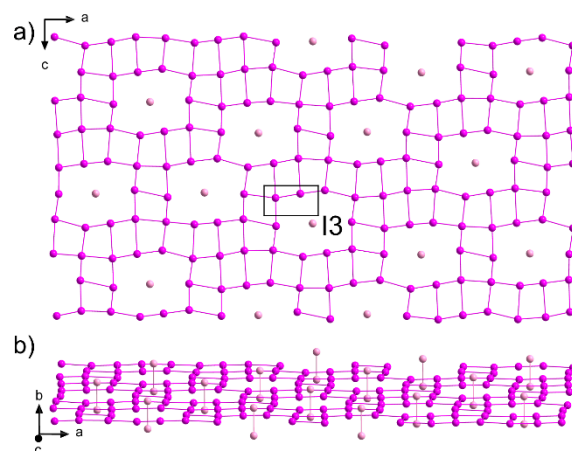


Figure 2. Section of the incommensurate WTe_2I structure a) only showing one iodine layer with I_2 dumbbells of I_3 being aligned along the b -axis, including the projected unit cell; and b) a corresponding view along the c -axis, emphasizing the I_2 dumbbells of I_3 . I_1 and I_2 are displayed purple, and I_3 in lighter purple.

The structure solution and refinement indicate that the displacement modulation of the iodine net is most pronounced in the ac -plane. Superimposed on this, an occupational modulation is required and was modeled using crenel functions (harmonics, orthogonalized to crenel interval) for the Te2/I2 and Te3/I3 split positions. The crenel intervals are $\Delta(\text{Te2/I2}) = 0.831824$ and $\Delta(\text{Te3/I3}) = 0.168176$, consistent with the intermittent appearance of the I_3 site, which corresponds to a local $\sim 90^\circ$ out-of-plane reorientation of an I_2 unit out of the ac -plane that disrupts the wave-like iodine layer. The crenel functions were refined using constraints linking their origins and Δ intervals ($\Delta(\text{Te2/I1/I2}) + \Delta(\text{Te3/I3}) = 1$), ensuring a consistent occupational modulation between the split-site pairs.

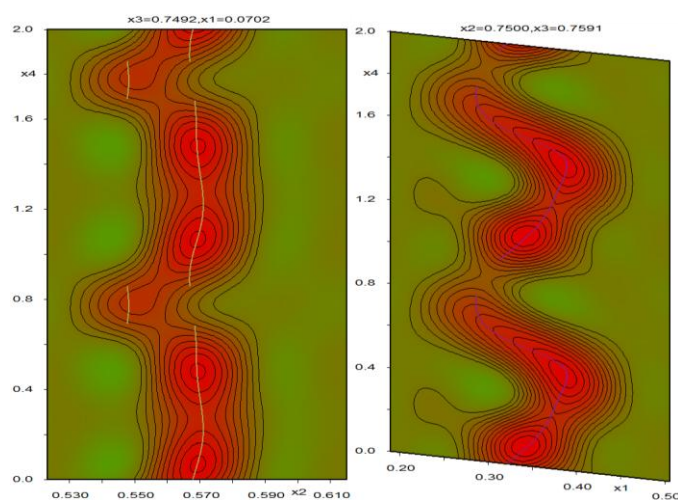


Figure 3. de Wolff sections (Fobs) of x_2 - x_4 plane for Te2 and Te3 (left) and in the x_1 - x_4 plane for I1 (right). Refined atomic positions are indicated by lines (Te: yellow; I: purple); the Te2 and Te3 sections are highlighted at $x_2 = 0.57$ and $x_2 = 0.55$, respectively. The electron density is visualized as a heat map (red = high, green = low).

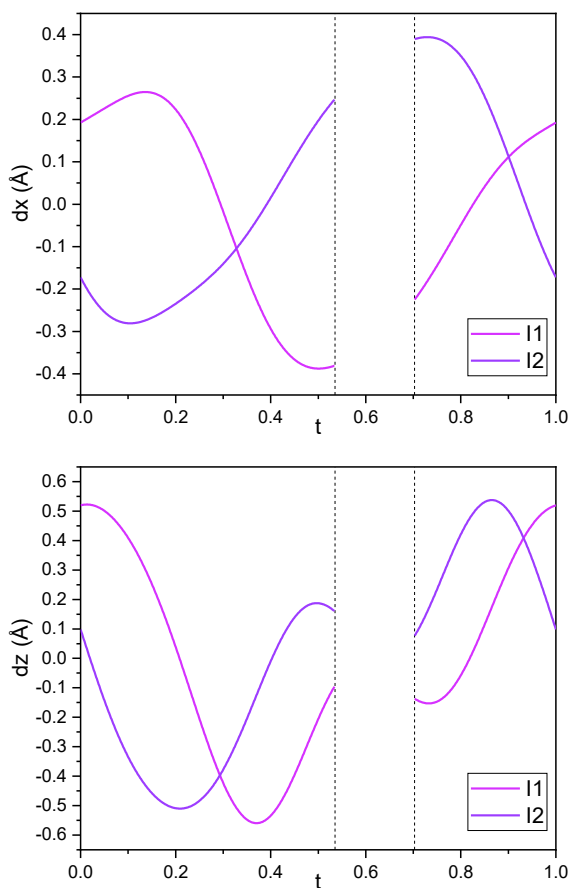


Figure 4. The modulation functions of the deviations from the average positions for I2 and I3 along x and z directions as a function of internal phase coordinate t with crenel limits marked as dashed vertical line.

To accommodate this local motif, Te2 splits into Te2/Te3 and induces subtle but observable distortions in the WTe₂ layer. The corresponding de Wolff sections (Fobs) through the (3+1)D Fourier map for Te2/Te3 and I2 is shown in Figure 3.

Although the host-layer modulations are comparatively small, they are clearly resolved. In particular, the position modulation of tungsten atom shows a characteristic saw-tooth modulation in the x_3 - x_4 section (see Figure 6, Figure 7), resulting in an average W–W distance of 2.86(1) Å. The shortest W–W contact with 2.78(1) Å remains closer to the average, whereas the longest distance with 3.10(2) Å periodically disrupts the chain after segments of roughly ~ 12 tungsten atoms. This disruption is induced by the I3 atom, which corresponds to the out of plane I₂ dumbbell of the iodine layer above and below the projected ac -plane of W chains, shown in Figure 5 and Figure S3.

Apart from these interruptions, the W–W distances vary only modestly with ~ 0.08 Å (see Figure 7, grey lines). The remaining tellurium sites exhibit similarly small displacements, with amplitudes of approximately $d_{xyz}(\text{Te1}) = \pm 0.1$ Å and $d_{xyz}(\text{Te2}) = \pm 0.06$ Å. Further refinement details, including constraints, parameter correlations, and the complete list of refined variables, are provided in the deposited CIF and in the Supporting Information.

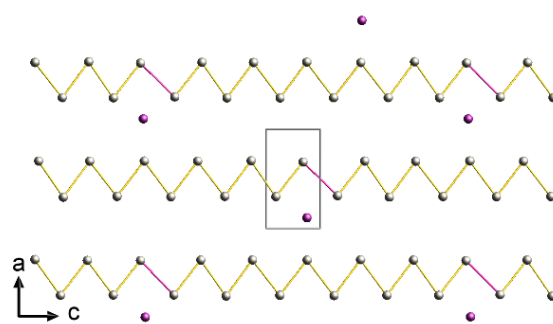


Figure 5. Section of the incommensurate WTe₂I structure viewed along the b direction with highlighted unit cell. For clarity, tellurium atoms are omitted and only one interlayer section in the ac -plane of the tungsten zigzag chains is shown, together with the I₂ dumbbells (I3 sites) aligned along b which are directly above and beyond of the ac -plane section. Elongated W–W contacts, indicating disruption of the tungsten chain are highlighted by violet bonds (W: grey; I: violet; $t = 0.62$).

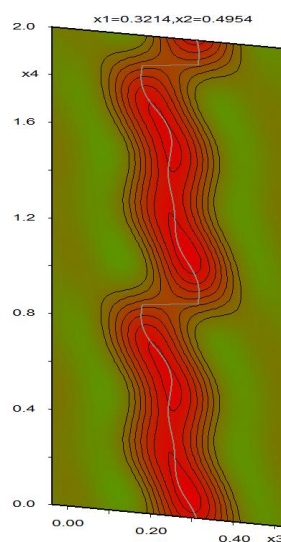


Figure 6. de Wolff sections (Fobs) of x_3 - x_4 plane for W1 in WTe₂I. Refined atomic positions are indicated by a grey line. The electron density is visualized as a heat map (red = high, green = low).

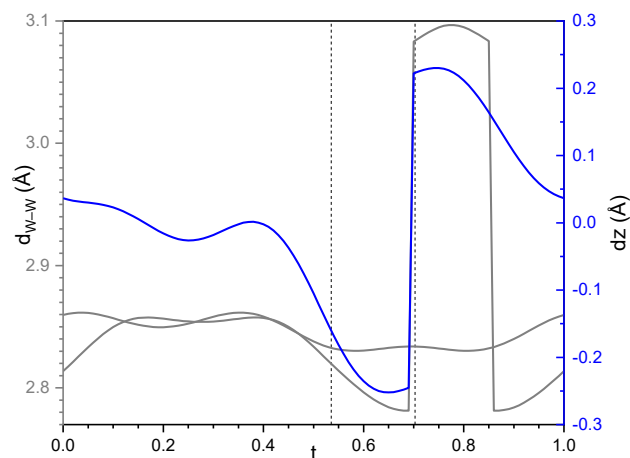


Figure 7. t plots of the W–W distances (grey) and positional deviation (blue) of tungsten along x_3 direction in WTe₂I with crenel limits marked as dashed vertical line.

Commensurate structure and superstructure model of WTe_2I

In addition to the incommensurate variant, a commensurate polytype is occasionally obtained in which the modulation “locks in” to the rational vector $\mathbf{q} = (1/2, 0, 1/6)$ and can therefore be described as a conventional three-dimensional $P2_1/m$ superstructure. Using the transformation matrix $\begin{pmatrix} 1 & 0 & -3 \\ 0 & 1 & 0 \\ 1 & 0 & 3 \end{pmatrix}$ yields a primitive supercell ($a \approx 12.17 \text{ \AA}$, $b \approx 21.88 \text{ \AA}$, $c \approx 12.17 \text{ \AA}$, $\beta \approx 117.64^\circ$; $W_6Te_{12}I_6$), which makes the modulation periodicity explicit in real space. In this commensurate description, the iodine net adopts a regular repeating motif that mirrors the rational components of \mathbf{q} , where along a direction, the rotated defect motif alternates such that every second I_2 unit is rotated by $\sim 90^\circ$ out of the iodine-net plane and appears as the I_3 site, while along the c direction the same motif repeats with a six-unit periodicity (Figure 8). The commensurate structure reproduces essentially the same I–I distance distribution, but arranges the shorter and longer contacts into an exactly repeating pattern.

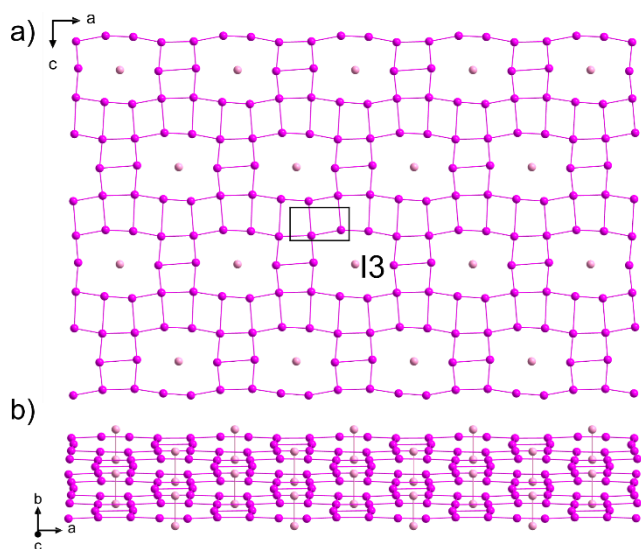


Figure 8. Section of the commensurate WTe_2I structure only showing a) one iodine layer with highlighted I_3 units aligned along the b -axis with unit cell shown, and b) a corresponding view along the c -axis, emphasizing the I_2 dumbbells (I_1/I_2 : purple; I_3 : lighter purple).

Refinement in the commensurate setting is advantageous over a purely 3D average-cell description because the modulation is represented explicitly rather than being “smeared out”, typically improving agreement factors and yielding cleaner residual density. Overall, the commensurate model can be viewed as a periodic approximant of the incommensurate structure that facilitates direct real-space visualization of both the iodine-net displacement wave and the ordered occurrence of the I_3 defect motif. For ease of comparison and broader reusability, the commensurate structure was also refined as an explicit 3D superstructure in SHELXL; the resulting model is crystallographically equivalent and is provided as a reference in the deposited data (Table 1). Because the diffraction data are affected by twinning and residual modulation, the supercell refinement was improved by modeling the interlayer iodine net as a two-compo-

nent disordered layer (atom sites Ixa/Ixb ; $x = 2-11$), with coupled occupancies constrained to unity and the b component accounting for $\sim 20\%$ occupancy. The minor b component represents a slightly b -rotated relative alignment of the iodine layer, whereas the out-of-plane iodine positions remain unaffected (see Figure S4).

Synthesis and “breathing” behavior of WTe_2Br_x

WTe_2Br_x powder phases were prepared by Schlenk techniques by exposing orthorhombic WTe_2 to an excess of bromine liquid between 0 and 30°C . Single crystals were intercalated by bromine vapor at room temperature for 4 days or with liquid bromine at 6°C for 2 days. Although crystallinity is generally compromised by the multiple phase transitions during bromine uptake and release, the vapor intercalation route consistently afforded crystals of higher quality than direct contact with liquid bromine. Thermal stability is a critical constraint in this system. While intercalation proceeds smoothly even near room temperature, heating WTe_2 with excess bromine in a closed vessel to 60°C leads to decomposition of the host structure and formation of binary halides, for example $TeBr_4$ and WBr_6 .

A striking feature of this system is a fast and reversible “breathing” behavior, present at room temperature, which involves an uptake and release of guest bromine. The bromine content can be increased up to the maximum stage with $x = 1.25$ by supplying liquid bromine, and bromine can conversely be removed from the van der Waals gaps (at room temperature) under constant argon flow. The actual bromine content in the structure of WTe_2Br_x is highly temperature sensitive during this de-intercalation step. Evaporation of excess bromine under a constant flow of argon yields $WTe_2Br_{1.25}$ when the temperature is maintained between 0 and 5°C , whereas the comparatively stable $WTe_2Br_{0.5}$ phase can be obtained at around 25°C . Starting from $WTe_2Br_{0.5}$, re-intercalation to the bromine-rich stage is particularly rapid and proceeds within minutes.

Elemental analysis by argentometric titration of $WTe_2Br_{0.5}$, and deintercalation of Br_2 saturated WTe_2Br_x confirms the variable bromine content and supports three distinct composition regimes in WTe_2Br_x at $x = 0.5, 1.0,$ and 1.25 .

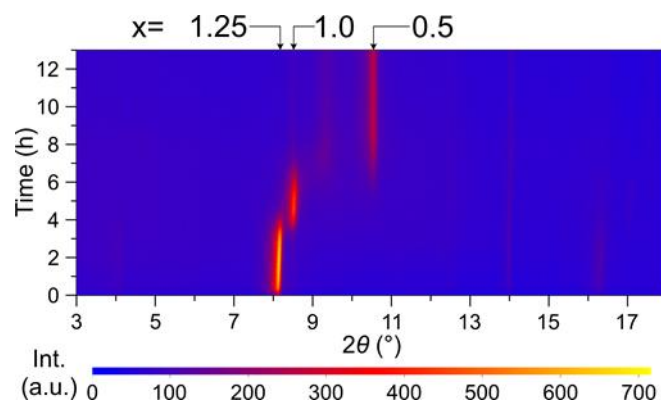


Figure 9. Time resolved PXRD analysis of WTe_2Br_x showing structural evolution during bromine deintercalation with discrete phases from $x = 1.25$ to 1.0 and 0.5 (for full 2θ range see Figure S5).

The dynamics of bromine exchange are directly captured by *in situ* PXRD studies. Starting from $WTe_2Br_{0.5}$, the bromine uptake

is extremely rapid and occurs within minutes. The accompanying change in bromine content is directly reflected in the basal reflections that tracks the interlayer spacing. For the monoclinic phases, the corresponding layer-stacking reflection, indexed here as (020), shifts continuously toward lower 2θ angles as the van der Waals gap expands to accommodate bromine. Upon deintercalation, time-resolved PXRD in Figure 9 reveals the reverse evolution through discrete stages, and the basal reflection shifts back toward higher 2θ as bromine is released from the lattice ($2\theta = 8.21^\circ$, 8.52° and 10.56°).

This inherent reversibility also explains why $\text{WTe}_2\text{Br}_{1.0}$ is difficult to isolate and handle. Unless samples are stored under strictly controlled conditions, bromine readily diffuses in or out, and bromine contents of the sample near $x = 1.0$ often relax toward $x = 0.5$ or $x = 1.25$. As a result, mixtures are frequently obtained in which $\text{WTe}_2\text{Br}_{1.0}$ coexists with $\text{WTe}_2\text{Br}_{0.5}$ or $\text{WTe}_2\text{Br}_{1.25}$. The $\text{WTe}_2\text{Br}_{1.0}$ phase also typically shows reduced crystallinity compared with the more stable end members, which we attribute to ongoing bromine exchange between the two stages.

Thermogravimetric analysis (TGA) of products obtained from the reaction of WTe_2 with excess bromine provides additional support for these composition regimes. During controlled deintercalation, distinct changes in the mass-loss rate mark transitions between the bromine-rich and bromine-poor stages. The TGA traces in Figure 10 show an initial rapid loss of excess bromine, followed by regimes of slower mass loss and a final, near-horizontal segment with only a subtle residual mass-loss rate. At 25°C , the first clear change in slope corresponds to a bromine content consistent with $\text{WTe}_2\text{Br}_{1.25}$, whereas at 50°C the first change in slope is shifted to the intermediate composition $\text{WTe}_2\text{Br}_{1.0}$. In both cases, the ensuing near-horizontal segment is consistent with the comparatively stable $\text{WTe}_2\text{Br}_{0.5}$ phase, which still shows a very slow residual bromine loss that becomes more pronounced at higher temperature. Accordingly, samples were stored cooled ($\leq 0^\circ\text{C}$) or kept under a sufficient bromine counter pressure at room temperature to suppress bromine evaporation. Even though phase-pure $\text{WTe}_2\text{Br}_{1.0}$ could not be isolated and structurally characterized, the established structure of $\text{WTe}_2\text{Br}_{1.25}$ shares key motifs with WTe_2I , which suggests that the intermediate $\text{WTe}_2\text{Br}_{1.0}$ phase may follow a closely related structural principle and has a similar structure. Owing to the highly corrosive nature of bromine, specialized reaction and measurement setups were employed, as described in the Experimental Section and the Supporting Information.

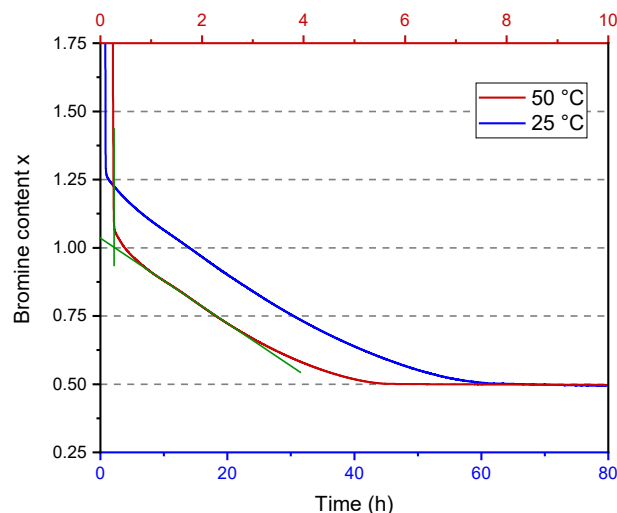


Figure 10. TGA showing the bromine loss of bromine saturated WTe_2Br_x samples, showing steps at $x = 1.25$, 1.0 , and 0.5 at constant temperature of 25°C (blue) and 50°C (red), under constant argon flow of $320\text{ ml}\cdot\text{min}^{-1}$ (an onset fit for the 50°C measurement is shown in green).

Crystal structure of $\text{WTe}_2\text{Br}_{0.5}$

The bromine-intercalated phase $\text{WTe}_2\text{Br}_{0.5}$, representing the lowest bromine content in the WTe_2Br_x series, crystallizes in the orthorhombic space group $Pm\bar{m}n$ with refined lattice parameters $a = 16.7450(4)\text{ \AA}$, $b = 3.67734(3)\text{ \AA}$, and $c = 6.29678(8)\text{ \AA}$. As shown by the Rietveld plot in Figure 11, the powder diffraction pattern is well described by the refinement ($R_{\text{Bragg}} = 2.028\%$, $R_p = 5.438\%$, $R_{\text{wp}} = 7.104$, $\chi^2 = 1.268$, Number of reflections/parameter 392/27), confirming a well-defined crystalline phase.

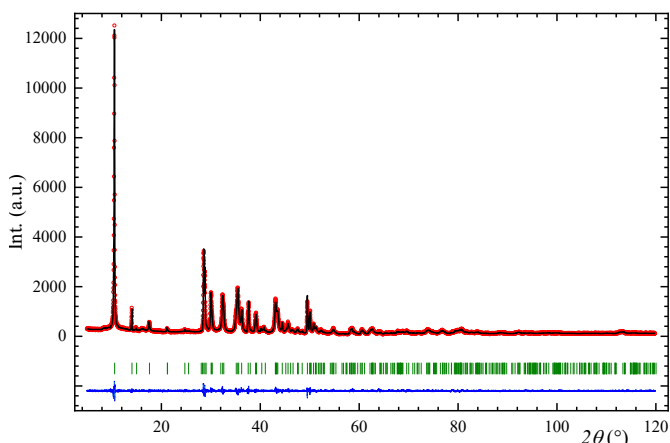


Figure 11. Rietveld PXRD structure refinement of $\text{WTe}_2\text{Br}_{0.5}$ with the space group $Pm\bar{m}n$ at 298 K with the experimental (red) and calculated (black) intensities. Bragg positions (green) and the difference curve (blue) are also shown.

In the chosen setting, the a -axis corresponds to the stacking direction. The WTe_2 layers adopt a stacking arrangement in which the tungsten zig-zag chains of neighboring layers are brought into eclipsed alignment along the a -direction, generating an enlarged interlayer void to accommodate bromine guest atoms.

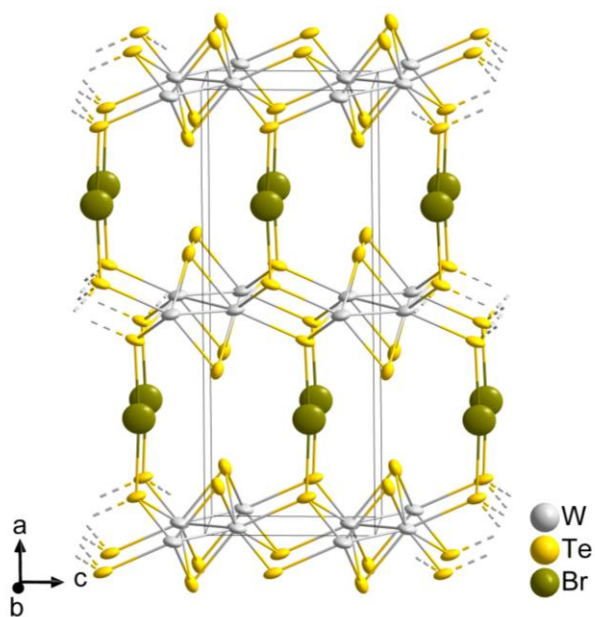


Figure 12. Section of the $\text{WTe}_2\text{Br}_{0.5}$ crystal structure highlighting the position of bromine atoms within the van der Waals gap, with their alignment toward Te1, thereby connecting adjacent WTe_2 layers. Atomic displacement parameters are shown as anisotropic displacement ellipsoids at the 50% probability level.

The adjacent WTe_2 layers are arranged in a mirror-like fashion across the bromine-containing interlayer plane. The average W-W separation of $2.909(2)$ Å is slightly expanded relative to pristine WTe_2 . In contrast to WTe_2 , where a more continuous halogen layer separates adjacent WTe_2 layers, $\text{WTe}_2\text{Br}_{0.5}$ contains only half as many halogens and the bromine position is shifted such that bromine atoms align along the a -axis with the tungsten-chain-bridging tellurium atom Te1, giving a short Te1–Br1 contact of $2.946(2)$ Å that connects neighboring WTe_2 layers. When projected onto the bc -plane, the bromine positions define a rectangular net with Br⋯Br separations fixed by the lattice dimensions ($3.6773(1)$ Å along b and $6.297(1)$ Å along the c -axis); these relatively long distances make direct Br⋯Br interactions inefficient.

A defining feature in the structure of $\text{WTe}_2\text{Br}_{0.5}$ is the exceptionally large anisotropic displacement of the bromine atom Br1, which occupies the Wyckoff 2b position with $mm2$ site symmetry. The bromine atom refines with $U_{\text{iso}} = 0.115(7)$ Å², and anisotropic atomic-displacement parameter (ADP) refinement reveals a pronounced directional character ($U_{11} = 0.145(9)$ Å², $U_{22} = 0.036(5)$ Å², $U_{33} = 0.163(7)$ Å²) with the largest components along a - and c -direction and only a minor component along b . Attempts to improve the description by splitting the bromine position or refining the site occupancy did not yield a better model and were therefore not pursued further. These unusually large and anisotropic ADPs indicate that bromine is not sharply localized but exhibits pronounced positional disorder and/or dynamic motion within the van der Waals gap, resulting in an averaged, “smeared” electron density of bromine atoms. This crystallographic signature is consistent with the high bromine mobility inferred from the rapid and reversible bromine exchange (“breathing”) behavior observed for the WTe_2Br_x system. While the present X-ray powder diffraction

data are adequately described by the average $Pmmn$ model, the presence of a weak superstructure or subtle incommensurate modulation cannot be fully excluded.

Crystal structure of $\text{WTe}_2\text{Br}_{1.25}$

At the maximum bromine content realized in this series, the compound $\text{WTe}_2\text{Br}_{1.25}$ is obtained, which crystallizes in the orthorhombic space group $Imm2$ with refined lattice parameters $a = 10.6218(4)$ Å, $b = 43.038(3)$ Å, and $c = 12.6285(9)$ Å. The structure was determined from single-crystal X-ray diffraction at 150 K and was identified as an inversion twin (see Table 2). All measured crystals exhibited twin domains with refined Flack parameters close to 0.5. Due to multiple phase transitions during bromine uptake the resulting crystallinity is reduced and the refinement quality is modest (see Figure S6). In addition, the structural model was used for Rietveld refinement of the bulk powder sample, yielding good agreement with the experimental pattern (see Figure S7). Given the large unit cell and number of atoms, the structure refinement from PXRD data was carried out with fixed atomic coordinates, refining only lattice parameters and profile functions.

Table 2: Crystallographic data and details from single-crystal X-ray refinement for $\text{WTe}_2\text{Br}_{1.25}$.

Compound	$\text{WTe}_2\text{Br}_{1.25}$
CCDC	2438541
Formula	$\text{W}_{24}\text{Te}_{48}\text{Br}_{30}$
Formula weight / $\text{g}\cdot\text{mol}^{-1}$	12934.50
Density / $\text{g}\cdot\text{cm}^{-3}$	7.441
Z	2
Crystal system	orthorhombic
Space group	$Imm2$
a / Å	10.6218(4)
b / Å	43.038(3)
c / Å	12.6285(9)
V / Å ³	5773.0(6)
T / K	150.0(1)
Radiation type	Cu- $K\alpha$
Reflections measured	25309
Independent reflections	4856
Abs. coeff. (mm^{-1})	148.873
Goof (F^2)	1.046
R_{int}	0.0736
R_1	0.1363
wR_2	0.2842
Flack	0.56(6)

In contrast to the uniform stacking sequence in $\text{WTe}_2\text{Br}_{0.5}$, $\text{WTe}_2\text{Br}_{1.25}$ adopts a structure in which two distinct bromine layer types alternate periodically within the van der Waals (vdW) gaps between adjacent WTe_2 layers, leading to a doubling of the b -axis (see Figure 13). An interesting feature of the structure is that one vdW interlayer contains 0.5 Br, the other 0.75 Br per WTe_2 formula unit, corresponding with interlayer distances of $10.1573(2)$ Å and $11.3493(2)$ Å.

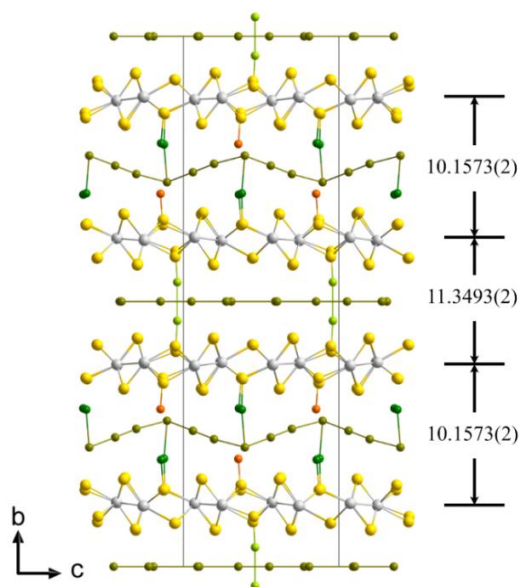


Figure 13. Section of the $\text{WTe}_2\text{Br}_{1.25}$ crystal structure viewed along the a -direction (W: grey, Te: yellow, Br: light green/green/olive/orange). Bromine atoms are shown in different colors to distinguish the individual bromine sites and to highlight the polybromide motifs.

The WTe_2 layers in $\text{WTe}_2\text{Br}_{1.25}$ are largely preserved and retain the characteristic zig-zag arrangement of tungsten atoms within a distorted WTe_2 layer. However, the W–W distances within the zig-zag chains are not equidistant, reflecting a distortion of the WTe_2 layers. Specifically, five consecutive tungsten atoms exhibit W–W distances along the crystallographic a -direction in the typical range of ~ 2.79 Å ($2.771(9)$ – $2.815(9)$ Å), followed by two distinctly elongated W–W contacts of approximately ~ 2.94 Å ($2.925(9)$ Å and $2.954(9)$ Å, see Figure 14).

The bromine interlayer containing 0.5 Br atoms per WTe_2 formula unit adopts an essentially planar arrangement, however, containing some out of plane Br_2 dumbbells (Br_7) aligned parallel to the b -axis (Figure 15, light green colored atoms), as present in the planar halogen layer observed in the commensurate WTe_2 structure (Figure 8). The out of plane bromine dumbbells, with a Br–Br distance of $3.13(4)$ Å, establish directional contacts with Te atoms of the WTe_2 layers, via interlayer Te–Br contacts of $2.50(3)$ Å. This interaction, based on Br_7 , has an impact on the W–W distances along zig-zag chains (W_1 – W_4), as visualized in Figure 14 with the longer W–W bonds shown as dashed lines.

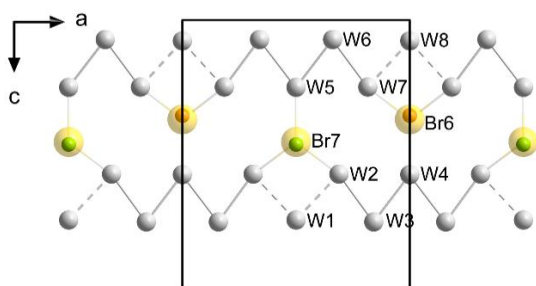


Figure 14. Section of the $\text{WTe}_2\text{Br}_{1.25}$ structure viewed along the b -axis with the unit cell highlighted. For clarity, only one interlayer section in the ac -plane of the tungsten zig-zag chains is shown. Tellurium atoms are omitted, except for Te atoms bonded to the WTe_2 layer as well as Br atoms, which are included. Note that Br_7

and Br_6 belong to different bromine interlayers, above and below the projected plane of W atoms. Elongated W–W contacts, indicating disruption of the tungsten chain, are highlighted by dashed lines (W: grey, Te: yellow, Br: light green/orange).

Bromine atoms within this layer organize into a rectangular network, with Br···Br separations ranging from $2.51(4)$ Å to $4.42(6)$ Å (Figure 15). The displacement parameters of the bromine atoms within the rectangular network (Br_{10} – Br_{13}) behave strongly anisotropic, being extended in the ac -plane, suggesting significant positional flexibility—possibly dynamic behavior—and may indicate a tendency toward local modulation or multiple orientations of the bromine atoms.

The bromine interlayer containing 0.75 bromine per WTe_2 formula unit hosts a more complex arrangement involving polybromide species. Within this vdW interlayer, three distinct types of bromine motifs can be distinguished (see Figure 13 and Figure 16). First, a single bromine atom (Br_6 in Figure 14, orange color) is observed in close contact with a tellurium atom in the adjacent WTe_2 layer, with a Br_5 – Te_{12} distance of $2.48(3)$ Å, which perturbs the crystallographic W–W chain (W_5 – W_8 ; Figure 14). Second, a linear chain of bromine atoms is also found interacting with the WTe_2 layer (Figure 13 green colored atoms), but without visibly perturbing the WTe_2 layers. Third, a more complex, square-pyramidal arrangement of bromine atoms is located fully within the interlayer space, forming a layer through edge-sharing connections (Figure 13, olive colored atoms). These bromine atoms show no direct bonding to the surrounding WTe_2 framework but are connected into the polybromide chain through the apex bromine atom Br_1 . All Br–Br distances fall within the expected range for polybromide species (2.30 – 3.67 Å)^{51–53}, spanning from $2.36(3)$ Å to $3.56(2)$ Å, with the shortest contacts observed at the bridging Br_2 unit between two apex bromine atoms.

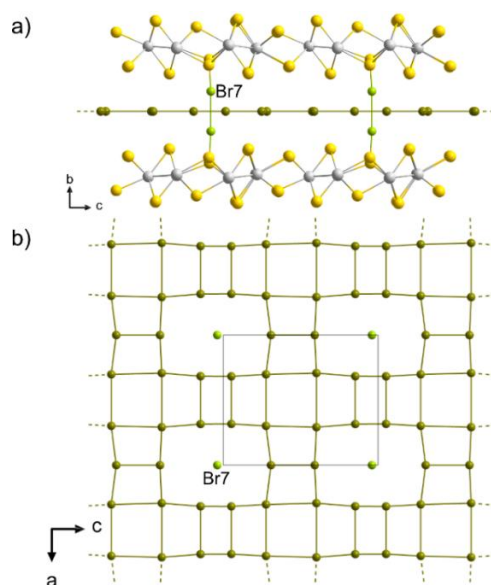


Figure 15. Section of the crystal structure of $\text{WTe}_2\text{Br}_{1.25}$ showing interlayer bromine atoms (0.5 Br per formula unit WTe_2) a) between adjacent WTe_2 layers and b) the same bromine net viewed along the b -direction. (W: grey, Te: yellow, Br: green/olive). The Br_2 dumbbells (Br_7) connecting adjacent WTe_2 layers are aligned along the b -axis and highlighted green.

The atomic displacement parameters of these polybromide sites are relatively normal but slightly increased compared to those of the WTe_2 framework atoms. In contrast to the bromine layer forming the rectangular net, the ADPs here are less anisotropic and suggest limited flexibility or positional variation of the bromine atoms within the polybromide layer.

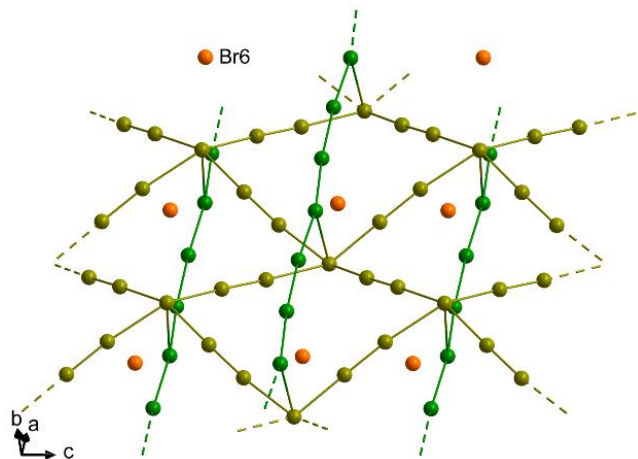


Figure 16. Section of the crystal structure of $WTe_2Br_{1.25}$ showing interlayer bromine atoms (0.75 Br per formula unit) between adjacent WTe_2 layers. For visual clarity, distinct bromine motifs are color-coded. The bromine atoms (Br6) connecting to adjacent WTe_2 layers are highlighted in orange

Crystal structure of WTe_2Br

Given the structural models of $WTe_2Br_{1.25}$, $WTe_2Br_{0.5}$ and WTe_2I , it is reasonable to assume that the intermediate phase $WTe_2Br_{1.0}$ adopts a closely related structure. Specifically, the interlayer region is expected to feature the same bromine arrangement as observed in the 0.5 Br per formula unit bromine layer configuration of $WTe_2Br_{1.25}$, i.e., a planar halogen layer composed of Br_2 -like units aligned with the tungsten-chain-bridging tellurium atoms. As such, $WTe_2Br_{1.0}$ likely exhibits a uniform stacking sequence with each van der Waals gap containing the same halogen motif. This would resemble the commensurate stacking found in WTe_2I and represents a structurally balanced state between the alternating-filled architecture of $WTe_2Br_{0.5}$ and the polybromide-rich environment of $WTe_2Br_{1.25}$. Due to the fast and reversible intercalation behavior and high mobility of bromine in this system, isolation of pure $WTe_2Br_{1.0}$ remains challenging, and a final structural characterization has not yet been achieved.

Electronic Band Structure of WTe_2I

The electronic band structure was calculated by density functional theory (DFT) for the 3D WTe_2I supercell model derived from the commensurate refinement, which can be regarded as equivalent descriptions (shown in Figure 17). In comparison to the band structure of unintercalated WTe_2 in the $P2_1/m$ space group which is a semimetal,³⁴ WTe_2I shows metallic behavior due to a downward shift in energy of tungsten orbitals between A ($-\frac{1}{2} 0 \frac{1}{2}$) and E ($-\frac{1}{2} \frac{1}{2} \frac{1}{2}$). The oxidation of the WTe_2 network by iodine is quite minimal, with a downward shift of the Fermi energy of only 0.04 eV.

The electronic structure of the unmodulated $Pm\bar{m}n$ structure of WTe_2I ($a = 21.8967(2)$ Å, $b = 3.4759(0)$ Å, $c = 6.3270(1)$ Å) has been previously reported.^{49, 50} The unmodulated structure is also metallic, but shows several important differences to the supercell structure: a much higher degree of oxidation of the WTe_2 layers, and the presence of iodine bands with high dispersion crossing the Fermi level. These crossing bands lead to nesting of the Fermi surface and charge density wave (CDW) instabilities, which create the modulated structures that we have characterized here.

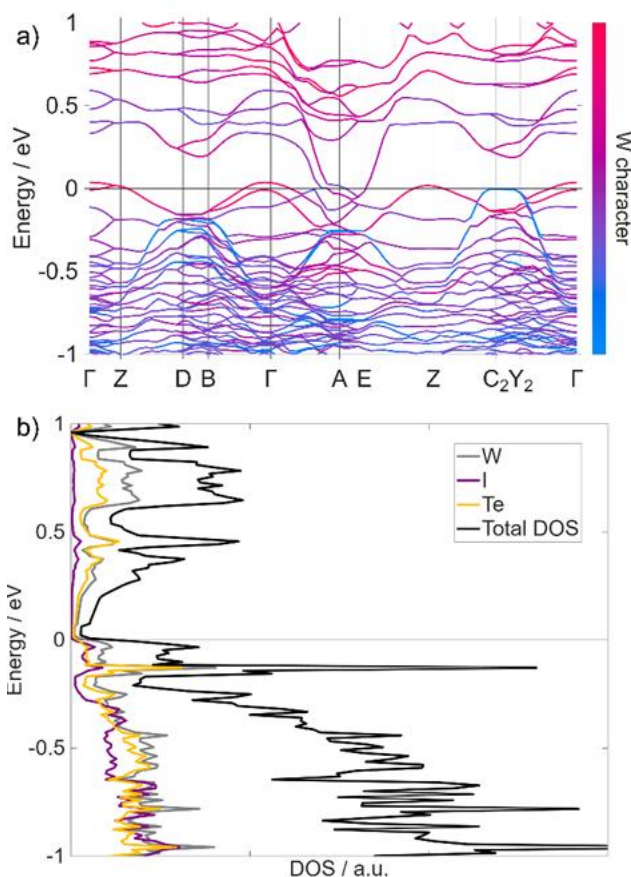


Figure 17. Calculated electronic band structure of commensurately modulated WTe_2I , with bands colored by their tungsten character (a), and the corresponding electronic density of states (b). Special points in and paths through reciprocal space were chosen following the literature.⁵⁴

In supercell WTe_2I structure, some iodine states form a flat band at the Fermi energy between C_2 ($-\frac{1}{2} \frac{1}{2} 0$) and Y_2 ($-\frac{1}{2} 0 0$) (shown in blue in Figure 17). The flatness of this band indicates a very high degree of electron localization. When moving away from the C_2 - Y_2 line, the band takes a parabolic form with many anticrossings of the W bands, which demonstrates strong coupling between the I and W states. This band is associated with the iodine atoms I2, I8 and I5, I11 which correspond to I1 and I2 in the commensurate structure at specific internal phase coordinate t (see Figure 18, highlighted in red). The overall picture is of localized metallic electrons on some portions of the iodine layer, potentially representing frozen CDWs.⁴⁹

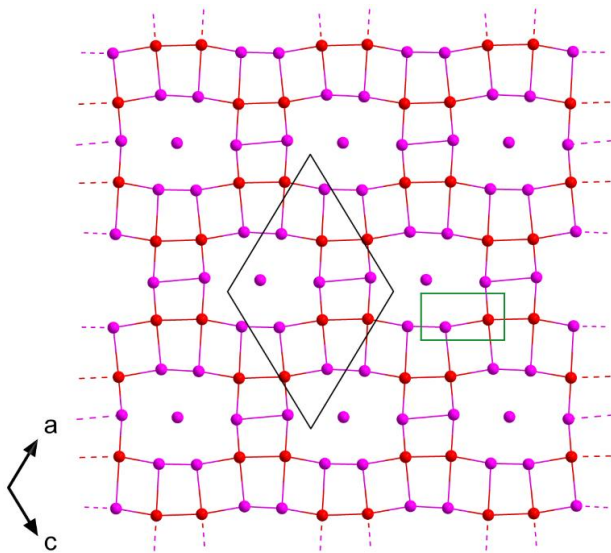


Figure 18. Section of the WTe_2I supercell structure only showing one iodine (red/purple) layer with highlighted I2, I8 and I5, I11 iodines in red with viewing direction along the b -axis. Unit cells are shown in black (supercell) and green (commensurate).

Electronic Band Structure and Phonon Band Structure of $WTe_2Br_{0.5}$

The electronic band structure of $WTe_2Br_{0.5}$ was also calculated using density functional theory (DFT) (Figure 19). Like WTe_2I , $WTe_2Br_{0.5}$ is a metal, with additional bands appearing near the Fermi energy compared to WTe_2 .⁴⁹ These include an interesting flat band at the Fermi energy between X ($\frac{1}{2}$ 0 0) and S ($\frac{1}{2}$ $\frac{1}{2}$ 0); however, unlike in the case of WTe_2I , there is no contribution of the Br atoms to the states near the Fermi energy, and therefore these localized metallic electrons are located within the WTe_2 layers. $WTe_2Br_{0.5}$ shows a higher degree of oxidation of the WTe_2 layers than modulated WTe_2I , with a shift of the Fermi energy of 0.35 eV, indicating a more ionic interaction with the intercalant.

The phonon band structure of $WTe_2Br_{0.5}$ was also calculated; it is shown in Figure 20. Like unmodulated WTe_2I ,⁴⁹ $WTe_2Br_{0.5}$ shows many soft modes (modes with negative energy), corresponding to instabilities of the crystal structure at 0 K. These soft modes include both displacements of the Br atoms and of the WTe_2 layers. Therefore, $WTe_2Br_{0.5}$, like WTe_2I , has a propensity towards the formation of a disordered or modulated structure.

The observation of an unmodulated structure for $WTe_2Br_{0.5}$, in comparison to the modulated structure of WTe_2I , can be understood by consideration of the electronic band structure. $WTe_2Br_{0.5}$ lacks the extra sheet-like bands crossing the Fermi level which lead to the formation of CDWs, CDW instabilities, and a modulated structure in WTe_2I .⁴⁹ Therefore, the phonon instabilities in $WTe_2Br_{0.5}$ likely cause dynamic and/or static disorder, as is seen in the large ADPs. The high density of Br states below 10 meV would also contribute thermal displacements to the ADPs, although these modes contain displacements of the Br atoms in all three Cartesian directions.

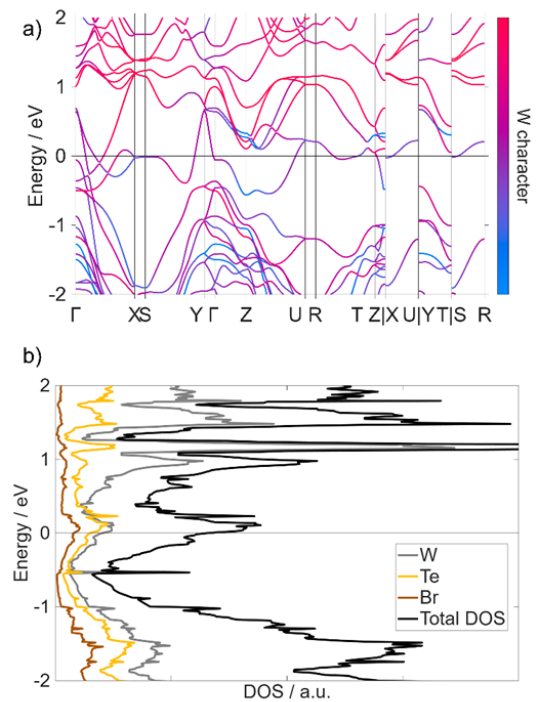
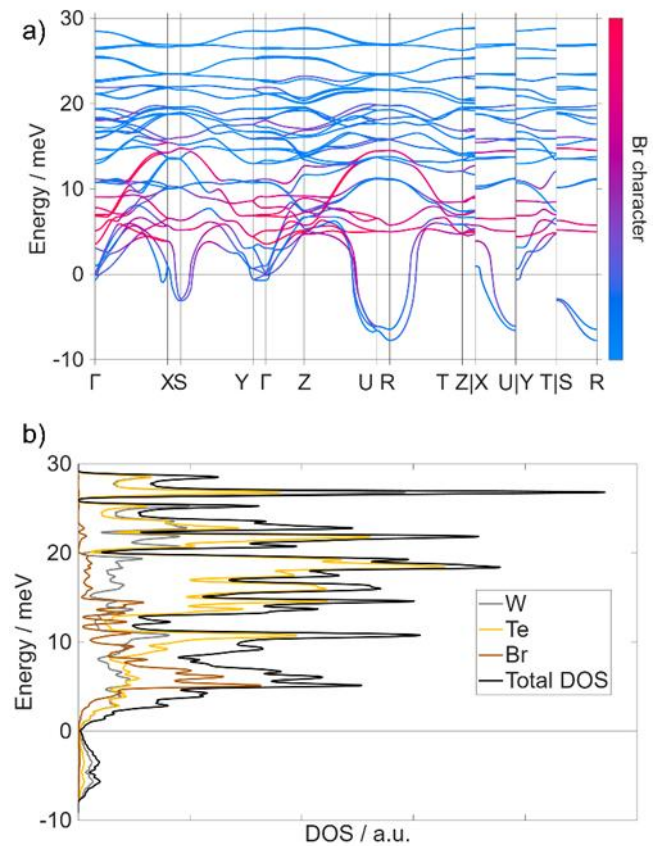


Figure 19. Calculated electronic band structure of $WTe_2Br_{0.5}$, with bands colored by their tungsten character (a), and the corresponding electronic density of states (b). Special points in and paths through reciprocal space were chosen following the literature.⁵⁴



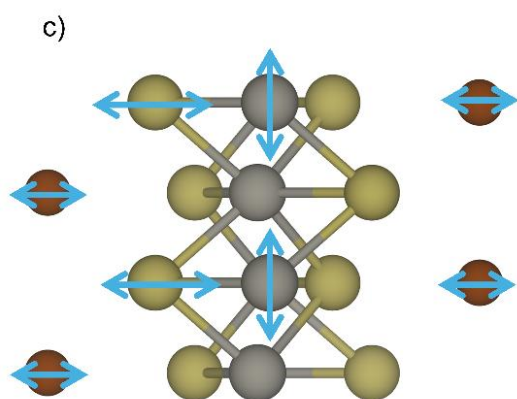


Figure 20. Calculated phonon band structure of $\text{WTe}_2\text{Br}_{0.5}$, with bands colored by their bromine character (a), and the corresponding phonon density of states (b). A cartoon view of an unstable mode at R (0.5 0.5 0.5) along c is shown in (c). Special points in and paths through reciprocal space were chosen following the literature.⁵⁴

Experimental

Synthesis: All material handling and manipulations were performed in an argon-filled glove box (MBraun Labmaster 130, $\text{O}_2 < 1$ ppm, $\text{H}_2\text{O} < 1$ ppm). All synthesis steps consistently afforded yields greater than 95%.

Powder: WTe_2 was synthesized by combining tungsten powder (1256.24 mg, 6.84 mmol, ABCR GmbH, 99.95%, particle size 0.6–0.9 μm), tellurium pieces (1830.95 mg, 14.35 mmol, Evochem, 99.999%), and tungsten(VI) chloride (WCl_6 ; 135.49 mg, 0.34 mmol, Arcos, 99.9+%) in a 1:2.1:0.05 molar ratio, with WCl_6 serving as an oxygen getter. The mixture was sealed in a dry, evacuated silica ampoule (40 mm length, 16 mm diameter) and heated in a commercial (Carbolite) furnace to 800 °C for 6 hours, employing heating and cooling rates of 2 K/min. The resulting product was thoroughly ground, vacuum-sealed in a second silica ampoule (200 mm length, 16 mm diameter), and heated to 500 °C for 20 hours under a temperature gradient, with the opposite end of the ampoule maintained at room temperature, to facilitate the removal of excess tellurium, tungsten oxychloride impurities and unreacted WCl_6 .

Single crystals of WTe_2 was synthesized by combining tungsten powder (1256.24 mg, 6.84 mmol, ABCR GmbH, 99.95%, particle size 0.6–0.9 μm), tellurium pieces (1830.95 mg, 14.35 mmol, Evochem, 99.999%), and tungsten(VI) chloride (WCl_6 ; 135.49 mg, 0.34 mmol, Arcos, 99.9+%) in a 1:2.1:0.05 molar ratio, with WCl_6 serving as an oxygen getter. The mixture was sealed in a dry, evacuated silica ampoule (40 mm length, 16 mm diameter) and heated in a commercial (Carbolite) furnace to 800 °C for 6 hours, employing heating and cooling rates of 2 K/min.

WTe_2 I crystals: WTe_2 single-crystals (~100 mg) were loaded into a borosilicate glass screw-cap vial (5/20 mL for incommensurate/commensurate crystals) with four molar equivalents of iodine, and the vial was sealed with a custom-machined PEEK cap equipped with a PTFE liner. The reaction mixture was heated in

a Simon-Müller laboratory oven at a rate of 2 $\text{K}\cdot\text{min}^{-1}$ to 120 °C, held at this temperature for 12 h, and then cooled to room temperature at the same rate.

WTe_2Br_x ($x = 0.5$ and 1.25): Bromine (p.a.) was degassed and purified prior to use according to Brauer.⁵⁵ Due to the corrosive nature and high vapor pressure of bromine, all operations were performed either in an argon glovebox or using Schlenk techniques under dry argon (with appropriate cold traps). Typically, WTe_2 (powder or single crystals, ca. 100 mg) was reacted with a large excess of bromine (ca. 3 mL). WTe_2 powder was placed in a Schlenk tube, liquid bromine was added and the mixture was allowed to react for 3 h. Excess bromine was then removed by passing a constant argon flow over the sample. Because of the high density of bromine vapors, a needle was inserted through the septum and positioned directly above the sample to provide an efficient outlet for the Br_2 /argon vapors and the vessel was gently shaken from time to time. For $\text{WTe}_2\text{Br}_{0.5}$, evaporation at room temperature was sufficient, whereas for $\text{WTe}_2\text{Br}_{1.25}$ the Schlenk tube was cooled to 0–5 °C during the bromine removal step and needed at least 3 h. Needle-shaped WTe_2 single crystals were intercalated either (i) by exposure to bromine vapor at room temperature for 4 days or (ii) by direct contact with liquid bromine at 6 °C for 2 days.

Powder X-ray diffraction: PXRD patterns of products were collected with a Stadi-P (STOE, Darmstadt) powder diffractometer using germanium monochromated $\text{Cu-K}\alpha_1$ radiation ($\lambda = 1.5406$ Å) and a Mythen 1K detector. PXRD measurements of WTe_2Br_x ($x = 0.5, 1.0,$ and 1.25) were performed in transmission geometry using interchangeable window materials selected according to the experimental requirements. The windows comprised ultrathin glass (Schott AF 32® eco thin glass, 30 μm), Kapton® film (25 μm), and Mylar® film (15 μm). To prevent corrosion by bromine and to enable reliable sealing, the metal parts of the original transmission holder were replaced by custom-made PTFE components (rotor disc and counter disc) and soda-lime glass components in a redesigned holder (see Figure S8 and S9). In all experiments, WTe_2 powder was immobilized on the glass window using Lithelen grease to ensure a fixed sample position during measurement, and all samples were assembled and sealed under inert conditions (argon atmosphere). For $\text{WTe}_2\text{Br}_{0.5}$, a standard glass disc without a filling slit was employed; the sample was covered with a Kapton® film window that was sealed using Lithelen grease and allowed gradual pressure equilibration via bromine diffusion through the Kapton film (see Figure S8 a) and d)). For $\text{WTe}_2\text{Br}_{1.25}$, a glass disc featuring a filling slit was used; ultrathin-glass windows were bonded to both sides of the disc using cyanoacrylate adhesive (superglue). Bromine was introduced through the slit under argon, and the opening was subsequently sealed with wax and additional cyanoacrylate. For in situ PXRD experiments, Mylar film was used as the window material to facilitate faster bromine release during the measurement. The crystal structure of $\text{WTe}_2\text{Br}_{0.5}$ was solved from PXRD using EXPO2014,⁵⁶ and refined by Rietveld method in FullProf (FP)⁵⁷ with a modified Thompson-Cox-Hastings pseudo-Voigt (TCHZ) profile function.^{58, 59} The instrumental resolution function (IRF) was obtained from the NIST Si640f

standard⁶⁰ and fitted in WinPLOTR.⁶¹ Additionally, multiple texturing effects, such as particle form, size, and orientation, were included in the Rietveld refinements to enhance the accuracy of the model. All intermediate and final structure models were validated with PLATON.⁶²

Single-Crystal X-Ray Diffraction (SC-XRD): SC-XRD studies were performed using a Rigaku XtaLAB Synergy-S diffractometer equipped with a HyPix 6000HE detector using MoK α ($\lambda = 0.71073 \text{ \AA}$) and CuK α ($\lambda = 1.54184 \text{ \AA}$) radiation at 150 K. Data reduction, scaling and absorption corrections were performed using CrysAlisPro.⁶³, taking into account the crystal shape and size.⁶⁴ The supercell structure of WTe₂I and WTe₂Br_{1.25} were solved with the ShelXT 2018/2 solution program⁶⁵, employing dual methods and refined with ShelXL 2018/3 (Sheldrick, 2015)⁶⁶ using Olex2 1.5 (Dolomanov et al., 2009)⁶⁷ as the graphical interface. The models were refined using full matrix least squares minimization on $|F|^2$. For WTe₂Br_{1.25} crystals, the needle shaped WTe₂ single crystals were selected directly from bromine layered with perfluoropolyalkylether (viscosity 1800 cSt; ABCR GmbH). The modulated WTe₂I structures were solved using the charge-flipping algorithm SUPERFLIP⁶⁸ (as implemented in JANA2020), and subsequent refinements were carried out in JANA2020.⁶⁹⁻⁷²

ICP-OES: After dissolution of WTe₂I in 2 wt % NaOH/H₂O₂, the W/Te/I ratio was determined by ICP-OES (iCAP 7400 Thermo Fisher Scientific) and yielded in averaged ratios W:Te:I of 1.0 : 1.99(3):0.49(3) for WTe₂I phases.

TXRF (Total Internal Reflection X-Ray Fluorescence) Spectroscopy: TXRF studies were performed using a S2 Picofox (Bruker AXS Microanalysis, Berlin, Germany) equipped with a Mo X-ray tube, which was operated at 50 kV and 600 μ A. The measurement period for each sample was 1000 s (live time). Fitting of the resulting spectra was done using the Spectra software (Bruker Nano GmbH) in the super byas mode (maximum stripping cycles of 2000). The average ratio for WTe₂I with W:Te:I was 1.0 : 1.98(7):0.51(6).

Bromide Content Determination (Argentometric Titration): Approximately 100 mg of WTe₂Br_{0.5} was dissolved in concentrated HNO₃ (5 mL) with addition of \sim 1 mL of H₂O₂ (30%). The mixture was carefully heated to ca. 80 °C for 30 min, allowed to cool to room temperature, and diluted with bidistilled H₂O to a final volume of 100 ml. The bromide content was determined by argentometric titration with potentiometric end-point detection using a standardized AgNO₃ solution (0.01 M). Titrations were performed on a Schott TitroLine easy automatic titrator (SI Analytics) equipped with a silver indicator electrode. The equivalence point was identified from the inflection in the electrode potential (mV), corresponding to complete precipitation of Br⁻ as AgBr. Repeated determinations gave bromide contents consistent with the expected composition of WTe₂Br_{0.5} (W:Br = 1:0.49(3)).

DFT Calculations: Calculations were performed using the ABINIT software package with the projector augmented-wave (PAW) method and a plane-wave basis set.^{73, 74} The Perdew–Burke–Ernzerhof exchange–correlation functional was used with the vdW–DFT–D3 dispersion correction.^{75, 76} PAW data files were used as received from the ABINIT library.⁷⁷ Methfessel–

Paxton smearing was used to determine band occupation.⁷⁸ Convergence studies were used to choose a 18 Ha (WTe₂I) and 20 Ha (WTe₂Br_{0.5}), plane wave basis set cutoff energy outside the PAW spheres; a 100 Ha cutoff was used within the spheres. The Brillouin zone was sampled with a 4 \times 2 \times 4 (WTe₂I) or 6 \times 10 \times 6 (WTe₂Br_{0.5}) grid of k-points. The calculation of the phonon band structure of WTe₂Br_{0.5} was performed using density functional perturbation theory on a 3 \times 5 \times 3 grid of q-points. Structural relaxation was performed prior to calculation of the electronic and phononic structures.

Conclusions

In this work, the crystal structure of the iodine intercalate WTe₂I was reinvestigated and shown to occur in two closely related (3+1)D variants within $P2_1/m(\alpha 0 \gamma)00$: an incommensurate form and a commensurate polytype that “locks in” to $\mathbf{q} = (1/2, 0, 1/6)$ and can be equivalently described as a 3D supercell. In both descriptions, the modulation is dominated by the iodine sublattice, while the WTe₂ host responds only by subtle, coupled distortions. A key microscopic element is a local defect motif in which an I2 unit reorients by 90° (I3 site) and is accommodated by a concomitant Te shift, consistent with localized host–guest bonding that effectively pins the modulation and periodically perturbs the tungsten chains.

Extending this chemistry from iodine to bromine, we identify a multistage series WTe₂Br _{x} with distinct regimes at $x = 0.5, 1.0$ and 1.25 and a striking, fast, and reversible “breathing” behavior already at room temperature. In situ PXRD directly captures the rapid evolution of the layer-spacing reflections during uptake and release, demonstrating that composition and structure can be cycled under mild conditions. Structurally, WTe₂Br_{0.5} ($Pm\bar{m}n$) represents a bromine-poor end member with a half-filled interlayer motif and a short Te–Br contact that links adjacent layers; its exceptionally large, anisotropic bromine displacement parameters point to pronounced positional freedom consistent with high bromine mobility. At the bromine-rich end, WTe₂Br_{1.25} ($Imm2$) adopts an alternating-filled architecture with two chemically distinct interlayer environments, combining Br₂-like bridging motifs and more complex polybromide arrangements, while the WTe₂ framework remains intact but locally distorted in response to directional Te–Br interactions. In both WTe₂I and WTe₂Br_{0.5}, the electronic structure of the WTe₂ layers is changed significantly by intercalation, leading to a metallic state with localized electrons in flat bands at the Fermi level. Together, these results establish WTe₂I and WTe₂Br _{x} as rare, structurally resolved examples of stoichiometric halogen intercalation in a TMDC, highlighting how a layered semimetal can tolerate strong oxidizing guests while retaining topotactic reversibility—opening a route to controllable oxidation (hole doping), staging, and modulation phenomena in van der Waals solids.

Conflicts of interest

There are no conflicts to declare.

Data availability

Crystallographic data have been deposited at the Cambridge Crystallographic Data Centre (CCDC) under 2520418 (WTe₂I, incommensurate), 2519690 (WTe₂I, commensurate), 2519736 (WTe₂I, supercell), 2503030 (WTe₂Br_{0.5}), 2519455 (WTe₂Br_{1.25}). Data are available within the article. The data that support the findings of this study are available on request from the corresponding author, H.-J. Meyer. Computational data are available at doi:10.5281/zenodo.18420902.

Acknowledgements

The authors acknowledge support of this research by the Deutsche Forschungsgemeinschaft (Bonn) through the project ME 914/32-1 and by the state of Baden-Württemberg through bwHPC and the German Research Foundation (DFG) through grant no INST 40/575-1 FUGG (JUSTUS 2 cluster). Carl P. Romao acknowledges support from the project FerrMion of the Ministry of Education, Youth and Sports, Czech Republic, co-funded by the European Union (CZ.02.01.01/00/22_008/0004591).

References

1. H. Yang, S. W. Kim, M. Chhowalla and Y. H. Lee, *Nat. Phys.*, 2017, **13**, 931–937.
2. M. Chhowalla, D. Jena and H. Zhang, *Nat. Rev. Mater.*, 2016, **1**, 16052.
3. M. Chhowalla, *Nat. Chem.*, 2013, **5**, 263–275.
4. J. A. Wilson and A. D. Yoffe, *Adv. Phys.*, 1969, **18**, 193–335.
5. M. S. Whittingham, *Chem. Rev.*, 2004, **104**, 4271–4302.
6. M. S. Whittingham, *Prog. Solid State Chem.*, 1978, **12**, 41–99.
7. Z. Wang, R. Li, C. Su and K. P. Loh, *SmartMat*, 2020, **1**, e1013.
8. M. N. Ali, H. Ji, D. Hirai, M. K. Fuccillo and R. J. Cava, *J. Solid State Chem.*, 2013, **202**, 77–84.
9. S. I. Ali, S. Mondal, S. J. Prathapa, S. van Smaalen, S. Zörb and B. Harbrecht, *Z. Anorg. Allg. Chem.*, 2012, **638**, 2625–2631.
10. S. I. Ali, S. Mondal and S. van Smaalen, *Z. Anorg. Allg. Chem.*, 2015, **641**, 464–469.
11. H. J. Crawack and C. Pettenkofer, *Solid State Commun.*, 2001, **118**, 325–332.
12. J. Rouxel, *Physica B+C*, 1980, **99**, 3–11.
13. S. N. Patel and A. A. Balchin, *J. Mater. Sci. Lett.*, 1985, **4**, 382–384.
14. M. B. Dines, *Science*, 1975, **188**, 1210.
15. E. Figueroa, J. W. Brill and J. P. Selegue, *J. Phys. Chem. Solids*, 1996, **57**, 1123–1127.
16. Y. Liu, Z. Wang, G. Hu, X. Chen, K. Xu, Y. Guo, Y. Xie and C. Wu, *Precis. Chem.*, 2025, **3**, 51–71.
17. S. Kabashima, *J. Phys. Soc. Jpn.*, 1966, **21**, 945–948.
18. J. Augustin, *Phys. Rev. B*, 2000, **62**, 10812–10823.
19. W. G. Dawson and D. W. Bullett, *J. Phys. C Solid State Phys.*, 1987, **20**, 6159–6174.
20. Y.-Y. Lv, B.-B. Zhang, X. Li, B. Pang, F. Zhang, D.-J. Lin, J. Zhou, S.-H. Yao, Y. B. Chen, S.-T. Zhang, M. Lu, Z. Liu, Y. Chen and Y.-F. Chen, *Sci. Rep.*, 2016, **6**, 26903.
21. H. Y. Lv, W. J. Lu, D. F. Shao, Y. Liu, S. G. Tan and Y. P. Sun, *Europhys. Lett.*, 2015, **110**, 37004.
22. P. Li, Y. Wen, X. He, Q. Zhang, C. Xia, Z.-M. Yu, S. A. Yang, Z. Zhu, H. N. Alshareef and X.-X. Zhang, *Nat. Commun.*, 2017, **8**, 2150.
23. Y. Sun, S.-C. Wu, M. N. Ali, C. Felser and B. Yan, *Phys. Rev. B*, 2015, **92**, 161107.
24. C. Huang, A. Narayan, E. Zhang, Y. Liu, X. Yan, J. Wang, C. Zhang, W. Wang, T. Zhou, C. Yi, S. Liu, J. Ling, H. Zhang, R. Liu, R. Sankar, F. Chou, Y. Wang, Y. Shi, K. T. Law, S. Sanvito, P. Zhou, Z. Han and F. Xiu, *ACS Nano*, 2018, **12**, 7185–7196.
25. C. Rovira and M. H. Whangbo, *Inorg. Chem.*, 1993, **32**, 4094–4097.
26. J. A. Wilson, F. J. Di Salvo and S. Mahajan, *Adv. Phys.*, 1975, **24**, 117–201.
27. M. N. Ali, *Nature*, 2014, **514**, 205–208.
28. N. Lu, C. Zhang, C.-H. Lee, J. P. Oviedo, M. A. T. Nguyen, X. Peng, R. M. Wallace, T. E. Mallouk, J. A. Robinson, J. Wang, K. Cho and M. J. Kim, *J. Phys. Chem. C*, 2016, **120**, 8364–8369.
29. E. Canadell and M.-H. Whangbo, *Phys. Rev. B*, 1991, **43**, 1894–1902.
30. B. Guster, E. Canadell, M. Pruneda and P. Ordejón, *2D Mater.*, 2018, **5**, 025024.
31. M. H. Whangbo, E. Canadell, P. Foury and J. P. Pouget, *Science*, 1991, **252**, 96–98.
32. N. Mitsuishi, Y. Sugita, M. S. Bahramy, M. Kamitani, T. Sonobe, M. Sakano, T. Shimojima, H. Takahashi, H. Sakai, K. Horiba, H. Kumigashira, K. Taguchi, K. Miyamoto, T. Okuda, S. Ishiwata, Y. Motome and K. Ishizaka, *Nat. Commun.*, 2020, **11**, 2466.
33. B. E. Brown, *Acta Crystallogr.*, 1966, **20**, 268–274.
34. P. Schmidt, F. Strauß, M. Scheele, C. P. Romao and H.-J. Meyer, *Dalton Trans.*, 2026, **55**, 3296–3309.
35. H. Wang, Z. Lu, S. Xu, D. Kong, J. J. Cha, G. Zheng, P.-C. Hsu, K. Yan, D. Bradshaw, F. B. Prinz and Y. Cui, *Proc. Natl. Acad. Sci.*, 2013, **110**, 19701–19706.
36. M. B. Dines, *Mater. Res. Bull.*, 1975, **10**, 287–291.
37. L. Charron, D. Dumchenko, E. Fortin, C. Gherman and L. Kulyuk, *J. Lumin.*, 2005, **112**, 45–49.
38. D. S. Devi and N. R. Mohapatra, *ACS Omega*, 2024, **9**, 50634–50641.
39. Y. Garcia-Basabe, C. D. Mendoza, F. C. Vicentin and D. G. Larrude, *Phys. Chem. Chem. Phys.*, 2025, **27**, 19347–19357.
40. T. Kim, Y. Kim and E. K. Kim, *Sens. Actuators, A*, 2020, **312**, 112165.
41. L. Kulyuk, L. Charron and E. Fortin, *Phys. Rev. B*, 2003, **68**, 075314.
42. L. Kulyuk, D. Dumcehnko, E. Bucher, K. Friemelt, O. Schenker, L. Charron, E. Fortin and T. Dumouchel, *Phys. Rev. B*, 2005, **72**, 075336.
43. S. Pak, J. Son, T. Kim, J. Lim, J. Hong, Y. Lim, C.-J. Heo, K.-B. Park, Y. W. Jin, K.-H. Park, Y. Cho and S. Cha, *Nanotechnology*, 2023, **34**, 015702.
44. S. Prucnal, A. Hashemi, M. Ghorbani-Asl, R. Hübner, J. Duan, Y. Wei, D. Sharma, D. R. T. Zahn, R. Ziegenrucker, U. Kentsch, A. V. Krasheninnikov, M. Helm and S. Zhou, *Nanoscale*, 2021, **13**, 5834–5846.
45. M. Rabeel, H. Kim, M. A. Khan, M. Abubakr, I. Ahmad, M. Ahmad, S. Rehman, M.-J. Lee, M. F. Khan and D.-k. Kim, *ACS Photonics*, 2023, **10**, 4425–4436.
46. N. T. Trung, M. I. Hossain, M. I. Alam, A. Ando, O. Kitakami, N. Kikuchi, T. Takaoka, Y. Sainoo, R. Arafune and T. Komeda, *ACS Omega*, 2020, **5**, 28108–28115.
47. F.-Y. Wu, Y.-S. Cheng, K.-L. Wu, R. Wu, R. Yu, P.-L. Guan, Y.-W. Cheng, W.-J. Li, J.-L. Yang and X.-W. Wei, *J. Mater. Chem. C*, 2024, **12**, 6645–6652.
48. L. Yang, K. Majumdar, H. Liu, Y. Du, H. Wu, M. Hatzistergos, P. Y. Hung, R. Tieckelmann, W. Tsai, C. Hobbs and P. D. Ye, *Nano Lett.*, 2014, **14**, 6275–6280.
49. P. Schmidt, P. Schneiderhan, M. Ströbele, C. P. Romao and H.-J. Meyer, *Inorg. Chem.*, 2021, **60**, 1411–1418.
50. W. L. Zhu, Y. Cao, P. J. Guo, X. Li, Y. J. Chen, L. J. Zhu, J. B. He, Y. F. Huang, Q. X. Dong, Y. Y. Wang, R. Q. Zhai, Y. B. Ou, G. Q. Zhu, H. Y. Lu, G. Li, G. F. Chen and M. H. Pan, *Phys. Rev. B*, 2022, **105**, 125116.

51. K. Sonnenberg, L. Mann, F. A. Redeker, B. Schmidt and S. Riedel, *Angew. Chem. Int. Ed.*, 2020, **59**, 5464–5493.
52. H. Haller and S. Riedel, *Z. Anorg. Allg. Chem.*, 2014, **640**, 1281–1291.
53. H. Haller, J. Schröder and S. Riedel, *Angew. Chem. Int. Ed.*, 2013, **52**, 4937–4940.
54. Y. Hinuma, G. Pizzi, Y. Kumagai, F. Oba and I. Tanaka, *Comput. Mater. Sci.*, 2017, **128**, 140–184.
55. G. Brauer, *Handbuch der präparativen anorganischen Chemie*, Ferdinand Enke, Stuttgart, 1975.
56. A. Altomare, C. Cuocci, C. Giacovazzo, A. Moliterni, R. Rizzi, N. Corriero and A. Falcicchio, *J. Appl. Crystallogr.*, 2013, **46**, 1231–1235.
57. J. Rodriguez-Carvajal and T. Roisnel, *IUCr, CPD Newsl.*, 1998, **20**, 35–36.
58. P. Thompson, D. E. Cox and J. B. Hastings, *J. Appl. Crystallogr.*, 1987, **20**, 79–83.
59. L. W. Finger, D. E. Cox and A. P. Jephcoat, *J. Appl. Crystallogr.*, 1994, **27**, 892–900.
60. D. R. Black, M. H. Mendenhall, A. Henins, J. Filliben and J. P. Cline, *Powder Diffr.*, 2020, **35**, 156–159.
61. T. Roisnel and J. Rodríguez-Carvajal, *Mater. Sci. Forum*, 2001, **378–381**, 118–123.
62. A. Spek, *J. Appl. Crystallogr.*, 2003, **36**, 7–13.
63. *Journal*, 2025.
64. R. C. Clark and J. S. Reid, *Acta Crystallogr. Sect. A: Found. Crystallogr.*, 1995, **51**, 887–897.
65. G. Sheldrick, *Acta Crystallogr. Sect. A: Found. Crystallogr.*, 2015, **71**, 3–8.
66. G. Sheldrick, *Acta Crystallogr.*, 2015, **C71**, 3–8.
67. O. V. Dolomanov, L. J. Bourhis, R. J. Gildea, J. A. K. Howard and H. Puschmann, *J. Appl. Crystallogr.*, 2009, **42**, 339–341.
68. L. Palatinus and G. Chapuis, *J. Appl. Crystallogr.*, 2007, **40**, 786–790.
69. V. Petříček, M. Dušek and L. Palatinus, *Z. Kristallogr. Cryst. Mater.*, 2014, **229**, 345–352.
70. V. Petříček, M. Dušek and J. Plášil, *Z. Kristallogr. Cryst. Mater.*, 2016, **231**, 583–599.
71. V. Petříček, V. Eigner, M. Dušek and A. Čejchan, *Z. Kristallogr. Cryst. Mater.*, 2016, **231**, 301–312.
72. V. Petříček, L. Palatinus, J. Plášil and M. Dušek, *Z. Kristallogr. Cryst. Mater.*, 2023, **238**, 271–282.
73. X. Gonze, F. Jollet, F. Abreu Araujo, D. Adams, B. Amadon, T. Applencourt, C. Audouze, J. M. Beuken, J. Bieder, A. Bokhanchuk, E. Bousquet, F. Bruneval, D. Caliste, M. Côté, F. Dahm, F. Da Pieve, M. Delaveau, M. Di Gennaro, B. Dorado, C. Espejo, G. Geneste, L. Genovese, A. Gerossier, M. Giantomassi, Y. Gillet, D. R. Hamann, L. He, G. Jomard, J. Laflamme Janssen, S. Le Roux, A. Levitt, A. Lherbier, F. Liu, I. Lukačević, A. Martin, C. Martins, M. J. T. Oliveira, S. Poncé, Y. Pouillon, T. Rangel, G. M. Rignanese, A. H. Romero, B. Rousseau, O. Rubel, A. A. Shukri, M. Stankovski, M. Torrent, M. J. Van Setten, B. Van Troeye, M. J. Verstraete, D. Waroquiers, J. Wiktor, B. Xu, A. Zhou and J. W. Zwanziger, *Comput. Phys. Commun.*, 2016, **205**, 106–131.
74. M. Torrent, F. Jollet, F. Bottin, G. Zérah and X. Gonze, *Comput. Mater. Sci.*, 2008, **42**, 337–351.
75. J. P. Perdew, K. Burke and M. Ernzerhof, *Phys. Rev. Lett.*, 1997, **78**, 1396.
76. S. Grimme, J. Antony, S. Ehrlich and H. Krieg, *J. Phys. Chem.*, 2010, **132**, 154104.
77. www.abinit.org, (accessed 20/3/19).
78. M. Methfessel and A. T. Paxton, *Phys. Rev. B*, 1989, **40**, 3616–3621.

**Structural Evolution during Reversible Halogen Intercalation in WTe_2 :
Commensurate–Incommensurate WTe_2I and Multistage WTe_2Br_x ($x =$
0.5, 1.0 and 1.25)**

Patrick Schmidt,^a Carl P. Romao,^b Hans-Jürgen Meyer*^a

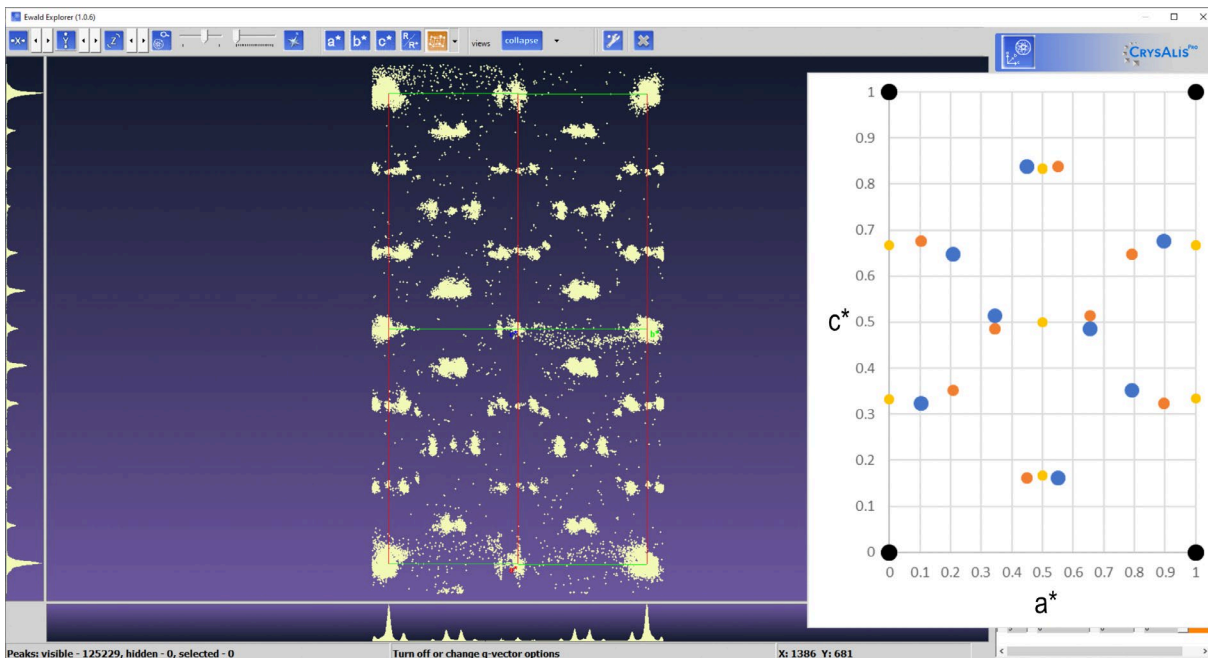


Figure S1. Screenshot from the Ewald Explorer in CrystallisPro showing the collapsed reciprocal lattice, with a simulated satellite pattern on the right (with $m \leq \pm 4$). Black dots mark the main reflections, while red and blue dots indicate incommensurate, twinned satellite reflections. Yellow dots denote the commensurate case.

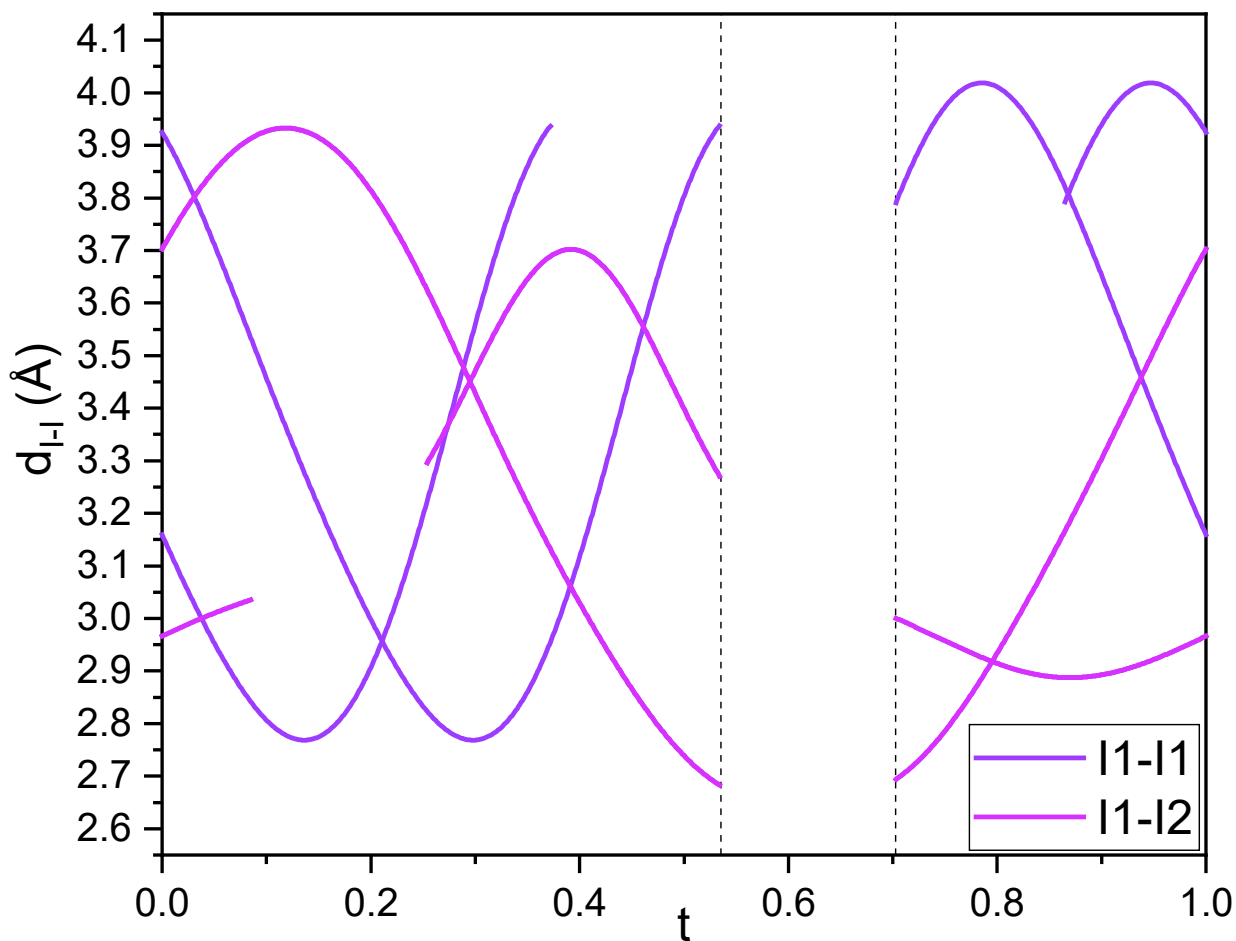


Figure S2. t plots of the distances for $l1-l1$ and $l1-l2$ in grey with crenel limits marked as dashed vertical line.

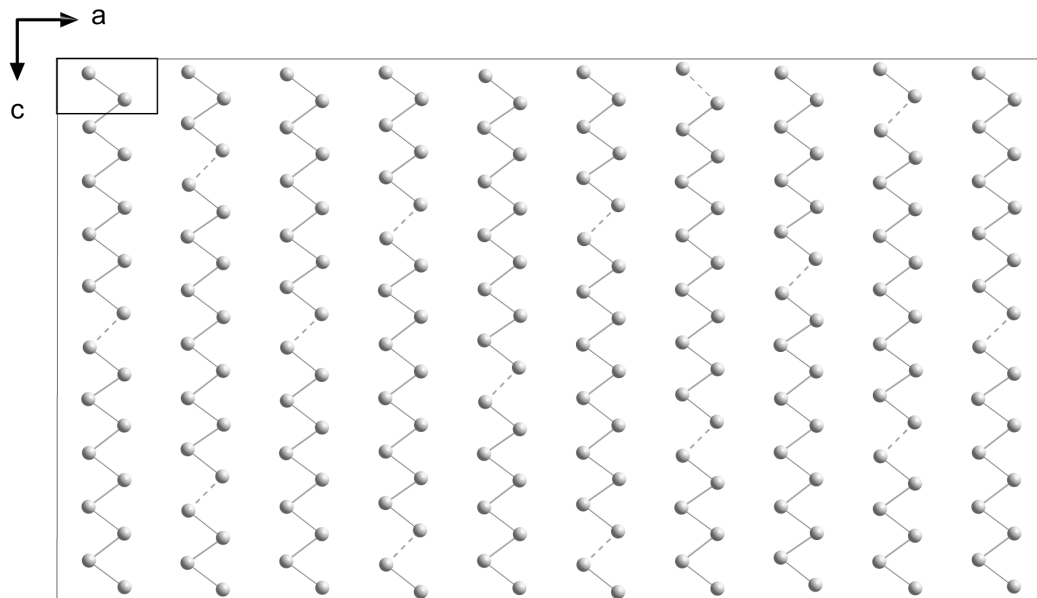


Figure S3. Section of the incommensurate WTe_2I structure showing only one layer of tungsten atoms with long bonds indicated as dashed lines. The unit cell is highlighted in the top left corner.

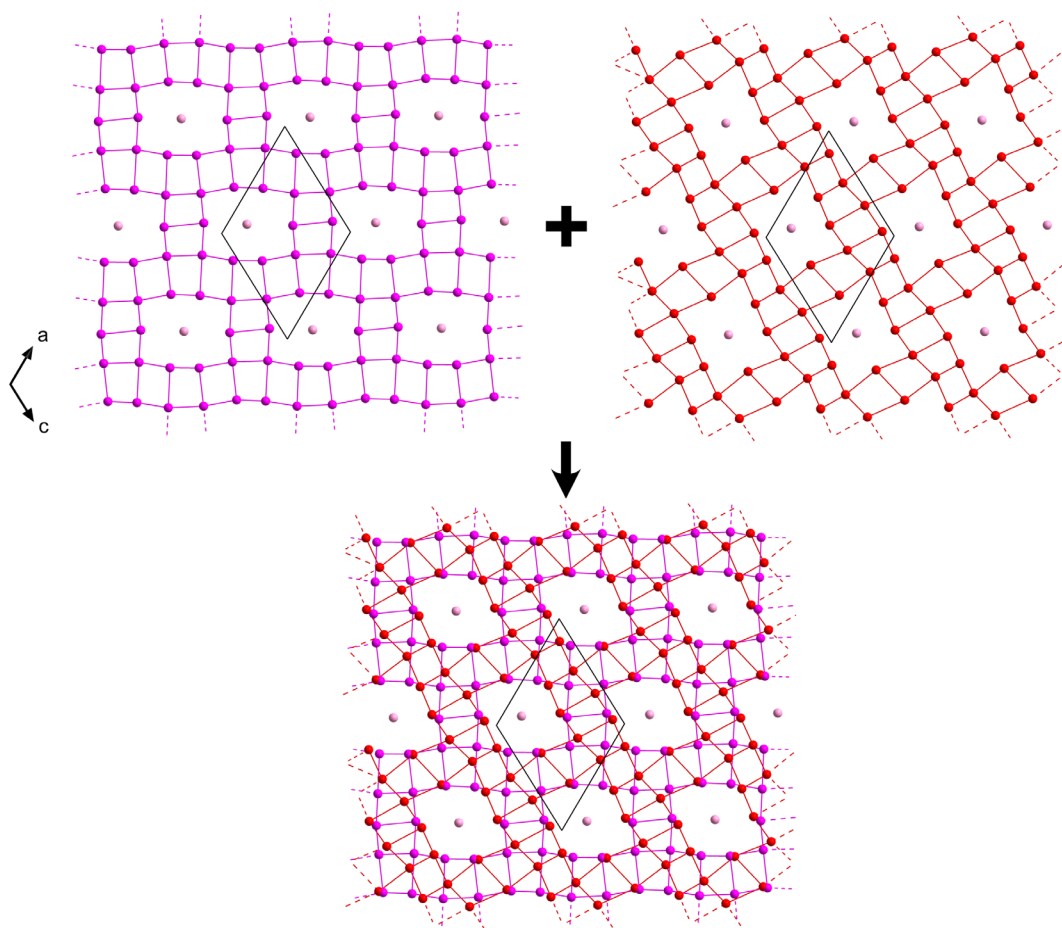


Figure S4. Sections of the WTe_2I supercell structure illustrating the iodine-layer disorder model. The top panels show the two disorder components separately (part a, purple; part b, red), while the bottom panel displays the combined iodine layer. Out-of-plane iodine atoms are highlighted in light purple. The structure is viewed along the b -axis, with the unit cell outlined.

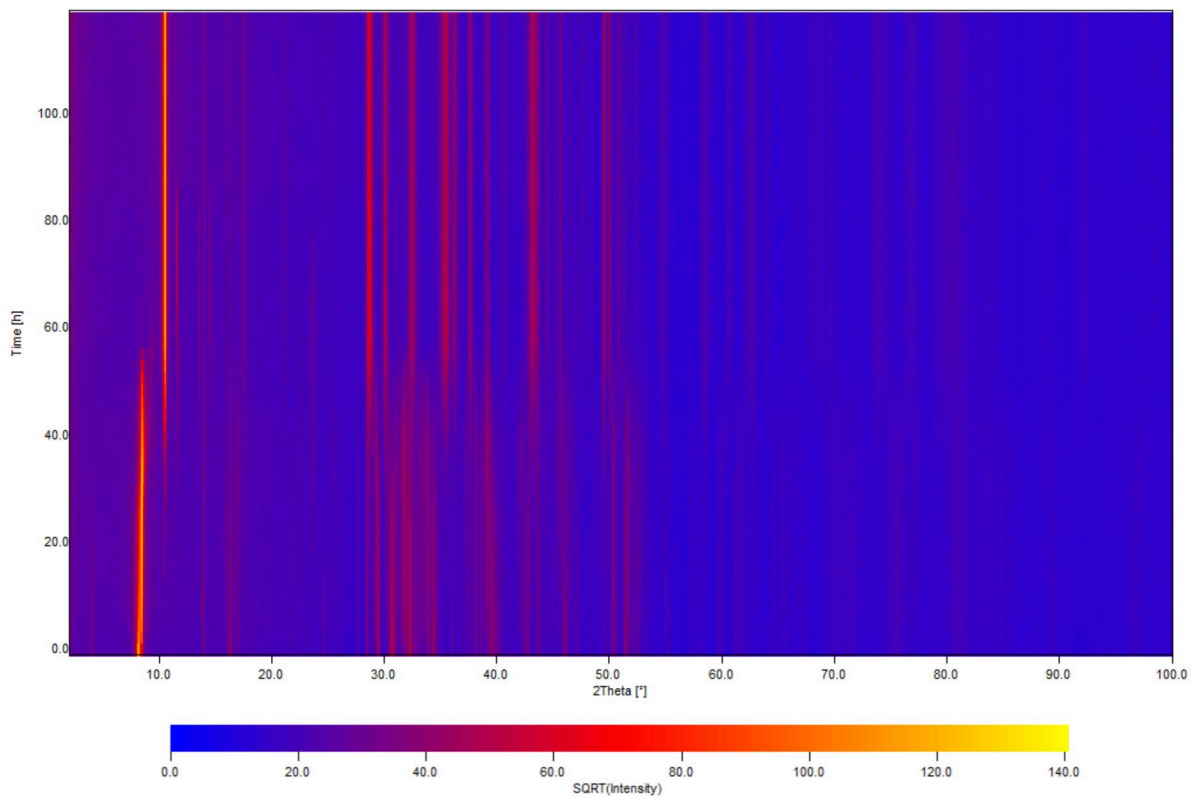


Figure S5. Time resolved PXRD analysis of WTe_2Br_x showing structural evolution while bromine deintercalation.

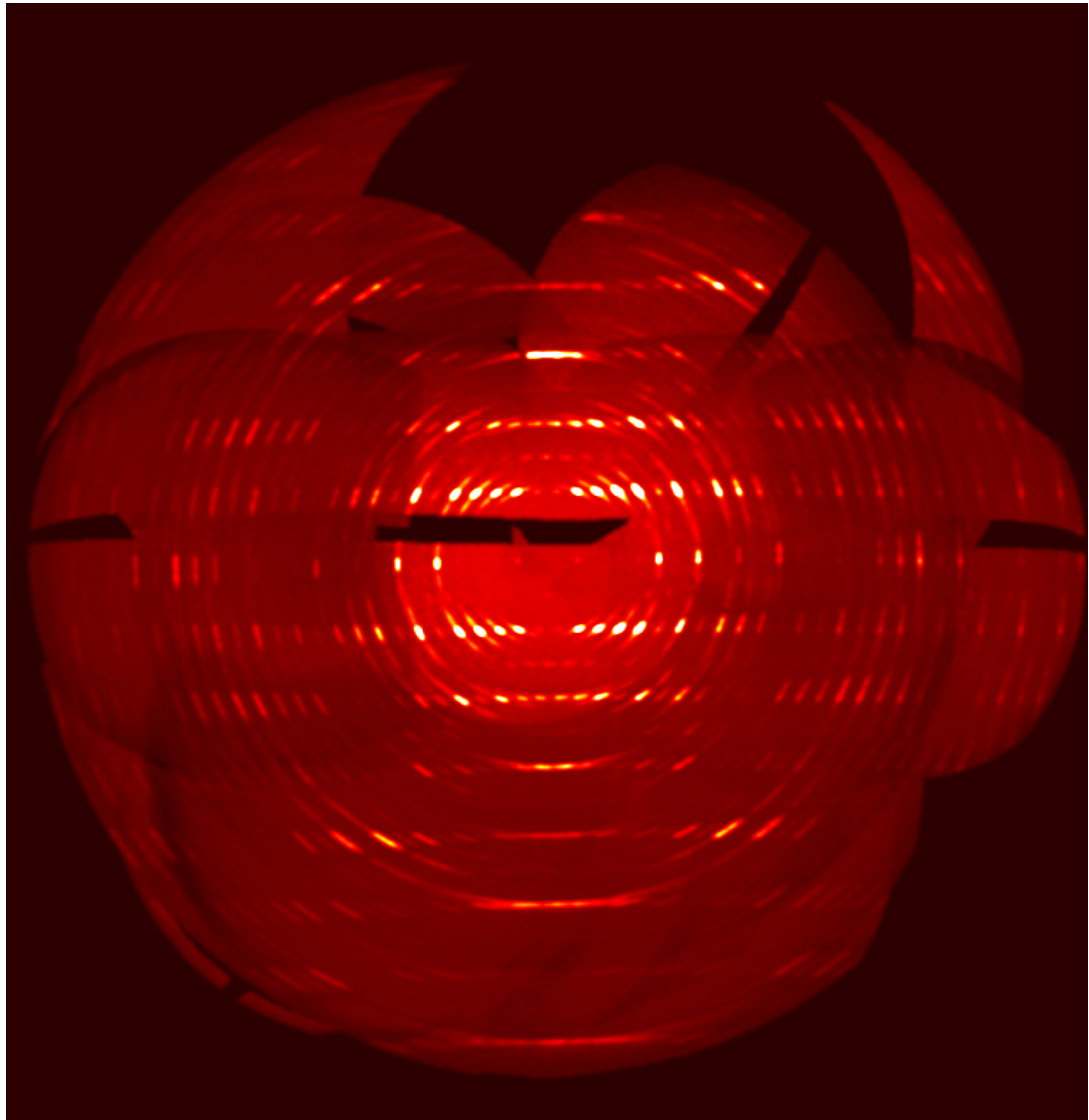


Figure S6. Reconstruction of the $(-3kn)$ of the reciprocal-space plane of $\text{WTe}_2\text{Br}_{1.25}$, highlighting reduced crystallinity due to multiple phase transitions.

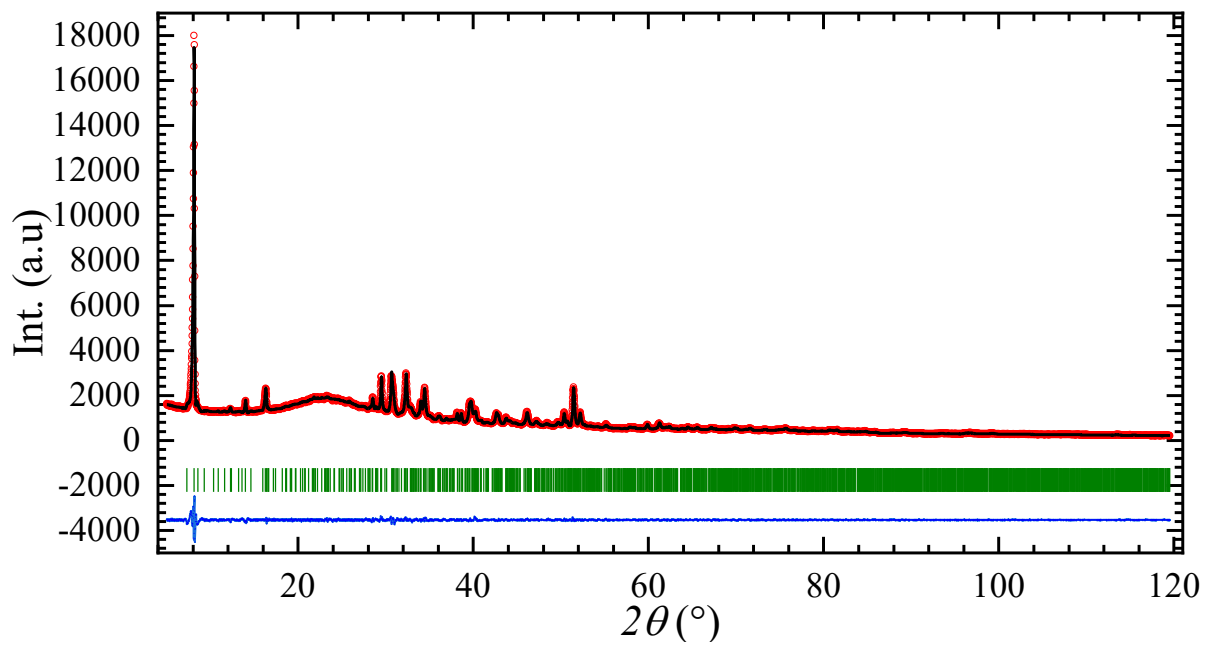


Figure S7. Rietveld refinement of $\text{WTe}_2\text{Br}_{1.25}$ using SXRD results for lattice and position parameters. The refinement shows a good agreement of PXRD and SXRD results.

Specialized Transmission Sample Holder

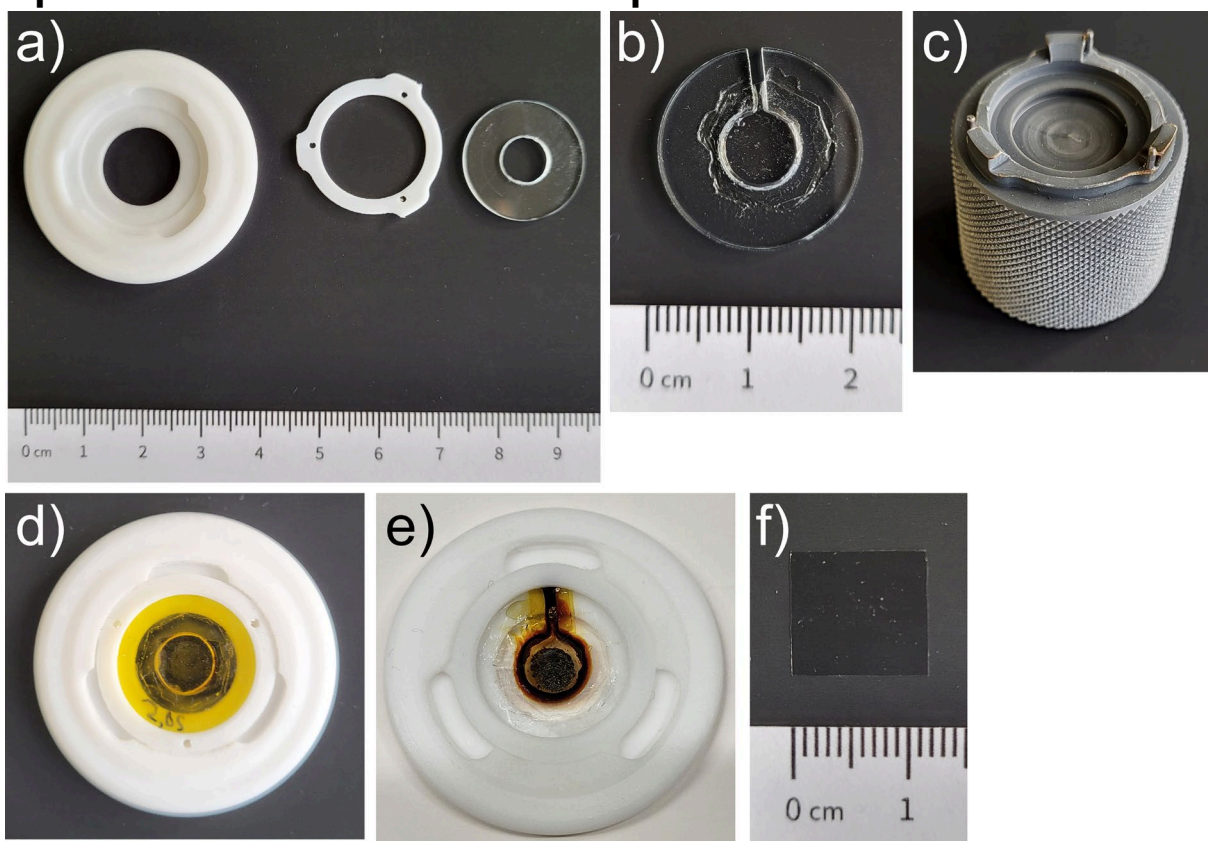
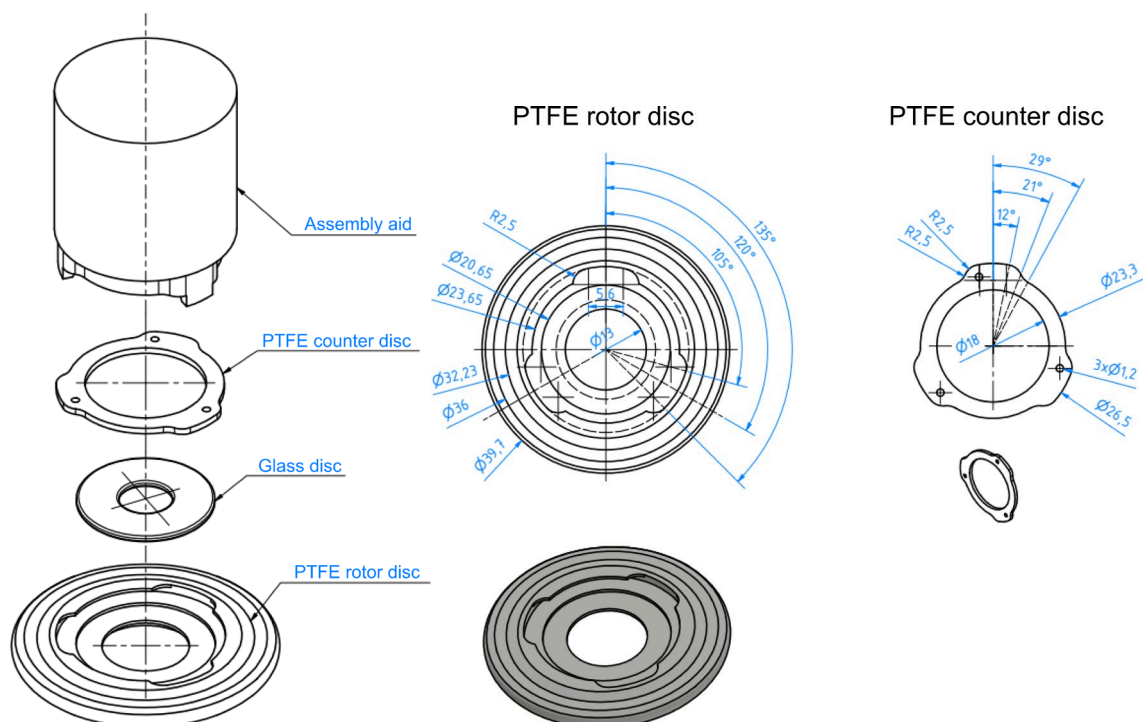
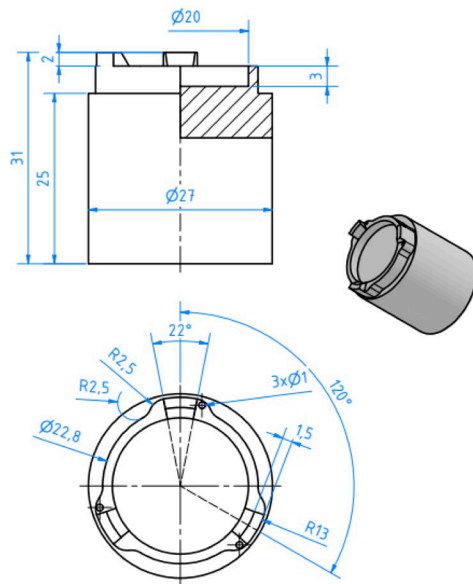


Figure S8. Components and assembly of the redesigned transmission sample holder. (a) PTFE rotor disc, PTFE counter disc, and glass disc. (b) Glass disc with an insertion slit and an ultrathin-glass window bonded to one side. (c) Assembly aid. (d) Transmission holder equipped with an assembled rotor disc (ultrathin glass on one side and Kapton on the other). (e) Examples of assembled rotor discs prepared for bromine-containing samples; for experiments with excess bromine, both sides were sealed with ultrathin glass and the perimeter was sealed with wax and cyanoacrylate under argon. (f) Ultrathin-glass window (Schott AF 32®).

Exploded view drawing



Assembly aid



Glas disc

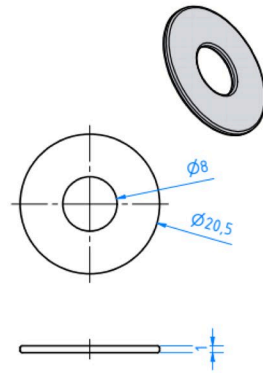


Figure S9. Engineering drawing of the redesigned transmission holder components (PTFE rotor disc, PTFE counter disc, glass disc, and assembly aid), including an exploded view and key dimensions (mm).

Crystallographic details for WTe₂ (supercell)

Table S1: Fractional Atomic Coordinates ($\times 10^4$) and Equivalent Isotropic Displacement Parameters ($\text{\AA}^2 \times 10^3$) for **WTe₂ (supercell)**. U_{eq} is defined as 1/3 of the trace of the orthogonalised U_j .

Atom	x	y	z	U_{eq}
W1	10340.8(7)	10074.9(3)	11376.4(7)	7.57(13)
W2	12243.8(8)	10053.4(4)	9537.5(8)	8.11(14)
W3	18784.5(7)	10050.7(4)	13031.9(8)	7.03(13)
W4	16172.5(7)	9956.1(4)	12038.8(8)	7.31(13)
W5	17157.2(7)	10038.2(4)	14661.4(8)	7.08(13)
W6	14525.4(6)	9978.7(3)	13694.4(6)	6.94(11)
Te1	9174.9(11)	9090.6(5)	10028.2(11)	8.51(18)
Te2	12484.8(13)	10971.8(6)	8234.0(12)	9.0(2)
Te3	15801.4(13)	9057.9(6)	13340.0(12)	8.5(2)
Te4	14134.7(11)	9056.6(5)	14952.2(11)	7.95(18)
Te5	17459.0(13)	10958.6(6)	13354.1(12)	8.2(2)
Te6	9010.4(12)	10972.9(6)	11644.3(12)	7.4(2)
Te7	10862.9(11)	9332.5(6)	13394.7(12)	7.9(2)
Te8	20758.1(12)	10691.9(6)	14936.8(12)	7.6(2)
Te9	17602.7(11)	9298.0(5)	16706.1(11)	7.33(18)
Te10	14124.3(12)	10697.7(6)	11583.2(12)	8.0(2)
Te11	14260.3(12)	9310.0(6)	10046.9(12)	7.9(2)
Te12	12502.9(11)	9513.6(5)	11682.9(11)	8.48(17)
I1	12390.5(13)	8251.2(5)	11550.8(13)	17.6(2)
I2A	17522(5)	7500	13841(6)	52.0(13)
I3A	15352(3)	7500	11151(4)	31.9(8)
I4A	13166(6)	7500	8826(6)	36.5(11)
I5A	10319(5)	7500	6530(4)	40.1(10)
I6A	15867(6)	7500	15192(6)	58.0(14)
I7A	9118(7)	7500	8110(8)	73.7(18)
I8A	14665(5)	7500	16743(4)	39.4(10)
I9A	11810(6)	7500	14423(6)	40.6(12)
I10A	9570(4)	7500	12122(4)	34.9(8)
I11A	7449(5)	7500	9458(6)	56.5(14)
I2B	13600(20)	12500	10224(16)	58(5)
I4B	14321(17)	12500	13021(15)	44(4)
I3B	11067(17)	12500	8914(17)	44(4)
I5B	10720(20)	12500	11142(12)	50(5)
I6B	14478(12)	12500	15563(13)	29(3)
I7B	10810(20)	12500	13717(12)	50(5)
I8B	14046(17)	12500	17773(14)	38(3)
I9B	11430(20)	12500	16481(16)	51(4)
I10B	12130(30)	7500	14788(16)	50(8)
I11B	12890(30)	7500	8436(15)	43(7)

Table S2: Anisotropic Displacement Parameters ($\times 10^4$) for **WTe₂** (supercell). The anisotropic displacement factor exponent takes the form: $-2\pi^2 [h^2 a^{*2} \times U_{11} + \dots + 2hka^* \times b^* \times U_{12}]$

Atom	U_{11}	U_{22}	U_{33}	U_{23}	U_{13}	U_{12}
W1	5.7(3)	10.2(3)	6.0(3)	-0.1(2)	2.0(2)	-0.5(2)
W2	6.4(3)	10.8(3)	6.0(4)	0.4(3)	1.9(3)	-1.0(3)
W3	4.9(3)	10.9(3)	5.3(3)	0.4(3)	2.3(2)	-1.1(3)
W4	5.1(3)	11.3(3)	5.7(4)	0.5(3)	2.7(2)	-1.2(3)
W5	4.8(3)	11.1(3)	5.3(4)	0.8(3)	2.3(2)	-1.3(3)
W6	4.7(4)	10.6(3)	5.4(4)	0.9(2)	2.3(2)	-1.4(2)
Te1	9.9(6)	11.5(4)	3.9(5)	1.0(4)	3.1(3)	-2.5(4)
Te2	10.5(6)	11.3(6)	6.0(6)	0.5(4)	4.5(5)	-1.7(4)
Te3	11.2(6)	11.0(5)	3.9(5)	1.0(4)	4.0(4)	-1.8(4)
Te4	11.0(6)	10.6(4)	3.3(5)	1.0(4)	4.3(3)	-1.7(4)
Te5	10.5(6)	10.9(5)	4.1(5)	1.0(4)	4.1(5)	-1.6(4)
Te6	8.7(5)	10.2(5)	5.0(5)	0.4(4)	4.6(4)	-1.0(4)
Te7	3.5(5)	13.3(5)	6.6(5)	0.2(4)	2.2(4)	-1.9(4)
Te8	3.2(5)	12.1(5)	7.8(6)	0.5(4)	2.8(4)	-1.7(4)
Te9	3.4(5)	11.4(4)	7.4(5)	0.9(4)	2.7(3)	-1.3(4)
Te10	3.7(5)	11.8(5)	8.4(6)	0.9(4)	2.8(4)	-1.4(4)
Te11	3.5(5)	12.6(5)	8.1(6)	1.3(5)	3.0(4)	-0.7(4)
Te12	4.2(5)	14.5(4)	7.7(5)	0.0(4)	3.6(3)	-1.5(4)
I1	20.0(6)	12.4(5)	20.0(7)	-1.0(5)	9.0(4)	-0.2(4)
I2A	62(3)	26.7(18)	92(4)	0	57(3)	0
I3A	39.1(19)	16.2(13)	49(2)	0	27.0(17)	0
I4A	49(3)	21.2(17)	44(3)	0	25(3)	0
I5A	63(3)	17.9(14)	49(2)	0	34(2)	0
I6A	91(4)	17.1(14)	79(4)	0	50(3)	0
I7A	100(5)	16.6(16)	110(6)	0	53(4)	0
I8A	65(3)	19.7(14)	49(2)	0	40(2)	0
I9A	53(3)	22.1(18)	52(4)	0	29(3)	0
I10A	46(2)	17.4(13)	54(2)	0	34.1(18)	0
I11A	64(3)	29.3(19)	99(4)	0	58(3)	0
I2B	91(15)	53(10)	29(8)	0	26(9)	0
I4B	55(10)	29(6)	34(7)	0	9(7)	0
I3B	56(10)	27(7)	51(10)	0	27(8)	0
I5B	97(13)	11(5)	10(5)	0	-2(7)	0
I6B	31(3)	25(3)	26(3)	0	10(2)	0
I7B	85(14)	37(7)	10(5)	0	6(6)	0
I8B	67(10)	18(5)	33(7)	0	27(7)	0
I9B	86(14)	43(8)	39(8)	0	42(9)	0
I10B	73(16)	26(8)	7(6)	0	-19(7)	0
I11B	70(15)	19(7)	5(7)	0	-13(7)	0

Table S3: Bond Lengths in Å for **WTe₂** (supercell).

Atom	Atom	Length / Å	Atom	Atom	Length / Å
W1	W1 ¹	3.0734(14)	W5	Te4 ²	2.7022(16)
W1	W2 ¹	2.8219(10)	W5	Te5	2.6953(15)
W1	Te1	2.6803(13)	W5	Te7 ²	2.8304(15)
W1	Te1 ¹	2.7458(15)	W5	Te8 ⁵	2.8419(15)
W1	Te6	2.6604(15)	W5	Te9	2.8035(14)
W1	Te7	2.7622(14)	W6	W6 ²	2.8355(14)
W1	Te9 ²	2.8591(13)	W6	Te3	2.6978(16)
W1	Te12	2.7676(14)	W6	Te4	2.7049(14)
W2	W3 ³	2.7874(10)	W6	Te4 ²	2.7085(13)
W2	Te1 ¹	2.7594(16)	W6	Te9 ²	2.8771(14)
W2	Te2	2.6596(15)	W6	Te10	2.8554(14)
W2	Te6 ¹	2.7211(16)	W6	Te12	2.7383(12)
W2	Te10	2.8528(16)	Te12	I1	2.7663(15)
W2	Te11	2.7641(15)	I2A	I3A	3.111(8)
W2	Te12	2.7478(15)	I2A	I6A	3.136(8)
W3	W4	2.8361(11)	I3A	I4A	2.846(7)
W3	Te2 ³	2.7492(16)	I5A	I7A	2.906(9)
W3	Te5	2.6997(16)	I6A	I8A	2.875(7)
W3	Te6 ⁴	2.7259(15)	I7A	I11A	3.148(10)
W3	Te7 ⁴	2.8329(15)	I9A	I10A	2.863(8)
W3	Te8 ⁵	2.7905(15)	I10A	I11A	3.068(8)
W3	Te8	2.8190(15)	I2B	I4B	3.10(2)
W4	W5	2.8479(10)	I2B	I3B	2.73(3)
W4	Te2 ³	2.7213(16)	I4B	I6B	3.01(2)
W4	Te3	2.6904(15)	I3B	I5B	2.93(3)
W4	Te5	2.7388(16)	I5B	I7B	3.09(2)
W4	Te10	2.8055(15)	I6B	I8B	2.97(2)
W4	Te11	2.8387(16)	I7B	I9B	3.09(2)
W4	Te11 ³	2.8393(15)	I8B	I9B	2.82(3)
W5	W6	2.8572(11)			
W5	Te3	2.7292(16)			

¹2-x,2-y,2-z; ²3-x,2-y,3-z; ³3-x,2-y,2-z; ⁴1+x,+y,+z; ⁵4-x,2-y,3-z

Table S4: Atomic Occupancies for all atoms that are not fully occupied in **WTe₂** (supercell).

Atom	Occupancy	Atom	Occupancy
I2A	0.803(4)	I2B	0.197(4)
I3A	0.803(4)	I4B	0.197(4)
I4A	0.803(4)	I3B	0.197(4)
I5A	0.803(4)	I5B	0.197(4)
I6A	0.803(4)	I6B	0.197(4)
I7A	0.803(4)	I7B	0.197(4)
I8A	0.803(4)	I8B	0.197(4)
I9A	0.803(4)	I9B	0.197(4)
I10A	0.803(4)	I10B	0.197(4)
I11A	0.803(4)	I11B	0.197(4)

Crystallographic details for incommensurate WTe₂I

Table S5: Occupational waves for incommensurate WTe₂I.

Atom	Wave/Parameter	Occ
Te2	delta	0.8318(8)
	x40	0.2710(4)
Te3	delta	0.1682(8)
	x40	0.7754(5)
I1	delta	0.8318(8)
	x40	0.3929(4)
I2	delta	0.8318(8)
	x40	0.1633(4)
I3	delta	0.1682(8)
	x40	0.7865(4)

Table S6: Positional parameters for incommensurate WTe₂I.

Atom	Occ	Wave	x	y	z	Ueq/Uiso
W1	1		0.32142(3)	0.495374(9)	0.25174(13)	0.00479(7)
		s,1	-0.00194(5)	0.001783(16)	-0.0072(12)	
		c,1	0.00190(5)	-0.001740(16)	-0.0085(10)	
		s,2	-0.00203(5)	-0.000332(16)	0.0046(2)	
		c,2	0.00211(5)	-0.000476(16)	0.0091(8)	
		s,3	-0.0010(3)	0.00067(8)	-0.0068(9)	
		c,3	0.0032(2)	-0.00036(7)	0.0057(11)	
		s,4	0	0	-0.067(2)	
		c,4	0.3826(5)	1	0	
		Te1	1		0.57919(5)	
s,1	-0.00264(8)			0.00038(3)	0.02596(15)	
c,1	-0.01089(8)			-0.00028(3)	-0.01238(15)	
s,2	0.00422(8)			-0.00187(3)	0.00920(15)	
c,2	0.00324(8)			-0.00144(3)	-0.00400(16)	
Te2	0.8318(8)		0.07022(7)	0.56927(2)	0.7492(2)	0.00552(9)
		o,1	-0.00111(10)	0.00106(3)	0.0018(2)	
		o,2	0.00011(6)	-0.00041(2)	-0.00017(12)	
		o,3	-0.00154(8)	0.00046(3)	-0.01128(14)	
Te3	0.1682(8)		0.0817(4)	0.54812(10)	0.7526(8)	0.0056(4)
		o,1	-0.0013(5)	-0.00001(17)	-0.0011(13)	
I1	0.8318(8)		0.34767(14)	0.75	0.7591(4)	0.0218(3)
		o,1	0.02889(15)	0	0.0932(3)	
		o,2	-0.01800(15)	0	-0.0089(4)	
		o,3	0.0001(2)	0	-0.0335(4)	
		o,4	0.00596(17)	0	-0.0221(4)	
		o,5	0.0008(3)	0	0.0010(5)	
		o,6	-0.0026(2)	0	-0.0113(5)	
I2	0.8318(8)		-0.17524(15)	0.75	0.7370(4)	0.0254(3)
		o,1	-0.03392(15)	0	-0.0879(3)	
		o,2	-0.00962(16)	0	0.0148(4)	
		o,3	-0.00434(19)	0	-0.0074(5)	
		o,4	-0.0032(2)	0	0.0410(5)	
		o,5	-0.0020(2)	0	-0.0104(6)	
I3	0.1682(8)		0.1052(2)	0.67498(7)	0.7481(5)	0.0151(3)
		o,1	-0.0031(8)	-0.0001(2)	0.0282(15)	

o,2 -0.004(4) 0.0007(12) -0.004(7)

Table S7: ADP harmonic parameters for incommensurate WTe₂l.

Atom	Wave	U11	U22	U33	U12	U13	U23
W1		0.00241(9)	0.00714(9)	0.00482(17)	-0.00014(6)	-0.00143(14)	0.00020(12)
	s,1	-0.00019(12)	0.00021(13)	-0.0004(2)	0.00008(11)	0.00026(12)	-0.00021(13)
	c,1	0.00005(12)	-0.00017(14)	0.00099(17)	-0.00011(11)	-0.00007(13)	-0.00023(13)
Te1		0.00502(12)	0.00856(13)	0.00596(13)	-0.00101(10)	-0.0012(2)	-0.0002(2)
	s,1	0.0010(2)	0.0013(2)	0.0005(2)	-0.00105(18)	-0.00049(16)	0.00068(17)
	c,1	0.0012(2)	0.0029(2)	0.0015(2)	-0.00243(17)	0.00108(17)	-0.00133(17)
Te2		0.00326(14)	0.00726(16)	0.00603(15)	0.00004(13)	-0.0015(3)	-0.0002(3)
	o,1	-0.00010(18)	-0.0005(2)	0.0018(2)	0.00021(17)	0.00013(15)	0.00003(19)
	o,2	-0.00001(16)	0.00011(18)	-0.00068(18)	0.00009(14)	-0.00018(13)	-0.00017(14)
Te3		0.0031(4)	0.0086(6)	0.0050(9)	-0.0011(5)	-0.0010(5)	0.0001(6)
I1		0.0176(4)	0.0156(3)	0.0323(6)	0	-0.0053(4)	0
	o,1	0.0024(4)	-0.0014(4)	0.0101(6)	0	-0.0048(4)	0
	o,2	0.0025(5)	-0.0015(4)	-0.0115(7)	0	0.0078(5)	0
I2		0.0183(4)	0.0158(3)	0.0419(7)	0	-0.0045(4)	0
	o,1	0.0024(4)	-0.0014(4)	0.0123(7)	0	-0.0090(4)	0
	o,2	-0.0010(5)	0.0016(4)	0.0149(6)	0	-0.0041(5)	0
I3		0.0174(6)	0.0089(5)	0.0191(7)	-0.0002(4)	-0.0017(5)	0.0005(5)

Table S9: List of distances for incommensurate WTe₂I.

	average / Å	min / Å	max / Å
W1-W1 ⁱ	2.870(11)	2.781(16)	3.097(16)
W1-W1 ⁱⁱ	2.846(11)	2.830(14)	2.862(14)
W1-Te1	2.720(3)	2.684(3)	2.755(3)
W1-Te1 ⁱ	2.706(8)	2.555(12)	2.856(12)
W1-Te1 ⁱⁱ	2.702(8)	2.543(12)	2.851(12)
W1-Te2 ⁱⁱⁱ	2.820(7)	2.749(9)	2.905(9)
W1-Te2	2.819(7)	2.739(9)	2.889(9)
W1-Te2 ^{iv}	2.845(3)	2.813(3)	2.877(3)
W1-Te3 ⁱⁱⁱ	2.76(4)	2.73(7)	2.78(7)
W1-Te3	2.73(4)	2.45(7)	2.78(7)
W1-Te3 ^{iv}	2.74(3)	2.73(6)	2.74(6)
Te3-I3	2.77(3)	2.76(6)	2.79(6)
I1-I1 ⁱⁱⁱ	3.415(6)	2.769(8)	4.018(8)
I1-I1 ^v	3.405(6)	2.769(8)	4.018(8)
I1-I2	3.341(6)	2.688(8)	3.933(8)
I1-I2 ^{vi}	3.189(6)	2.887(8)	3.702(8)
I1-I2 ^{vii}	3.341(6)	2.688(8)	3.933(8)
I1-I2 ^{viii}	3.189(6)	2.887(8)	3.702(8)
I1-I3 ⁱⁱⁱ	4.084(9)	4.011(15)	4.255(15)
I1-I3 ^v	4.297(9)	4.140(13)	4.407(13)
I1-I3 ^{ix}	4.084(9)	4.011(15)	4.255(15)
I1-I3 ^x	4.297(9)	4.140(13)	4.407(13)
I2-I2 ⁱⁱⁱ	3.419(7)	2.765(9)	4.028(9)
I2-I2 ^v	3.416(7)	2.765(9)	4.029(9)
I2-I2 ^{ix}	3.419(7)	2.765(9)	4.028(9)
I2-I2 ^{vii}	0	0	0
I2-I2 ^x	3.416(7)	2.765(9)	4.029(9)
I2-I3 ^v	4.123(8)	4.064(14)	4.250(14)
I2-I3 ^x	4.123(8)	4.064(14)	4.250(14)
I3-I3 ⁱⁱⁱ	3.659(15)	3.659(15)	3.659(15)
I3-I3 ^v	3.658(15)	3.658(15)	3.658(15)
I3-I3 ^{vii}	3.272(11)	3.24(2)	3.29(2)
(i)	-x+1,-y+1,-z		
(ii)	-x+1,-y+1,-z+1		
(iii)	x,y,z-1		
(iv)	-x,-y+1,-z+1		
(v)	x,y,z+1		
(vi)	x+1,y,z		
(vii)	x,-y+3/2,z		
(viii)	x+1,-y+3/2,z		
(ix)	x,-y+3/2,z-1		
(x)	x,-y+3/2,z+1		
(xi)	x-1,y,z		

Table S10: List of angles for incommensurate WTe₂l.

	average / °	min / °	max / °
W1 ⁱ -W1-W1 ⁱⁱ	74.7(3)	70.4(3)	83.2(3)
W1 ⁱ -W1-Te1	57.78(14)	55.55(17)	59.50(17)
W1 ⁱ -W1-Te1 ⁱ	58.3(2)	53.7(2)	60.5(3)
W1 ⁱ -W1-Te1 ⁱⁱ	104.93(15)	102.07(12)	110.76(16)
W1 ⁱ -W1-Te2 ⁱⁱⁱ	93.3(3)	90.1(4)	96.5(4)
W1 ⁱ -W1-Te2	140.27(13)	137.64(16)	143.27(12)
W1 ⁱ -W1-Te2 ^{iv}	136.1(4)	127.6(5)	142.3(5)
W1 ⁱ -W1-Te3 ⁱⁱⁱ	82.2(14)	81.4(14)	89.2(14)
W1 ⁱ -W1-Te3	145.6(13)	145.2(14)	146.3(13)
W1 ⁱ -W1-Te3 ^{iv}	139.1(15)	138.6(15)	140.2(15)
W1 ⁱⁱ -W1-Te1	58.04(14)	54.70(18)	61.91(19)
W1 ⁱⁱ -W1-Te1 ⁱ	104.74(15)	100.93(13)	110.0(2)
W1 ⁱⁱ -W1-Te1 ⁱⁱ	58.6(2)	56.8(3)	59.9(3)
W1 ⁱⁱ -W1-Te2 ⁱⁱⁱ	140.51(12)	137.11(13)	144.01(11)
W1 ⁱⁱ -W1-Te2	92.9(3)	90.2(4)	94.1(3)
W1 ⁱⁱ -W1-Te2 ^{iv}	137.0(4)	133.2(6)	141.6(5)
W1 ⁱⁱ -W1-Te3 ⁱⁱⁱ	145.8(12)	145.2(12)	146.6(13)
W1 ⁱⁱ -W1-Te3	87.4(14)	86.4(14)	93.9(16)
W1 ⁱⁱ -W1-Te3 ^{iv}	138.3(15)	138.0(15)	138.7(15)
Te1-W1-Te1 ⁱ	116.1(3)	109.3(4)	119.9(3)
Te1-W1-Te1 ⁱⁱ	116.6(3)	111.1(4)	121.3(3)
Te1-W1-Te2 ⁱⁱⁱ	83.74(15)	81.31(14)	86.70(13)
Te1-W1-Te2	83.82(14)	81.73(17)	86.06(14)
Te1-W1-Te2 ^{iv}	155.34(14)	152.2(3)	159.93(11)
Te1-W1-Te3 ⁱⁱⁱ	85.2(12)	83.5(12)	87.7(13)
Te1-W1-Te3	87.0(13)	85.8(13)	91.8(14)
Te1-W1-Te3 ^{iv}	151.2(13)	149.5(13)	152.0(13)
Te1 ⁱ -W1-Te1 ⁱⁱ	79.86(7)	77.14(7)	84.58(9)
Te1 ⁱ -W1-Te2 ⁱⁱⁱ	99.9(3)	95.4(4)	104.4(5)
Te1 ⁱ -W1-Te2	158.24(13)	156.7(3)	160.69(10)
Te1 ⁱ -W1-Te2 ^{iv}	81.23(16)	79.4(2)	84.66(17)
Te1 ⁱ -W1-Te3 ⁱⁱⁱ	85.8(14)	84.0(14)	88.1(14)
Te1 ⁱ -W1-Te3	153.9(13)	153.6(14)	154.3(12)
Te1 ⁱ -W1-Te3 ^{iv}	85.3(14)	84.7(14)	86.3(14)
Te1 ⁱⁱ -W1-Te2 ⁱⁱⁱ	158.39(13)	156.05(10)	159.76(11)
Te1 ⁱⁱ -W1-Te2	100.1(3)	96.8(4)	103.8(5)
Te1 ⁱⁱ -W1-Te2 ^{iv}	81.39(16)	78.55(14)	85.19(17)
Te1 ⁱⁱ -W1-Te3 ⁱⁱⁱ	154.5(12)	154.2(12)	154.9(12)
Te1 ⁱⁱ -W1-Te3	86.4(14)	84.5(14)	98.7(16)
Te1 ⁱⁱ -W1-Te3 ^{iv}	85.2(14)	84.6(14)	86.1(14)
Te2 ⁱⁱⁱ -W1-Te2	75.02(8)	72.66(7)	77.19(8)
Te2 ⁱⁱⁱ -W1-Te2 ^{iv}	78.53(13)	76.69(13)	80.30(15)
Te2 ⁱⁱⁱ -W1-Te3	80.7(14)	79.8(14)	81.2(13)
Te2 ⁱⁱⁱ -W1-Te3 ^{iv}	71.7(14)	71.4(14)	72.2(14)
Te2-W1-Te2 ^{iv}	78.43(13)	76.87(16)	79.87(15)
Te2-W1-Te3 ⁱⁱⁱ	79.0(14)	78.4(14)	80.0(14)
Te2-W1-Te3 ^{iv}	71.8(14)	71.1(14)	72.2(14)
Te2 ^{iv} -W1-Te3 ⁱⁱⁱ	71.1(12)	70.7(12)	72.2(12)
Te2 ^{iv} -W1-Te3	71.9(13)	70.7(12)	74.8(14)
Te3 ⁱⁱⁱ -W1-Te3	82.8(16)	82.8(16)	82.8(16)
W1-Te1-W1 ⁱ	63.9(2)	61.8(3)	69.3(3)
W1-Te1-W1 ⁱⁱ	63.3(2)	61.3(3)	65.4(3)
W1 ⁱ -Te1-W1 ⁱⁱ	79.8(3)	75.3(3)	89.7(3)
W1-Te2-W1 ^v	73.8(3)	71.3(3)	75.8(2)
W1-Te2-W1 ^{iv}	102.09(16)	99.7(2)	105.4(2)
W1 ^v -Te2-W1 ^{iv}	102.19(16)	99.1(2)	105.36(19)
W1-Te3-W1 ^v	89.9(10)	81.8(5)	90.6(17)

W1-Te3-W1 ^{iv}	110.9(11)	110.1(17)	114.4(5)
W1-Te3-I3	113.4(11)	112(2)	119.1(5)
W1 ^v -Te3-W1 ^{iv}	111.2(11)	110.1(7)	111.6(9)
W1 ^v -Te3-I3	114.2(11)	112.3(5)	115.4(7)
W1 ^{iv} -Te3-I3	114.7(10)	113.6(4)	115.3(19)
I1 ⁱⁱⁱ -I1-I1 ^v	176.1(2)	171.3(2)	180
I1 ⁱⁱⁱ -I1-I2	89.3(2)	76.22(19)	107.0(2)
I1 ⁱⁱⁱ -I1-I2 ^{vi}	89.7(2)	82.1(2)	97.28(17)
I1 ⁱⁱⁱ -I1-I2 ^{vii}	89.3(2)	76.22(19)	107.0(2)
I1 ⁱⁱⁱ -I1-I2 ^{viii}	89.7(2)	82.1(2)	97.28(17)
I1 ⁱⁱⁱ -I1-I3 ^v	154.94(10)	152.26(10)	156.47(8)
I1 ⁱⁱⁱ -I1-I3 ^x	154.94(10)	152.26(10)	156.47(8)
I1 ^v -I1-I2	91.0(2)	81.1(2)	100.33(17)
I1 ^v -I1-I2 ^{vi}	94.6(2)	77.28(18)	99.9(2)
I1 ^v -I1-I2 ^{vii}	91.0(2)	81.1(2)	100.33(17)
I1 ^v -I1-I2 ^{viii}	94.6(2)	77.28(18)	99.9(2)
I1 ^v -I1-I3 ⁱⁱⁱ	149.64(11)	148.82(13)	151.36(8)
I1 ^v -I1-I3 ^{ix}	149.64(11)	148.82(13)	151.36(8)
I2-I1-I2 ^{vi}	167.5(2)	155.8(2)	180
I2-I1-I2 ^{vii}	0	0	0
I2-I1-I2 ^{viii}	167.5(2)	155.8(2)	180
I2-I1-I3 ⁱⁱⁱ	75.05(15)	72.67(16)	76.11(14)
I2-I1-I3 ^v	66.88(13)	65.76(11)	69.54(16)
I2-I1-I3 ^{ix}	75.05(15)	72.67(16)	76.11(14)
I2-I1-I3 ^x	66.88(13)	65.76(11)	69.54(16)
I2 ^{vi} -I1-I2 ^{vii}	167.5(2)	155.8(2)	180
I2 ^{vi} -I1-I2 ^{viii}	0	0	0
I2 ^{vi} -I1-I3 ⁱⁱⁱ	102.09(16)	101.80(18)	102.33(15)
I2 ^{vi} -I1-I3 ^v	95.29(14)	91.83(14)	102.89(12)
I2 ^{vi} -I1-I3 ^{ix}	102.09(16)	101.80(18)	102.33(15)
I2 ^{vi} -I1-I3 ^x	95.29(14)	91.83(14)	102.89(12)
I2 ^{vii} -I1-I2 ^{viii}	167.5(2)	155.8(2)	180
I2 ^{vii} -I1-I3 ⁱⁱⁱ	75.05(15)	72.67(16)	76.11(14)
I2 ^{vii} -I1-I3 ^v	66.88(13)	65.76(11)	69.54(16)
I2 ^{vii} -I1-I3 ^{ix}	75.05(15)	72.67(16)	76.11(14)
I2 ^{vii} -I1-I3 ^x	66.88(13)	65.76(11)	69.54(16)
I2 ^{viii} -I1-I3 ⁱⁱⁱ	102.09(16)	101.80(18)	102.33(15)
I2 ^{viii} -I1-I3 ^v	95.29(14)	91.83(14)	102.89(12)
I2 ^{viii} -I1-I3 ^{ix}	102.09(16)	101.80(18)	102.33(15)
I2 ^{viii} -I1-I3 ^x	95.29(14)	91.83(14)	102.89(12)
I3 ⁱⁱⁱ -I1-I3 ^{ix}	47.28(14)	44.9(2)	48.29(11)
I3 ^v -I1-I3 ^x	44.80(13)	43.19(11)	46.3(2)
I1 ^{xi} -I2-I1	168.9(2)	157.3(3)	180
I1 ^{xi} -I2-I2 ⁱⁱⁱ	94.48(18)	77.86(17)	99.7(2)
I1 ^{xi} -I2-I2 ^v	89.74(19)	82.2(2)	97.1(2)
I1 ^{xi} -I2-I2 ^{ix}	94.48(18)	77.86(17)	99.7(2)
I1 ^{xi} -I2-I2 ^{vii}	0	0	0
I1 ^{xi} -I2-I2 ^x	89.74(19)	82.2(2)	97.1(2)
I1 ^{xi} -I2-I3 ^v	105.61(14)	104.61(18)	106.13(11)
I1 ^{xi} -I2-I3 ^x	105.61(14)	104.61(18)	106.13(11)
I1-I2-I2 ⁱⁱⁱ	90.67(18)	82.37(19)	99.6(2)
I1-I2-I2 ^v	88.91(19)	76.01(17)	105.7(2)
I1-I2-I2 ^{ix}	90.67(18)	82.37(19)	99.6(2)
I1-I2-I2 ^{vii}	0	0	0
I1-I2-I2 ^x	88.91(19)	76.01(17)	105.7(2)
I1-I2-I3 ^v	73.38(13)	71.73(14)	74.28(12)
I1-I2-I3 ^x	73.38(13)	71.73(14)	74.28(12)
I2 ⁱⁱⁱ -I2-I2 ^v	175.9(2)	171.3(3)	179.53(17)
I2 ⁱⁱⁱ -I2-I2 ^{ix}	0	0	0
I2 ⁱⁱⁱ -I2-I2 ^{vii}	0	0	0

I2 ⁱⁱⁱ -I2-I2 ^x	175.9(2)	171.3(3)	179.53(17)
I2 ⁱⁱⁱ -I2-I3 ^v	148.13(10)	147.38(11)	149.85(12)
I2 ⁱⁱⁱ -I2-I3 ^x	148.13(10)	147.38(11)	149.85(12)
I2 ^v -I2-I2 ^{ix}	175.9(2)	171.3(3)	179.53(16)
I2 ^v -I2-I2 ^{vii}	0	0	0
I2 ^v -I2-I2 ^x	0	0	0
I2 ^{ix} -I2-I2 ^{vii}	0	0	0
I2 ^{ix} -I2-I2 ^x	175.9(2)	171.3(3)	179.53(17)
I2 ^{ix} -I2-I3 ^v	148.13(10)	147.38(11)	149.85(12)
I2 ^{ix} -I2-I3 ^x	148.13(10)	147.38(11)	149.85(12)
I2 ^{vii} -I2-I2 ^x	0	0	0
I2 ^{vii} -I2-I3 ^v	0	0	0
I2 ^{vii} -I2-I3 ^x	0	0	0
I3 ^v -I2-I3 ^x	46.79(13)	44.87(12)	47.60(14)
Te3-I3-I1 ⁱⁱⁱ	113.7(8)	112.1(4)	114.3(14)
Te3-I3-I1 ^v	114.6(8)	113.1(7)	115.4(4)
Te3-I3-I2 ⁱⁱⁱ	112.4(8)	110.8(4)	113.0(13)
Te3-I3-I2 ^{ix}	112.4(8)	110.8(4)	113.0(13)
Te3-I3-I3 ⁱⁱⁱ	87.8(5)	87.8(5)	87.8(5)
Te3-I3-I3 ^v	88.2(5)	88.2(5)	88.2(5)
Te3-I3-I3 ^{vii}	176.6(8)	176.4(12)	176.9(5)
I1 ⁱⁱⁱ -I3-I1 ^v	119.6(2)	118.4(3)	120.96(17)
I1 ⁱⁱⁱ -I3-I2 ⁱⁱⁱ	39.78(14)	38.23(17)	42.02(13)
I1 ⁱⁱⁱ -I3-I2 ^{ix}	39.78(14)	38.23(17)	42.02(13)
I1 ⁱⁱⁱ -I3-I3 ^v	152.4(2)	152.4(2)	152.4(2)
I1 ⁱⁱⁱ -I3-I3 ^{vii}	67.62(17)	66.9(2)	68.42(15)
I1 ^v -I3-I2 ⁱⁱⁱ	132.7(2)	132.17(16)	133.8(3)
I1 ^v -I3-I2 ^{ix}	132.7(2)	132.17(16)	133.8(3)
I1 ^v -I3-I3 ⁱⁱⁱ	146.8(4)	146.8(4)	146.8(4)
I1 ^v -I3-I3 ^{vii}	66.38(17)	65.86(13)	67.6(3)
I2 ⁱⁱⁱ -I3-I2 ^{ix}	0	0	0
I2 ⁱⁱⁱ -I3-I3 ^v	144.9(2)	144.9(2)	144.9(2)
I2 ⁱⁱⁱ -I3-I3 ^{vii}	66.62(16)	66.20(18)	67.60(15)
I2 ^{ix} -I3-I3 ^v	144.9(2)	144.9(2)	144.9(2)
I2 ^{ix} -I3-I3 ^{vii}	66.62(16)	66.20(18)	67.60(15)
I3 ⁱⁱⁱ -I3-I3 ^{vii}	89.9(4)	89.9(4)	89.9(4)
I3 ^v -I3-I3 ^{vii}	90.0(3)	90.0(3)	90.0(3)
(i)	-x+1,-y+1,-z		
(ii)	-x+1,-y+1,-z+1		
(iii)	x,y,z-1		
(iv)	-x,-y+1,-z+1		
(v)	x,y,z+1		
(vi)	x+1,y,z		
(vii)	x,-y+3/2,z		
(viii)	x+1,-y+3/2,z		
(ix)	x,-y+3/2,z-1		
(x)	x,-y+3/2,z+1		
(xi)	x-1,y,z		

Crystallographic details for commensurate WTe₂

Table S 11: Occupational waves for commensurate WTe₂.

Atom	Wave/Parameter	Occ
Te2	delta	0.8318
	x40	0.3211(4)
Te3	delta	0.1682
	x40	0.8231(4)
I1	delta	0.8318
	x40	0.4567(5)
I2	delta	0.8318
	x40	0.1933
I3	delta	0.1682
	x40	0.8366(5)

Table S12: Positional parameters for commensurate WTe₂.

Atom	Occ	Wave	x	y	z	Ueq/Uiso
W1	1		0.32164(6)	0.495299(18)	0.2518(2)	0.00718(10)
		s,1	-0.00066(16)	0.00147(4)	-0.0298(10)	
		c,1	0.00256(13)	-0.00162(3)	-0.0094(4)	
		s,2	-0.00350(11)	0.00013(3)	-0.0044(6)	
		c,2	-0.00019(14)	0.00012(4)	0.0026(4)	
		s,3	0	0	-0.0949(15)	
Te1	1		0.57916(10)	0.59501(3)	0.2561(3)	0.00847(15)
		s,1	-0.0039(3)	0.00054(8)	0.0279(3)	
		c,1	-0.00876(16)	-0.00040(5)	-0.0007(5)	
		s,2	-0.0009(2)	-0.00033(5)	0.0108(3)	
		c,2	0.00613(17)	-0.00235(5)	-0.0041(3)	
			0.4355	1	0	
Te2	0.8318		0.07018(16)	0.56910(4)	0.7592(4)	0.00718(18)
		o,1	-0.0008(2)	0.00093(6)	-0.0008(6)	
		o,2	0.0002(3)	0.00012(7)	0.0029(4)	
		o,3	0.0011(4)	-0.00061(11)	-0.0175(8)	
		o,4	-0.0007(3)	0.00003(8)	-0.0030(7)	
Te3	0.1682		0.0811(4)	0.54884(10)	0.7465(8)	0.0077(4)
I1	0.8318		0.3527(6)	0.75	0.7423(14)	0.0627(11)
		o,1	0.0010(9)	0	0.0720(8)	
		o,2	-0.0266(7)	0	0.0347(12)	
		o,3	-0.0065(7)	0	-0.0358(10)	
		o,4	0.0058(11)	0	-0.0214(14)	
I2	0.8318		-0.1823(6)	0.75	0.7503(15)	0.0660(12)
		o,1	-0.0280(8)	0	0.0009(12)	
		o,2	-0.0161(8)	0	0.0755(9)	
		o,3	-0.0021(8)	0	0.0387(11)	
		o,4	0.0110(11)	0	0.0226(18)	
I3	0.1682		0.1055(4)	0.67488(9)	0.7537(9)	0.0168(5)

Table S13: ADP harmonic parameters for commensurate WTe₂l.

Atom	Wave	U11	U22	U33	U12	U13	U23
W1		0.00523(16)	0.01106(18)	0.00526(17)	-0.00038(13)	0.0000(4)	0.0020(2)
	s,1	0.0003(4)	0.0005(4)	-0.0008(3)	0.0009(3)	-0.0001(3)	0.0002(2)
	c,1	0.0002(3)	0.0000(3)	0.0004(3)	0.0002(3)	-0.0004(3)	0.0005(3)
Te1		0.0080(3)	0.0118(3)	0.0056(3)	-0.0009(2)	-0.0037(5)	0.0036(4)
Te2		0.0053(3)	0.0125(3)	0.0037(4)	-0.0006(2)	0.0026(5)	0.0027(4)
	o,1	0.0004(3)	-0.0016(4)	-0.0009(4)	0.0005(3)	0.0006(4)	-0.0009(4)
	o,2	0.0007(5)	-0.0007(5)	0.0002(5)	0.0006(4)	0.0001(2)	-0.0001(3)
Te3		0.0058(8)	0.0144(9)	0.0028(7)	0.0000(8)	0.0027(9)	-0.0003(11)
I1		0.102(2)	0.0259(9)	0.060(2)	0	0.018(2)	0
	o,1	0.005(3)	-0.0021(13)	0.0039(18)	0	-0.0057(15)	0
	o,2	-0.018(3)	0.0008(11)	-0.0075(17)	0	0.001(2)	0
I2		0.106(3)	0.0257(9)	0.067(2)	0	0.009(2)	0
	o,1	0.031(3)	-0.0012(12)	0.018(2)	0	-0.002(2)	0
	o,2	0.008(2)	0.0039(12)	0.0100(18)	0	0.0008(16)	0
I3		0.0182(9)	0.0128(8)	0.0194(9)	-0.0005(7)	-0.0014(11)	-0.0004(10)

Table S15: List of distances for commensurate WTe₂l.

	average / Å	min / Å	max / Å
W1-W1 ⁱ	2.843(6)	2.825(7)	2.862(7)
W1-W1 ⁱⁱ	2.859(6)	2.775(9)	3.080(9)
W1-Te1	2.722(3)	2.689(3)	2.746(3)
W1-Te1 ⁱ	2.715(5)	2.649(6)	2.794(6)
W1-Te1 ⁱⁱ	2.696(5)	2.623(7)	2.761(7)
W1-Te2 ⁱⁱⁱ	2.802(6)	2.744(8)	2.863(8)
W1-Te2	2.837(5)	2.787(7)	2.905(7)
W1-Te2 ^{iv}	2.839(4)	2.814(6)	2.860(6)
W1-Te3 ⁱⁱⁱ	2.755(5)	2.755(5)	2.755(5)
W1-Te3	2.766(7)	2.766(7)	2.766(7)
W1-Te3 ^{iv}	2.739(3)	2.739(3)	2.739(3)
Te3-I3	2.762(3)	2.762(3)	2.762(3)
I1-I1 ⁱⁱⁱ	3.416(11)	2.900(12)	3.915(12)
I1-I1 ^v	3.416(11)	2.900(12)	3.915(12)
I1-I2	3.374(14)	2.966(18)	4.015(18)
I1-I2 ^{vi}	3.143(14)	3.051(17)	3.223(17)
I1-I3 ^v	4.164(8)	4.164(8)	4.164(8)
I1-I3 ^{vii}	4.164(8)	4.164(8)	4.164(8)
I2-I2 ⁱⁱⁱ	3.443(13)	2.967(16)	4.002(16)
I2-I2 ^v	3.443(13)	2.967(16)	4.002(16)
I2-I3 ⁱⁱⁱ	4.148(11)	4.148(11)	4.148(11)
I2-I3 ^{viii}	4.148(11)	4.148(11)	4.148(11)
I3-I3 ^{ix}	3.287(3)	3.287(3)	3.287(3)
(i)	-x+1,-y+1,-z		
(ii)	-x+1,-y+1,-z+1		
(iii)	x,y,z-1		
(iv)	-x,-y+1,-z+1		
(v)	x,y,z+1		
(vi)	x+1,y,z		
(vii)	x,-y+3/2,z+1		
(viii)	x,-y+3/2,z-1		
(ix)	x,-y+3/2,z		
(x)	x-1,y,z		

Table S16: List of angles for commensurate WTe₂l.

	average / °	min / °	max / °
W1 ⁱ -W1-W1 ⁱⁱ	74.97(16)	71.72(19)	82.50(17)
W1 ⁱ -W1-Te1	58.38(10)	57.09(11)	60.83(11)
W1 ⁱ -W1-Te1 ⁱ	58.59(12)	57.18(14)	59.34(15)
W1 ⁱ -W1-Te1 ⁱⁱ	104.87(11)	102.29(11)	109.22(11)
W1 ⁱ -W1-Te2 ⁱⁱⁱ	93.0(2)	91.9(2)	93.50(19)
W1 ⁱ -W1-Te2	140.47(16)	137.74(16)	142.44(15)
W1 ⁱ -W1-Te2 ^{iv}	136.3(3)	133.8(3)	139.1(3)
W1 ⁱ -W1-Te3 ⁱⁱⁱ	87.1(2)	87.1(2)	87.1(2)
W1 ⁱ -W1-Te3	145.68(10)	145.68(10)	145.68(10)
W1 ⁱ -W1-Te3 ^{iv}	138.87(18)	138.87(18)	138.87(18)
W1 ⁱⁱ -W1-Te1	57.67(10)	56.70(12)	58.57(10)
W1 ⁱⁱ -W1-Te1 ⁱ	105.25(11)	102.55(10)	109.73(11)
W1 ⁱⁱ -W1-Te1 ⁱⁱ	58.63(12)	54.50(15)	61.06(13)
W1 ⁱⁱ -W1-Te2 ⁱⁱⁱ	140.04(16)	138.02(16)	142.81(15)
W1 ⁱⁱ -W1-Te2	92.9(2)	91.6(2)	94.6(2)
W1 ⁱⁱ -W1-Te2 ^{iv}	136.6(3)	129.4(3)	141.9(3)
W1 ⁱⁱ -W1-Te3 ⁱⁱⁱ	145.00(12)	145.00(12)	145.00(12)
W1 ⁱⁱ -W1-Te3	82.1(2)	82.1(2)	82.1(2)

W1 ⁱⁱ -W1-Te3 ^{iv}	138.71(19)	138.71(19)	138.71(19)
Te1-W1-Te1 ⁱ	116.87(16)	114.04(17)	119.9(2)
Te1-W1-Te1 ⁱⁱ	116.29(17)	111.2(2)	119.63(17)
Te1-W1-Te2 ⁱⁱⁱ	83.75(17)	81.88(17)	85.62(16)
Te1-W1-Te2	83.27(17)	81.75(17)	85.50(16)
Te1-W1-Te2 ^{iv}	155.39(17)	153.53(17)	157.29(16)
Te1-W1-Te3 ⁱⁱⁱ	86.47(12)	86.47(12)	86.47(12)
Te1-W1-Te3	85.13(15)	85.13(15)	85.13(15)
Te1-W1-Te3 ^{iv}	150.85(9)	150.85(9)	150.85(9)
Te1 ⁱ -W1-Te1 ⁱⁱ	79.83(9)	77.81(9)	83.73(9)
Te1 ⁱ -W1-Te2 ⁱⁱⁱ	100.4(2)	97.8(2)	103.4(3)
Te1 ⁱ -W1-Te2	158.47(17)	157.59(17)	159.61(17)
Te1 ⁱ -W1-Te2 ^{iv}	80.83(18)	78.93(18)	83.49(19)
Te1 ⁱ -W1-Te3 ⁱⁱⁱ	85.48(18)	85.48(18)	85.48(18)
Te1 ⁱ -W1-Te3	154.93(12)	154.93(12)	154.93(12)
Te1 ⁱ -W1-Te3 ^{iv}	85.84(11)	85.84(11)	85.84(11)
Te1 ⁱⁱ -W1-Te2 ⁱⁱⁱ	158.18(18)	156.56(16)	160.50(18)
Te1 ⁱⁱ -W1-Te2	99.9(2)	96.6(2)	103.3(3)
Te1 ⁱⁱ -W1-Te2 ^{iv}	81.40(18)	80.4(2)	83.30(18)
Te1 ⁱⁱ -W1-Te3 ⁱⁱⁱ	153.84(12)	153.84(12)	153.84(12)
Te1 ⁱⁱ -W1-Te3	85.9(2)	85.9(2)	85.9(2)
Te1 ⁱⁱ -W1-Te3 ^{iv}	84.74(10)	84.74(10)	84.74(10)
Te2 ⁱⁱⁱ -W1-Te2	75.03(19)	73.37(17)	77.4(2)
Te2 ⁱⁱⁱ -W1-Te2 ^{iv}	78.28(18)	77.24(17)	79.01(17)
Te2 ⁱⁱⁱ -W1-Te3	78.46(15)	78.46(15)	78.46(15)
Te2 ⁱⁱⁱ -W1-Te3 ^{iv}	71.84(13)	71.84(13)	71.84(13)
Te2-W1-Te2 ^{iv}	78.91(18)	77.6(2)	80.1(2)
Te2-W1-Te3 ⁱⁱⁱ	80.69(8)	80.69(8)	80.69(8)
Te2-W1-Te3 ^{iv}	71.95(13)	71.95(13)	71.95(13)
Te2 ^{iv} -W1-Te3 ⁱⁱⁱ	71.85(15)	71.85(15)	71.85(15)
Te2 ^{iv} -W1-Te3	72.28(16)	72.28(16)	72.28(16)
W1-Te1-W1 ⁱ	63.04(13)	62.00(16)	64.18(11)
W1-Te1-W1 ⁱⁱ	63.70(13)	61.85(13)	68.81(17)
W1 ⁱ -Te1-W1 ⁱⁱ	79.82(17)	76.3(2)	89.14(18)
W1-Te2-W1 ^v	73.77(18)	71.83(16)	75.17(19)
W1-Te2-W1 ^{iv}	101.63(16)	99.85(10)	103.8(2)
W1 ^v -Te2-W1 ^{iv}	102.28(16)	100.6(2)	104.6(2)
W1-Te3-W1 ^v	89.8(2)	89.8(2)	89.8(2)
W1-Te3-W1 ^{iv}	111.06(14)	111.06(14)	111.06(14)
W1-Te3-I3	114.59(12)	114.59(12)	114.59(12)
W1 ^v -Te3-W1 ^{iv}	110.62(14)	110.62(14)	110.62(14)
W1 ^v -Te3-I3	113.31(12)	113.31(12)	113.31(12)
W1 ^{iv} -Te3-I3	114.85(10)	114.85(10)	114.85(10)
I1 ⁱⁱⁱ -I1-I1 ^v	176.2(4)	170.9(4)	179.9(5)
I1 ⁱⁱⁱ -I1-I2	90.7(4)	87.0(4)	96.3(4)
I1 ⁱⁱⁱ -I1-I2 ^{vi}	92.1(4)	83.7(4)	98.3(4)
I1 ⁱⁱⁱ -I1-I3 ^v	149.9(2)	149.9(2)	149.9(2)
I1 ⁱⁱⁱ -I1-I3 ^{vii}	149.9(2)	149.9(2)	149.9(2)
I1 ^v -I1-I2	89.7(4)	81.3(3)	98.6(4)
I1 ^v -I1-I2 ^{vi}	91.9(4)	83.5(4)	96.2(4)
I2-I1-I2 ^{vi}	169.3(4)	165.3(5)	171.8(4)
I2-I1-I3 ^v	72.03(19)	72.03(19)	72.03(19)
I2-I1-I3 ^{vii}	72.03(19)	72.03(19)	72.03(19)
I2 ^{vi} -I1-I3 ^v	100.5(2)	100.5(2)	100.5(2)
I2 ^{vi} -I1-I3 ^{vii}	100.5(2)	100.5(2)	100.5(2)
I3 ^v -I1-I3 ^{vii}	46.49(9)	46.49(9)	46.49(9)
I1 ^x -I2-I1	170.3(4)	166.8(3)	175.2(5)
I1 ^x -I2-I2 ⁱⁱⁱ	91.0(4)	82.6(3)	95.9(3)
I1 ^x -I2-I2 ^v	91.7(4)	84.3(4)	95.7(4)
I1 ^x -I2-I3 ⁱⁱⁱ	105.3(3)	105.3(3)	105.3(3)
I1 ^x -I2-I3 ^{viii}	105.3(3)	105.3(3)	105.3(3)
I1-I2-I2 ⁱⁱⁱ	89.3(4)	80.4(4)	97.3(3)
I1-I2-I2 ^v	90.2(4)	86.9(4)	96.9(4)

I1-I2-I3 ⁱⁱⁱ	70.3(3)	70.3(3)	70.3(3)
I1-I2-I3 ^{viii}	70.3(3)	70.3(3)	70.3(3)
I2 ^v -I2-I2 ^v	174.9(5)	168.3(6)	178.7(6)
I2 ^v -I2-I3 ⁱⁱⁱ	148.1(2)	148.1(2)	148.1(2)
I2 ^v -I2-I3 ^{viii}	148.1(2)	148.1(2)	148.1(2)
I3 ⁱⁱⁱ -I2-I3 ^{viii}	46.69(14)	46.69(14)	46.69(14)
Te3-I3-I1 ⁱⁱⁱ	113.92(12)	113.92(12)	113.92(12)
Te3-I3-I2 ^v	112.40(13)	112.40(13)	112.40(13)
Te3-I3-I3 ^{ix}	176.75(11)	176.75(11)	176.75(11)
I1 ⁱⁱⁱ -I3-I2 ^v	133.28(11)	133.28(11)	133.28(11)
I1 ⁱⁱⁱ -I3-I3 ^{ix}	66.75(8)	66.75(8)	66.75(8)
I2 ^v -I3-I3 ^{ix}	66.65(10)	66.65(10)	66.65(10)
(i)	-x+1,-y+1,-z		
(ii)	-x+1,-y+1,-z+1		
(iii)	x,y,z-1		
(iv)	-x,-y+1,-z+1		
(v)	x,y,z+1		
(vi)	x+1,y,z		
(vii)	x,-y+3/2,z+1		
(viii)	x,-y+3/2,z-1		
(ix)	x,-y+3/2,z		
(x)	x-1,y,z		

Crystallographic details for WTe₂Br_{0.5}

Table S17: Fractional atomic coordinates and isotropic or equivalent isotropic displacement parameters (Å²) for WTe₂Br_{0.5}.

	x	y	z	U _{iso} [*] /U _{eq}
W1	-0.00516 (15)	0.25	-0.1785 (3)	0.0527 (15)
Te1	-0.07421 (12)	0.25	-0.5896 (5)	0.042 (2)
Te2	0.12012 (14)	0.25	0.0912 (5)	0.039 (2)
Br1	-0.2500	0.25	-0.6083 (13)	0.115 (7)

Table S18: for WTe₂Br_{0.5}.

	U ¹¹	U ²²	U ³³	U ¹²	U ¹³	U ²³
W1	0.0192 (14)	0.0821 (16)	0.0568 (14)	0	-0.0072 (17)	0
Te1	0.020 (3)	0.048 (3)	0.0574 (18)	0	0.013 (2)	0
Te2	0.047 (3)	0.044 (3)	0.0274 (17)	0	-0.010 (3)	0
Br1	0.145 (9)	0.036 (5)	0.163 (7)	0	0	0

Table S19: Atomic displacement parameters (Å²) for WTe₂Br_{0.5}.

W1—W1 ⁱ	3.6773 (1)	Te1—Te2 ^{vi}	3.735 (4)
W1—W1 ⁱⁱ	3.6773 (1)	Te1—Te2 ⁱⁱⁱ	3.718 (4)
W1—W1 ⁱⁱⁱ	2.909 (2)	Te1—Te2 ^{vii}	3.735 (4)
W1—W1 ^{iv}	2.909 (2)	Te1—Te2 ^{iv}	3.718 (4)
W1—Te1	2.835 (4)	Te1—Br1	2.946 (2)
W1—Te1 ^v	3.884 (4)	Te2—W1	2.699 (4)
W1—Te1 ^{vi}	2.698 (3)	Te2—W1 ⁱⁱⁱ	2.718 (3)
W1—Te1 ^{vii}	2.698 (3)	Te2—W1 ^{iv}	2.718 (3)
W1—Te2	2.699 (4)	Te2—Te1 ^v	3.825 (4)
W1—Te2 ⁱⁱⁱ	2.718 (3)	Te2—Te1 ^{vi}	3.735 (4)
W1—Te2 ^{iv}	2.718 (3)	Te2—Te1 ⁱⁱⁱ	3.718 (4)
Te1—W1 ^{viii}	3.884 (4)	Te2—Te1 ^{vii}	3.735 (4)
Te1—W1	2.835 (4)	Te2—Te1 ^{iv}	3.718 (4)
Te1—W1 ^{vi}	2.698 (3)	Te2—Te2 ⁱ	3.6773 (1)
Te1—W1 ^{vii}	2.698 (3)	Te2—Te2 ⁱⁱ	3.6773 (1)
Te1—Te1 ⁱ	3.6773 (1)	Br1—Te1	2.946 (2)
Te1—Te1 ⁱⁱ	3.6773 (1)	Br1—Te1 ^{ix}	2.946 (2)
Te1—Te1 ^{vi}	3.291 (3)	Br1—Br1 ⁱ	3.6773 (1)
Te1—Te1 ^{vii}	3.291 (3)	Br1—Br1 ⁱⁱ	3.6773 (1)
Te1—Te2 ^{viii}	3.825 (4)		

Symmetry codes: (i) x, y-1, z; (ii) x, y+1, z; (iii) -x, y-1/2, -z; (iv) -x, y+1/2, -z; (v) x, y, z+1; (vi) -x, y-1/2, -z-1; (vii) -x, y+1/2, -z-1; (viii) x, y, z-1; (ix) -x-1/2, -y+1/2, z. Table S20: for WTe₂Br_{0.5}.

W1 ⁱ —W1—W1 ⁱⁱ	180	W1 ^{vii} —Te1—Br1	118.07 (13)
W1 ⁱ —W1—W1 ⁱⁱⁱ	50.80 (6)	Te1 ⁱ —Te1—Te1 ⁱⁱ	180
W1 ⁱ —W1—W1 ^{iv}	129.20 (6)	Te1 ⁱ —Te1—Te1 ^{vi}	56.03 (7)
W1 ⁱ —W1—Te1	90.00 (10)	Te1 ⁱ —Te1—Te1 ^{vii}	123.97 (7)
W1 ⁱ —W1—Te1 ^v	90.00 (8)	Te1 ⁱ —Te1—	90.00 (8)
W1 ⁱ —W1—Te1 ^{vi}	47.04 (7)	Te1 ⁱⁱⁱ —Te1—Te2 ^{vi}	60.51 (9)
W1 ⁱ —W1—Te1 ^{vii}	132.96 (7)	Te1 ⁱ —Te1—Te2 ⁱⁱⁱ	60.36 (9)
W1 ⁱ —W1—Te2	90.00 (10)	Te1 ⁱ —Te1—Te2 ^{vii}	119.49 (9)
W1 ⁱ —W1—Te2 ⁱⁱⁱ	47.43 (7)	Te1 ⁱ —Te1—Te2 ^{iv}	119.64 (9)
W1 ⁱ —W1—Te2 ^{iv}	132.57 (7)	Te1 ⁱ —Te1—Br1	90.00 (5)
W1 ⁱⁱ —W1—W1 ⁱⁱⁱ	129.20 (6)	Te1 ⁱⁱ —Te1—Te1 ^{vi}	123.97 (7)

W1 ⁱⁱ —W1—W1 ^{iv}	50.80 (6)	Te1 ⁱⁱ —Te1—	56.03 (7)
W1 ⁱⁱ —W1—Te1	90.00 (10)	Te1 ⁱⁱⁱ —Te1—	90.00 (8)
W1 ⁱⁱ —W1—Te1 ^v	90.00 (8)	Te1 ⁱⁱⁱⁱ —Te1—Te2 ^{vi}	119.49 (9)
W1 ⁱⁱ —W1—Te1 ^{vi}	132.96 (7)	Te1 ⁱⁱ —Te1—Te2 ⁱⁱⁱ	119.64 (9)
W1 ⁱⁱ —W1—Te1 ^{vii}	47.04 (7)	Te1 ⁱⁱ —Te1—	60.51 (9)
W1 ⁱⁱ —W1—Te2	90.00 (10)	Te1 ⁱⁱ —Te1—Te2 ^{iv}	60.36 (9)
W1 ⁱⁱ —W1—Te2 ⁱⁱⁱ	132.57 (7)	Te1 ⁱⁱ —Te1—Br1	90.00 (5)
W1 ⁱⁱ —W1—Te2 ^{iv}	47.43 (7)	Te1 ^{vi} —Te1—	67.93 (7)
W1 ⁱⁱⁱ —W1—W1 ^{iv}	78.40 (6)	Te1 ^{vii} —Te1—	62.46 (10)
W1 ⁱⁱⁱ —W1—Te1	136.86 (16)	Te1 ^{viii} —Te1—	99.81 (13)
W1 ⁱⁱⁱ —W1—Te1 ^{vi}	87.61 (13)	Te1 ^{vi} —Te1—	65.82 (10)
W1 ⁱⁱⁱ —W1—Te1 ^{vii}	145.05 (13)	Te1 ^{vii} —Te1—	136.09 (13)
W1 ⁱⁱⁱ —W1—Te2	57.84 (10)	Te1 ^{viii} —Te1—	98.22 (10)
W1 ⁱⁱⁱ —W1—Te2 ⁱⁱⁱ	57.20 (10)	Te1 ^{vi} —Te1—Br1	140.20 (11)
W1 ⁱⁱⁱ —W1—Te2 ^{iv}	108.26 (10)	Te1 ^{vii} —Te1—	62.46 (10)
W1 ^{iv} —W1—Te1	136.86 (16)	Te1 ^{viii} —Te1—	136.09 (13)
W1 ^{iv} —W1—Te1 ^{vi}	145.05 (13)	Te1 ^{vii} —Te1—	98.22 (10)
W1 ^{iv} —W1—Te1 ^{vii}	87.61 (13)	Te1 ^{viii} —Te1—	99.81 (13)
W1 ^{iv} —W1—Te2	57.84 (10)	Te1 ^{vii} —Te1—	65.82 (10)
W1 ^{iv} —W1—Te2 ⁱⁱⁱ	108.26 (10)	Te1 ^{viii} —Te1—Br1	140.20 (11)
W1 ^{iv} —W1—Te2 ^{iv}	57.20 (10)	Te2 ^{viii} —Te1—	74.38 (10)
Te1—W1—Te1 ^v	138.61 (18)	Te2 ^{viii} —Te1—	128.28 (14)
Te1—W1—Te1 ^{vi}	72.95 (12)	Te2 ^{viii} —Te1—	74.38 (10)
Te1—W1—Te1 ^{vii}	72.95 (12)	Te2 ^{viii} —Te1—	128.28 (14)
Te1—W1—Te2	153.1 (2)	Te2 ^{viii} —Te1—Br1	146.01 (13)
Te1—W1—Te2 ⁱⁱⁱ	84.02 (14)	Te2 ^{vi} —Te1—	115.33 (15)
Te1—W1—Te2 ^{iv}	84.02 (14)	Te2 ^{vii} —Te1—	58.99 (9)
Te1 ^v —W1—Te1 ^{vi}	131.55 (16)	Te2 ^{vii} —Te1—	156.19 (15)
Te1 ^v —W1—Te1 ^{vii}	131.55 (16)	Te2 ^{vi} —Te1—Br1	76.14 (16)
Te1 ^v —W1—Te2	68.33 (12)	Te2 ⁱⁱⁱ —Te1—	156.19 (15)
Te1 ^v —W1—Te2 ⁱⁱⁱ	66.18 (11)	Te2 ⁱⁱⁱ —Te1—	59.28 (9)
Te1 ^v —W1—Te2 ^{iv}	66.18 (11)	Te2 ⁱⁱⁱ —Te1—Br1	80.04 (17)
Te1 ^{vi} —W1—	85.92 (8)	Te2 ^{vii} —Te1—	115.33 (15)
Te1 ^{vii} —W1—Te2	87.57 (15)	Te2 ^{vii} —Te1—Br1	76.14 (16)
Te1 ^{vi} —W1—Te2 ⁱⁱⁱ	89.85 (13)	Te2 ^{iv} —Te1—Br1	80.04 (17)
Te1 ^{vi} —W1—Te2 ^{iv}	156.82 (13)	W1—Te2—W1 ⁱⁱⁱ	64.96 (11)
Te1 ^{vii} —W1—Te2	87.57 (15)	W1—Te2—W1 ^{iv}	64.96 (11)
Te1 ^{vii} —W1—Te2 ⁱⁱⁱ	156.82 (13)	W1—Te2—Te1 ^v	70.69 (12)
Te1 ^{vii} —W1—	89.85 (13)	W1—Te2—Te1 ^{vi}	46.20 (11)
Te2—W1—Te2 ⁱⁱⁱ	115.04 (15)	W1—Te2—Te1 ⁱⁱⁱ	111.74 (15)
Te2—W1—Te2 ^{iv}	115.04 (15)	W1—Te2—Te1 ^{vii}	46.20 (11)
Te2 ⁱⁱⁱ —W1—Te2 ^{iv}	85.13 (8)	W1—Te2—Te1 ^{iv}	111.74 (15)
W1 ^{viii} —Te1—W1	138.61 (13)	W1—Te2—Te2 ⁱ	90.00 (10)
W1 ^{viii} —Te1—W1 ^{vi}	48.45 (9)	W1—Te2—Te2 ⁱⁱ	90.00 (10)
W1 ^{viii} —Te1—	48.45 (9)	W1 ⁱⁱⁱ —Te2—W1 ^{iv}	85.13 (8)
W1 ^{viii} —Te1—Te1 ⁱ	90.00 (8)	W1 ⁱⁱⁱ —Te2—Te1 ^{vi}	72.07 (12)
W1 ^{viii} —Te1—Te1 ⁱⁱ	90.00 (8)	W1 ⁱⁱⁱ —Te2—Te1 ⁱⁱⁱ	49.33 (10)
W1 ^{viii} —Te1—	95.88 (11)	W1 ⁱⁱⁱ —Te2—Te1 ^{vii}	110.99 (12)
W1 ^{viii} —Te1—	95.88 (11)	W1 ⁱⁱⁱ —Te2—Te1 ^{iv}	91.00 (10)
W1 ^{viii} —Te1—	150.16 (13)	W1 ⁱⁱⁱ —Te2—Te2 ⁱ	47.43 (7)
W1 ^{viii} —Te1—	150.16 (13)	W1 ⁱⁱⁱ —Te2—Te2 ⁱⁱ	132.57 (7)
W1 ^{viii} —Te1—Br1	105.03 (18)	W1 ^{iv} —Te2—Te1 ^{vi}	110.99 (12)
W1—Te1—W1 ^{vi}	107.05 (13)	W1 ^{iv} —Te2—Te1 ⁱⁱⁱ	91.00 (10)
W1—Te1—W1 ^{vii}	107.05 (13)	W1 ^{iv} —Te2—	72.07 (12)
W1—Te1—Te1 ⁱ	90.00 (10)	W1 ^{iv} —Te2—Te1 ^{iv}	49.33 (10)
W1—Te1—Te1 ⁱⁱ	90.00 (10)	W1 ^{iv} —Te2—Te2 ⁱ	132.57 (7)
W1—Te1—Te1 ^{vi}	51.61 (10)	W1 ^{iv} —Te2—Te2 ⁱⁱ	47.43 (7)
W1—Te1—Te1 ^{vii}	51.61 (10)	Te1 ^v —Te2—Te1 ^{vi}	105.62 (13)
W1—Te1—Te2 ^{viii}	97.63 (14)	Te1 ^v —Te2—Te1 ⁱⁱⁱ	51.72 (9)
W1—Te1—Te2 ^{vi}	148.89 (16)	Te1 ^v —Te2—	105.62 (13)
W1—Te1—Te2 ⁱⁱⁱ	46.65 (10)	Te1 ^v —Te2—Te1 ^{iv}	51.72 (9)
W1—Te1—Te2 ^{vii}	148.89 (16)	Te1 ^v —Te2—Te2 ⁱ	90.00 (8)
W1—Te1—Te2 ^{iv}	46.65 (10)	Te1 ^v —Te2—Te2 ⁱⁱ	90.00 (8)

W1—Te1—Br1	116.36 (19)	Te1 ^{vi} —Te2—	115.33 (15)
W1 ^{vi} —Te1—W1 ^{vii}	85.92 (8)	Te1 ^{vi} —Te2—	58.99 (9)
W1 ^{vi} —Te1—Te1 ⁱ	47.04 (7)	Te1 ^{vi} —Te2—	156.19 (15)
W1 ^{vi} —Te1—Te1 ⁱⁱ	132.96 (7)	Te1 ^{vi} —Te2—Te2 ⁱ	60.51 (9)
W1 ^{vi} —Te1—Te1 ^{vi}	55.45 (10)	Te1 ^{vi} —Te2—Te2 ⁱⁱ	119.49 (9)
W1 ^{vi} —Te1—	101.20 (10)	Te1 ⁱⁱⁱ —Te2—	156.19 (15)
W1 ^{vi} —Te1—	45.29 (9)	Te1 ⁱⁱⁱ —Te2—	59.28 (9)
W1 ^{vi} —Te1—Te2 ^{vi}	46.22 (10)	Te1 ⁱⁱⁱ —Te2—Te2 ⁱ	60.36 (9)
W1 ^{vi} —Te1—Te2 ⁱⁱⁱ	102.81 (14)	Te1 ⁱⁱⁱ —Te2—Te2 ⁱⁱ	119.64 (9)
W1 ^{vi} —Te1—	88.81 (10)	Te1 ^{vii} —Te2—	115.33 (15)
W1 ^{vi} —Te1—Te2 ^{iv}	153.61 (14)	Te1 ^{vii} —Te2—Te2 ⁱ	119.49 (9)
W1 ^{vi} —Te1—Br1	118.07 (13)	Te1 ^{vii} —Te2—	60.51 (9)
W1 ^{vii} —Te1—Te1 ⁱ	132.96 (7)	Te1 ^{iv} —Te2—Te2 ⁱ	119.64 (9)
W1 ^{vii} —Te1—Te1 ⁱⁱ	47.04 (7)	Te1 ^{iv} —Te2—Te2 ⁱⁱ	60.36 (9)
W1 ^{vii} —Te1—	101.20 (10)	Te2 ⁱ —Te2—Te2 ⁱⁱ	180
W1 ^{vii} —Te1—	55.45 (10)	Te1—Br1—Te1 ^{ix}	175.42 (13)
W1 ^{vii} —Te1—	45.29 (9)	Te1—Br1—Br1 ⁱ	90.00 (5)
W1 ^{vii} —Te1—	88.81 (10)	Te1—Br1—Br1 ⁱⁱ	90.00 (5)
W1 ^{vii} —Te1—Te2 ⁱⁱⁱ	153.61 (14)	Te1 ^{ix} —Br1—Br1 ⁱ	90.00 (5)
W1 ^{vii} —Te1—	46.22 (10)	Te1 ^{ix} —Br1—Br1 ⁱⁱ	90.00 (5)
W1 ^{vii} —Te1—	102.81 (14)	Br1 ⁱ —Br1—Br1 ⁱⁱ	180

Symmetry codes: (i) $x, y-1, z$; (ii) $x, y+1, z$; (iii) $-x, y-1/2, -z$; (iv) $-x, y+1/2, -z$; (v) $x, y, z+1$; (vi) $-x, y-1/2, -z-1$; (vii) $-x, y+1/2, -z-1$; (viii) $x, y, z-1$; (ix) $-x-1/2, -y+1/2, z$.

Crystallographic details for $\text{WTe}_2\text{Br}_{1.25}$

Table S 21: Fractional Atomic Coordinates ($\times 10^4$) and Equivalent Isotropic Displacement Parameters ($\text{\AA}^2 \times 10^3$) for $\text{WTe}_2\text{Br}_{1.25}$. U_{eq} is defined as 1/3 of the trace of the orthogonalised U_j .

Atom	x	y	z	U_{eq}
W4	5000	3794(2)	723(8)	55(2)
W8	5000	3803(2)	5768(8)	57(2)
W6	1607(5)	3809.8(15)	5719(5)	56(2)
W3	3417(5)	3849.9(16)	2475(5)	58(2)
W2	1886(4)	3782.2(15)	703(5)	57(2)
W5	0	3832(2)	7490(7)	55(2)
W7	3155(5)	3850.8(15)	7480(5)	58(2)
W1	0	3858(2)	2403(8)	64(3)
Te1	0	3357(3)	1159(9)	53(3)
Te3	3411(6)	3323(2)	1265(6)	52(2)
Te13	0	4055(3)	9515(10)	55(3)
Te12	5000	3538(3)	3811(9)	57(3)
Te15	3329(6)	4157(2)	-525(7)	55(2)
Te14	1712(6)	3461(2)	8708(7)	61(3)
Te10	1651(6)	3557(2)	3727(7)	60(3)
Te8	5000	4294(3)	7073(10)	55(3)
Te6	1594(7)	4313.7(17)	7032(7)	52(2)
Te16	5000	3555(3)	8679(10)	60(3)
Te9	0	4186(3)	4440(11)	57(3)
Te11	3342(6)	4177.7(19)	4490(7)	55(2)
Te5	0	3347(3)	6167(10)	59(3)
Te7	3283(7)	3357(2)	6187(7)	58(2)
Te4	5000	4313(3)	1945(12)	63(3)
Te2	1726(7)	4291(3)	1916(8)	71(3)
Br5	5000	2961(5)	3756(16)	63(5)
Br6	5000	2969(5)	8534(18)	64(5)
Br3	1794(15)	2597(4)	6973(16)	78(4)
Br4	1674(12)	2984(4)	3571(14)	71(4)
Br7	0	4636(6)	9607(19)	71(6)
Br8	3170(20)	5000	10520(20)	74(6)
Br1	5000	2249(6)	3950(20)	74(6)
Br9	3160(20)	5000	8530(20)	75(6)
Br10	0	5000	5910(60)	190(40)
Br2	3175(12)	2438(5)	5615(18)	86(5)
Br12	2920(40)	5000	6020(80)	290(50)
Br13	3020(60)	5000	2760(100)	350(80)
Br11	0	5000	3080(70)	240(60)

Table S22: Anisotropic Displacement Parameters ($\times 10^4$) for $\text{WTe}_2\text{Br}_{1.25}$. The anisotropic displacement factor exponent takes the form: $-2\pi^2[h^2a^{*2} \times U_{11} + \dots + 2hka^* \times b^* \times U_{12}]$

Atom	U_{11}	U_{22}	U_{33}	U_{23}	U_{13}	U_{12}
W4	31(3)	80(5)	55(5)	7(4)	0	0
W8	37(4)	79(5)	53(5)	-3(4)	0	0
W6	34(3)	77(4)	55(4)	-5(3)	1(3)	-1(2)
W3	32(3)	91(4)	51(3)	0(3)	-1(3)	0(2)
W2	31(3)	81(4)	60(4)	5(3)	-1(3)	0(2)
W5	35(4)	76(5)	55(5)	0(4)	0	0
W7	42(3)	80(4)	52(4)	1(3)	-2(3)	0(2)
W1	69(6)	70(5)	55(6)	1(4)	0	0
Te1	26(4)	76(7)	55(7)	-5(5)	0	0
Te3	31(3)	81(5)	45(4)	-2(3)	1(3)	-1(3)
Te13	23(4)	95(8)	49(6)	4(6)	0	0
Te12	24(4)	109(9)	37(6)	-5(6)	0	0
Te15	33(3)	85(5)	46(4)	0(4)	1(3)	2(3)
Te14	28(3)	104(6)	49(5)	-4(5)	2(3)	-1(3)
Te10	25(3)	100(6)	55(5)	-7(4)	1(3)	-2(3)
Te8	35(5)	73(7)	57(7)	-3(5)	0	0
Te6	43(4)	55(4)	59(5)	-5(3)	-2(4)	-1(3)
Te16	33(5)	93(8)	56(7)	-1(6)	0	0
Te9	36(5)	77(7)	58(7)	0(6)	0	0
Te11	32(3)	76(5)	57(4)	-2(4)	0(3)	0(3)
Te5	29(5)	95(9)	52(7)	-1(6)	0	0
Te7	31(3)	84(5)	58(5)	4(4)	1(3)	0(3)
Te4	24(4)	91(8)	74(8)	5(7)	0	0
Te2	20(3)	126(8)	66(6)	-2(5)	-4(3)	3(4)
Br5	20(6)	118(15)	51(11)	3(10)	0	0
Br6	60(10)	65(11)	67(13)	-8(9)	0	0
Br3	57(8)	84(9)	92(11)	-2(8)	21(8)	4(7)
Br4	41(6)	87(9)	86(11)	8(8)	1(7)	1(6)
Br7	29(7)	124(18)	58(12)	-3(11)	0	0
Br8	64(11)	65(11)	94(16)	0	10(12)	0
Br1	41(9)	102(15)	78(14)	0(12)	0	0
Br9	54(10)	92(14)	79(15)	0	13(10)	0
Br10	370(130)	60(20)	150(60)	0	0	0
Br2	36(6)	118(13)	104(13)	27(11)	9(8)	2(6)
Br12	60(20)	450(130)	370(110)	0	110(40)	0
Br13	190(50)	64(18)	800(200)	0	-300(90)	0
Br11	500(200)	50(20)	170(70)	0	0	0

Table S23: Bond Lengths in Å for **WTe₂Br_{1.25}**.

Atom	Atom	Length/Å	Atom	Atom	Length/Å
W4	W3	2.789(9)	W2	Te3	2.653(10)
W4	W3 ¹	2.789(9)	W2	Te13 ²	2.763(11)
W4	Te3	2.725(11)	W2	Te15	2.713(10)
W4	Te3 ¹	2.725(11)	W2	Te14 ²	2.879(12)
W4	Te15	2.843(11)	W2	Te2	2.676(13)
W4	Te15 ¹	2.843(11)	W5	Te13	2.731(16)
W4	Te16 ²	2.778(16)	W5	Te14 ³	2.866(11)
W4	Te4	2.716(17)	W5	Te14	2.866(11)
W8	W7 ¹	2.925(9)	W5	Te6	2.738(10)
W8	W7	2.925(9)	W5	Te6 ³	2.738(10)
W8	Te12	2.723(15)	W5	Te5	2.672(16)
W8	Te8	2.680(15)	W7	Te15 ⁴	2.849(11)
W8	Te11	2.883(11)	W7	Te14	2.750(11)
W8	Te11 ¹	2.883(11)	W7	Te8	2.782(11)
W8	Te7	2.701(11)	W7	Te6	2.653(10)
W8	Te7 ¹	2.701(11)	W7	Te16	2.783(11)
W6	W5	2.815(9)	W7	Te7	2.685(12)
W6	W7	2.772(9)	W1	Te1	2.668(15)
W6	Te10	2.741(11)	W1	Te10	2.748(12)
W6	Te6	2.730(10)	W1	Te10 ³	2.748(12)
W6	Te9	2.852(12)	W1	Te9	2.933(17)
W6	Te11	2.883(11)	W1	Te2 ³	2.685(12)
W6	Te5	2.682(13)	W1	Te2	2.685(12)
W6	Te7	2.706(10)	Te13	Br7	2.50(3)
W3	W2	2.781(8)	Te12	Br5	2.48(3)
W3	Te3	2.736(11)	Te10	Br4	2.473(19)
W3	Te12	2.735(12)	Te16	Br6	2.53(2)
W3	Te10	2.758(10)	Br3	Br2	2.36(2)
W3	Te11	2.910(11)	Br8	Br9	2.51(3)
W3	Te4	2.692(13)			
W3	Te2	2.706(12)			
W2	W1	2.955(9)			
W2	Te1	2.775(11)			

¹1-x,+y,+z; ²+x,+y,-1+z; ³-x,+y,+z; ⁴+x,+y,1+z

Table S24: Bond Angles in ° for **WTe₂Br_{1.25}**.

Atom	Atom	Atom	Angle/°	Atom	Atom	Atom	Angle/°
W3 ¹	W4	W3	74.2(3)	Te16 ²	W4	Te15	71.8(4)
W3 ¹	W4	Te15	140.2(4)	Te16 ²	W4	Te15 ¹	71.8(4)
W3	W4	Te15 ¹	140.2(4)	Te4	W4	W3	58.5(3)
W3 ¹	W4	Te15 ¹	90.9(2)	Te4	W4	W3 ¹	58.5(3)
W3	W4	Te15	90.9(2)	Te4	W4	Te3 ¹	118.0(4)
Te3 ¹	W4	W3 ¹	59.5(2)	Te4	W4	Te3	118.0(4)
Te3	W4	W3	59.5(2)	Te4	W4	Te15	82.1(4)
Te3	W4	W3 ¹	103.8(4)	Te4	W4	Te15 ¹	82.1(4)
Te3 ¹	W4	W3	103.8(4)	Te4	W4	Te16 ²	146.3(6)
Te3 ¹	W4	Te3	76.6(4)	W7	W8	W7 ¹	84.1(3)
Te3 ¹	W4	Te15	159.3(5)	Te12	W8	W7 ¹	134.5(2)
Te3	W4	Te15	99.3(2)	Te12	W8	W7	134.5(2)
Te3	W4	Te15 ¹	159.3(5)	Te12	W8	Te11	74.1(4)
Te3 ¹	W4	Te15 ¹	99.3(2)	Te12	W8	Te11 ¹	74.1(4)
Te3	W4	Te16 ²	87.6(4)	Te8	W8	W7 ¹	59.3(3)
Te3 ¹	W4	Te16 ²	87.6(4)	Te8	W8	W7	59.3(3)
Te15 ¹	W4	Te15	77.3(4)	Te8	W8	Te12	152.7(6)
Te16 ²	W4	W3 ¹	140.3(2)	Te8	W8	Te11 ¹	84.4(4)
Te16 ²	W4	W3	140.3(2)	Te8	W8	Te11	84.4(4)

Atom	Atom	Atom	Angle ^o
Te8	W8	Te7	116.1(4)
Te8	W8	Te7 ¹	116.1(4)
Te11 ¹	W8	W7 ¹	88.0(2)
Te11	W8	W7	88.0(2)
Te11 ¹	W8	W7	141.6(4)
Te11	W8	W7 ¹	141.6(4)
Te11	W8	Te11 ¹	75.3(4)
Te7	W8	W7 ¹	111.0(4)
Te7	W8	W7	56.8(3)
Te7 ¹	W8	W7	111.0(4)
Te7 ¹	W8	W7 ¹	56.8(3)
Te7 ¹	W8	Te12	83.1(4)
Te7	W8	Te12	83.1(4)
Te7	W8	Te11	95.4(3)
Te7	W8	Te11 ¹	156.9(4)
Te7 ¹	W8	Te11 ¹	95.5(3)
Te7 ¹	W8	Te11	156.9(4)
Te7	W8	Te7 ¹	84.9(5)
W5	W6	Te9	93.9(3)
W5	W6	Te11	142.8(3)
W7	W6	W5	73.7(2)
W7	W6	Te9	140.7(4)
W7	W6	Te11	91.0(3)
Te10	W6	W5	138.9(3)
Te10	W6	W7	138.7(3)
Te10	W6	Te9	73.5(4)
Te10	W6	Te11	73.3(3)
Te6	W6	W5	59.2(3)
Te6	W6	W7	57.7(2)
Te6	W6	Te10	150.8(4)
Te6	W6	Te9	83.7(3)
Te6	W6	Te11	83.9(3)
Te9	W6	Te11	76.5(3)
Te5	W6	W5	58.1(3)
Te5	W6	W7	104.8(3)
Te5	W6	Te10	84.8(4)
Te5	W6	Te6	117.3(4)
Te5	W6	Te9	99.2(3)
Te5	W6	Te11	158.1(4)
Te5	W6	Te7	80.7(3)
Te7	W6	W5	104.5(3)
Te7	W6	W7	58.7(3)
Te7	W6	Te10	84.4(3)
Te7	W6	Te6	116.3(3)
Te7	W6	Te9	157.8(4)
Te7	W6	Te11	95.3(3)
W4	W3	Te11	138.8(3)
W2	W3	W4	72.8(2)
W2	W3	Te11	137.6(3)
Te3	W3	W4	59.1(3)
Te3	W3	W2	57.5(2)
Te3	W3	Te10	86.5(3)
Te3	W3	Te11	152.9(4)
Te12	W3	W4	94.4(3)
Te12	W3	W2	143.5(4)
Te12	W3	Te3	86.5(4)
Te12	W3	Te10	80.8(3)
Te12	W3	Te11	73.5(3)
Te10	W3	W4	145.6(4)
Te10	W3	W2	90.9(3)
Te10	W3	Te11	72.6(3)
Te4	W3	W4	59.4(4)

Atom	Atom	Atom	Angle ^o
Te4	W3	W2	104.0(4)
Te4	W3	Te3	118.5(4)
Te4	W3	Te12	97.6(4)
Te4	W3	Te10	154.9(5)
Te4	W3	Te11	82.9(4)
Te4	W3	Te2	80.3(3)
Te2	W3	W4	104.7(3)
Te2	W3	W2	58.4(3)
Te2	W3	Te3	115.7(4)
Te2	W3	Te12	156.0(4)
Te2	W3	Te10	91.1(3)
Te2	W3	Te11	82.5(3)
W3	W2	W1	78.5(2)
W3	W2	Te14 ²	142.4(3)
Te1	W2	W3	108.9(3)
Te1	W2	W1	55.4(3)
Te1	W2	Te14 ²	79.6(3)
Te3	W2	W3	60.4(3)
Te3	W2	W1	107.5(3)
Te3	W2	Te1	83.9(3)
Te3	W2	Te13 ²	154.7(4)
Te3	W2	Te15	104.6(3)
Te3	W2	Te14 ²	85.2(3)
Te3	W2	Te2	119.7(4)
Te13 ²	W2	W3	144.7(4)
Te13 ²	W2	W1	81.7(3)
Te13 ²	W2	Te1	82.5(3)
Te13 ²	W2	Te14 ²	71.5(4)
Te15	W2	W3	93.9(3)
Te15	W2	W1	137.1(4)
Te15	W2	Te1	156.8(4)
Te15	W2	Te13 ²	81.2(3)
Te15	W2	Te14 ²	79.7(3)
Te14 ²	W2	W1	130.2(3)
Te2	W2	W3	59.4(3)
Te2	W2	W1	56.7(3)
Te2	W2	Te1	112.0(4)
Te2	W2	Te13 ²	85.3(4)
Te2	W2	Te15	82.9(3)
Te2	W2	Te14 ²	152.7(4)
W6 ³	W5	W6	74.6(3)
W6	W5	Te14 ³	142.4(4)
W6 ³	W5	Te14 ³	91.3(2)
W6	W5	Te14	91.3(2)
W6 ³	W5	Te14	142.4(4)
Te13	W5	W6 ³	139.1(2)
Te13	W5	W6	139.1(2)
Te13	W5	Te14	72.1(4)
Te13	W5	Te14 ³	72.1(4)
Te13	W5	Te6	86.1(4)
Te13	W5	Te6 ³	86.1(4)
Te14 ³	W5	Te14	78.8(4)
Te6 ³	W5	W6	103.4(4)
Te6	W5	W6	58.9(3)
Te6 ³	W5	W6 ³	58.9(3)
Te6	W5	W6 ³	103.4(4)
Te6 ³	W5	Te14 ³	98.2(3)
Te6	W5	Te14 ³	158.0(5)
Te6 ³	W5	Te14	158.0(5)
Te6	W5	Te14	98.2(3)
Te6	W5	Te6 ³	76.4(4)
Te5	W5	W6	58.4(3)

Atom	Atom	Atom	Angle ^f
Te5	W5	W6 ³	58.4(3)
Te5	W5	Te13	149.2(6)
Te5	W5	Te14 ³	84.3(4)
Te5	W5	Te14	84.3(4)
Te5	W5	Te6 ³	117.3(4)
Te5	W5	Te6	117.3(4)
W6	W7	W8	78.5(2)
W6	W7	Te15 ⁴	141.0(3)
W6	W7	Te8	108.2(3)
W6	W7	Te16	145.6(4)
Te15 ⁴	W7	W8	130.0(3)
Te14	W7	W8	138.3(4)
Te14	W7	W6	94.7(3)
Te14	W7	Te15 ⁴	79.6(3)
Te14	W7	Te8	156.2(4)
Te14	W7	Te16	78.9(3)
Te8	W7	W8	55.9(3)
Te8	W7	Te15 ⁴	78.5(3)
Te8	W7	Te16	85.3(3)
Te6	W7	W8	108.3(3)
Te6	W7	W6	60.4(2)
Te6	W7	Te15 ⁴	83.2(3)
Te6	W7	Te14	103.3(3)
Te6	W7	Te8	83.5(3)
Te6	W7	Te16	154.0(4)
Te6	W7	Te7	119.8(3)
Te16	W7	W8	84.2(3)
Te16	W7	Te15 ⁴	71.6(3)
Te7	W7	W8	57.4(3)
Te7	W7	W6	59.4(2)
Te7	W7	Te15 ⁴	154.3(4)
Te7	W7	Te14	83.6(3)
Te7	W7	Te8	113.3(4)
Te7	W7	Te16	86.2(4)
W2 ³	W1	W2	85.4(3)
Te1	W1	W2 ³	58.9(3)
Te1	W1	W2	58.9(3)
Te1	W1	Te10	88.7(4)
Te1	W1	Te10 ³	88.7(4)
Te1	W1	Te9	154.8(6)
Te1	W1	Te2 ³	115.2(4)
Te1	W1	Te2	115.2(4)
Te10	W1	W2 ³	145.4(4)
Te10	W1	W2	87.6(2)
Te10 ³	W1	W2	145.4(4)
Te10 ³	W1	W2 ³	87.6(2)
Te10 ³	W1	Te10	79.3(4)
Te10 ³	W1	Te9	72.1(3)
Te10	W1	Te9	72.1(3)
Te9	W1	W2	133.6(2)
Te9	W1	W2 ³	133.6(2)
Te2 ³	W1	W2 ³	56.4(3)
Te2	W1	W2 ³	111.9(4)
Te2	W1	W2	56.4(3)
Te2 ³	W1	W2	111.9(4)
Te2 ³	W1	Te10 ³	91.8(3)
Te2	W1	Te10 ³	154.5(5)
Te2	W1	Te10	91.8(3)
Te2 ³	W1	Te10	154.5(5)
Te2	W1	Te9	82.4(4)
Te2 ³	W1	Te9	82.4(4)
Te2	W1	Te2 ³	86.1(5)

Atom	Atom	Atom	Angle ^f
W2	Te1	W2 ³	92.4(4)
W1	Te1	W2	65.7(3)
W1	Te1	W2 ³	65.7(3)
W4	Te3	W3	61.4(3)
W2	Te3	W4	75.9(3)
W2	Te3	W3	62.1(3)
W2 ⁴	Te13	W2 ⁵	92.9(4)
W5	Te13	W2 ⁵	111.1(4)
W5	Te13	W2 ⁴	111.1(4)
Br7	Te13	W2 ⁵	113.5(5)
Br7	Te13	W2 ⁴	113.5(5)
Br7	Te13	W5	113.2(7)
W8	Te12	W3	110.7(5)
W8	Te12	W3 ¹	110.7(5)
W3	Te12	W3 ¹	75.9(4)
Br5	Te12	W8	116.4(7)
Br5	Te12	W3 ¹	118.3(5)
Br5	Te12	W3	118.3(5)
W4	Te15	W7 ²	106.0(4)
W2	Te15	W4	73.0(3)
W2	Te15	W7 ²	101.1(3)
W5	Te14	W2 ⁴	104.1(4)
W7	Te14	W2 ⁴	99.5(3)
W7	Te14	W5	73.3(3)
W6	Te10	W3	110.9(3)
W6	Te10	W1	111.1(4)
W1	Te10	W3	82.5(3)
Br4	Te10	W6	118.0(6)
Br4	Te10	W3	113.8(5)
Br4	Te10	W1	115.3(5)
W8	Te8	W7 ¹	64.7(3)
W8	Te8	W7	64.7(3)
W7 ¹	Te8	W7	89.5(4)
W6	Te6	W5	62.0(3)
W7	Te6	W6	62.0(2)
W7	Te6	W5	76.9(3)
W4 ⁴	Te16	W7 ¹	109.7(4)
W4 ⁴	Te16	W7	109.7(4)
W7	Te16	W7 ¹	89.5(5)
Br6	Te16	W4 ⁴	115.8(7)
Br6	Te16	W7	114.6(5)
Br6	Te16	W7 ¹	114.6(5)
W6	Te9	W6 ³	73.5(4)
W6	Te9	W1	102.9(4)
W6 ³	Te9	W1	102.9(4)
W8	Te11	W3	101.6(3)
W6	Te11	W8	77.4(3)
W6	Te11	W3	102.8(3)
W6 ³	Te5	W6	79.0(5)
W5	Te5	W6 ³	63.4(4)
W5	Te5	W6	63.4(4)
W8	Te7	W6	83.6(3)
W7	Te7	W8	65.8(3)
W7	Te7	W6	61.9(3)
W3	Te4	W4	62.1(3)
W3 ¹	Te4	W4	62.1(3)
W3 ¹	Te4	W3	77.3(5)
W2	Te2	W3	62.2(3)
W2	Te2	W1	66.9(3)
W1	Te2	W3	84.7(4)

¹1-x,+y,+z; ²+x,+y,-1+z; ³-x,+y,+z; ⁴+x,+y,1+z; ⁵-x,+y,1+z

